University of California
Los Angeles

Search for Dark Matter with XENON100 and Future Ton-Scale Detectors

A dissertation submitted in partial satisfaction
of the requirements for the degree
Doctor of Philosophy in Physics

by

Chi Wai Lam

2010

The dissertation of Chi Wai Lam is approved.

Alan L. Yuille

David Saltzberg

Graciela B. Gelmini

Katsushi Arisaka, Committee Chair

University of California, Los Angeles

2010

To my parents

Table of Contents

List of Figures

List of Tables

ACKNOWLEDGMENTS

I would first like to thank my doctoral committee members, Professor Alan Yuille, Professor David Saltzberg, Professor Graciela Gelmini, and Professor Katsushi Arisaka. My deepest gratefulness goes to my advisor, Professor Katsushi Arisaka, who have taught me many important things, both in and outside of Physics, and not only in words but also by his action as an example. With his energy, he has pushed me to work hard and move fast, and showed me how to be efficient and go in the right direction when pursuing one's goal. Last but not least, he helped me numerous times in tremendous ways which I will never forget.

My thanks also go to Professor Peter Smith, who is a true expert in the field of dark matter. With his enthusiasm to share his knowledge with others, I have benefited a lot from him, both from discussions and asking questions during and after group meetings. I would like to thank Dr. Hanguo Wang, who has generously offered me important advice. I would also like to thank all the people in the XENON collaboration and my colleagues in the UCLA dark matter group, Ethan Brown, Kevin Lung, Dr. Emilia Pantic, and Artin Teymourian, all of whom I have enjoyed working with for the past years.

I would like to express my gratitude to all my family members, especially my parents, whom this dissertation is dedicated to. Without their support over the years, it would not have been possible for me to achieve my goal.

Vita

1981	Born, Macau SAR, China
2002	B.S. (Physics, Summa Cum Laude), UCLA, Los Angeles, California, USA.
2003–2004	Teaching Assistant, Physics and Astronomy Department, UCLA.
2005–2008	Teaching Associate, Physics and Astronomy Department, UCLA.
2008–present	Research Assistant, Physics and Astronomy Department, UCLA.

Publications

K. Arisaka *et al.*, *XAX: a multi-ton, multi-target detection system for dark matter, double beta decay and pp solar neutrinos.* Astropart. Phys. **31**, 63 (2009).

E. Aprile *et al.* (XENON100 Collaboration) (2010), *First Dark Matter Results from the XENON100 Experiment.* arXiv:1005.0380v2 (Accepted by Phys. Rev. Lett.).

ABSTRACT OF THE DISSERTATION

Search for Dark Matter with XENON100 and Future Ton-Scale Detectors

by

Chi Wai Lam

Doctor of Philosophy in Physics

University of California, Los Angeles, 2010

Professor Katsushi Arisaka, Chair

This dissertation describes XENON100, a dark matter experiment located at the Laboratori Nazionali del Gran Sasso in Italy, which employs two-phase time projection chamber techniques and utilizes liquid xenon as a target to search for weakly interacting massive particles (WIMP). An analysis of the 40 kg × 11.17 days non-blind data acquired in Oct.-Nov. 2009 will be presented here. In particular, the scenarios of spin-independent (SI) low mass WIMPs and inelastic dark matter (iDM) will be studied. In this analysis, it is found that both low mass WIMPs and inelastic dark matter remain possible as an explanation for the disagreement between the DAMA experiment and other null-result experiments. Finally, a background study of ton-scale liquid xenon and liquid argon detectors for the next generation will be described. It is shown that the future detectors, which can achieve low background level and improved sensitivity, will be capable of probing the SUSY parameter space and allow for measurements of WIMP properties.

CHAPTER 1

Introduction

Over the last few decades, there has been tremendous progress in both theoretical and experimental physics in terms of answering the fundamental questions of our universe. In particle physics, the greatest success, known as the standard model, has managed to explain the interaction of particles to the smallest scale of length achievable to date. One of the beauties of the standard model lies in its ability to divide observable matter into categories of only a few particles, which consists of 6 leptons, 6 quarks, and the mediating bosons of the fundamental forces. The results of a vast array of experiments in particle physics, whether it comes to the measurements of the masses of the W and Z bosons, or the magnetic dipole moment of a tiny electron, all agree with the standard model well within experimental uncertainty. In astrophysics, on the other hand, scientists have come to understanding many important aspects of the universe, such as stellar dynamics and evolution, as well as the cosmic microwave background.

However, there remain unresolved problems regarding the most basic questions of the universe. It is still unknown how large scale structures were formed in the early universe, which is homogeneous as predicted from the cosmic microwave background radiation. In terms of particle content, the composition of the universe has puzzled physicists and astronomers. It is estimated that only about 4.6% of the mass of the universe is made up of baryonic or 'ordinary' matter. About 23% of the mass is composed of so called 'dark matter', which does not, or rarely, interacts with baryonic matter, and thus cannot be easily observed experimentally (Fig. 1.1). The remaining 72% of the mass is composed of dark energy, whose content is even more unknown to us, but is crucial in explaining the accelerating expansion rate of the universe. Finding out the content of dark matter has become an obstacle in the quest of fully understanding the questions about the universe. Theorists have been proposing numerous particle models to provide candidates for the dark matter. Experimentalists, on the other hand, have been carrying out different experiments in detecting dark matter from various approaches. Experiments are done not only in hope of merely verifying the existence of dark matter, but also towards the goal of measuring its properties characterized by observable parameters, which may shed light on possible particle models.

The first part of this dissertation describes the firsts results of XENON100, which is an experiment that is designed for direct detection of Weakly Interacting Massive Particles (WIMP), a dark matter candidate, and which has established one of the world's best experimental limits to date. The second part of this dissertation describes future generation detectors which aim to achieve order of magnitude improvements in the limit over current experiments. In particular, the Monte Carlo studies of radioactive backgrounds in the future detectors will be described.

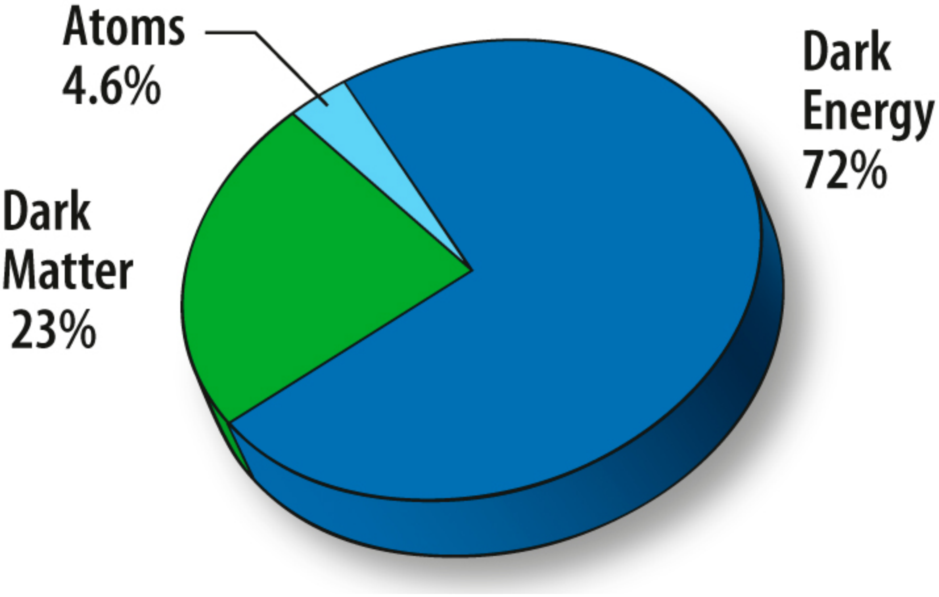

Figure 1.1: Composition of the Universe. Figure taken from [1]

CHAPTER 2

Detection of Dark Matter

2.1 Detection Methods

There are numerous experiments that aim to verify the existence of dark matter. They can be divided into 3 different categories: (1) direct detection, (2) indirect detection, and (3) accelerator search. Direct detection looks for dark matter by detecting the energy deposits of a dark matter scattering off of a target material. These experiments look for cold dark matter candidates such as weakly interacting massive particles (WIMPs) and axions in the dark matter halo of our galaxy. WIMPs in the dark matter halo of the Milky Way are estimated to exist with a density of ~ 0.3 GeV/c^2 and average kinetic energy of a few tens of keV. Major direct detection experiments include XENON [2], CDMS [3], DAMA [4], CoGeNT [5], CRESST [6], and others, which will be further discussed in Sec. 2.2. Indirect detection looks for pair annihilation products of dark matter particles produced in the dark matter halo at the center of galaxies, including neutrinos and anti-neutrinos, electrons and positrons, and gamma rays, and experiments are commonly carried out by space telescopes. Major experiments in this category include EGRET [7], Fermi (GLAST) [8], PAMELA [9], and VERITAS [10]. Accelerator experiments aim to find dark matter particles by actually producing them through collision of high energy particles. Physicists at the Large Hadron Collider (LHC) look for signatures of dark matter, such as lepton jets and large missing transverse energy [11].

2.2 Direct Detection Experiments

Over the past decade, there has been major disagreement and debate between the results of several direct detection experiments. They are divided into experiments with null results, which include XENON [2] and CDMS [3], and experiments which claim discovery, which include DAMA [4], and recently CoGeNT [5].

In 2007, the XENON collaboration published the limits based on data obtained from 5.4 kg × 58.6 days of exposure [12]. XENON10, which is the detector of the XENON collaboration at that time, uses 5.4 kg liquid xenon as the target, and detects both scintillation and ionization signals from nuclear recoils of dark matter [2]. It achieved good background rejection using self-shielding and S2/S1 discrimination. During the run between Oct 2006 and Feb 2007, it found 10 events consistent with background (Fig. 2.1) and achieved the world's best limit at that time.

The CDMS experiment uses a Ge target which detects both ionization and phonon produced by nuclear recoil from dark matter [13], and achieved extremely good background rejection using ionization yield (ratio between ionization and phonon energy) and timing parameter (rise time of phonon pulse) discrimination. The previous runs of CDMS found zero events [14], and in the latest results released in Dec. 2009 [3], 2 events were found, while the expected background is 0.6 events, which is also consistent with null results (Fig. 2.2).

The DAMA experiment, on the other hand, uses NaI crystals as its target material, and detects scintillation due to nuclear recoils [4]. It is not a low background experiment compared to XENON and CDMS due to the intrinsic radioac-

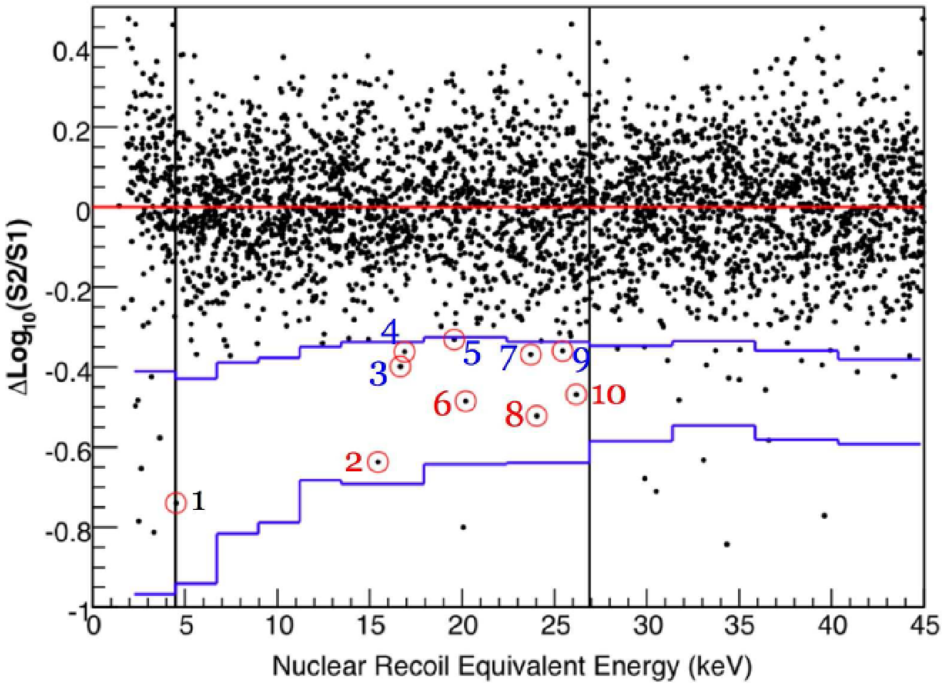

Figure 2.1: Events in the XENON10 data. Ten events were observed in the acceptance region (taken from [12])

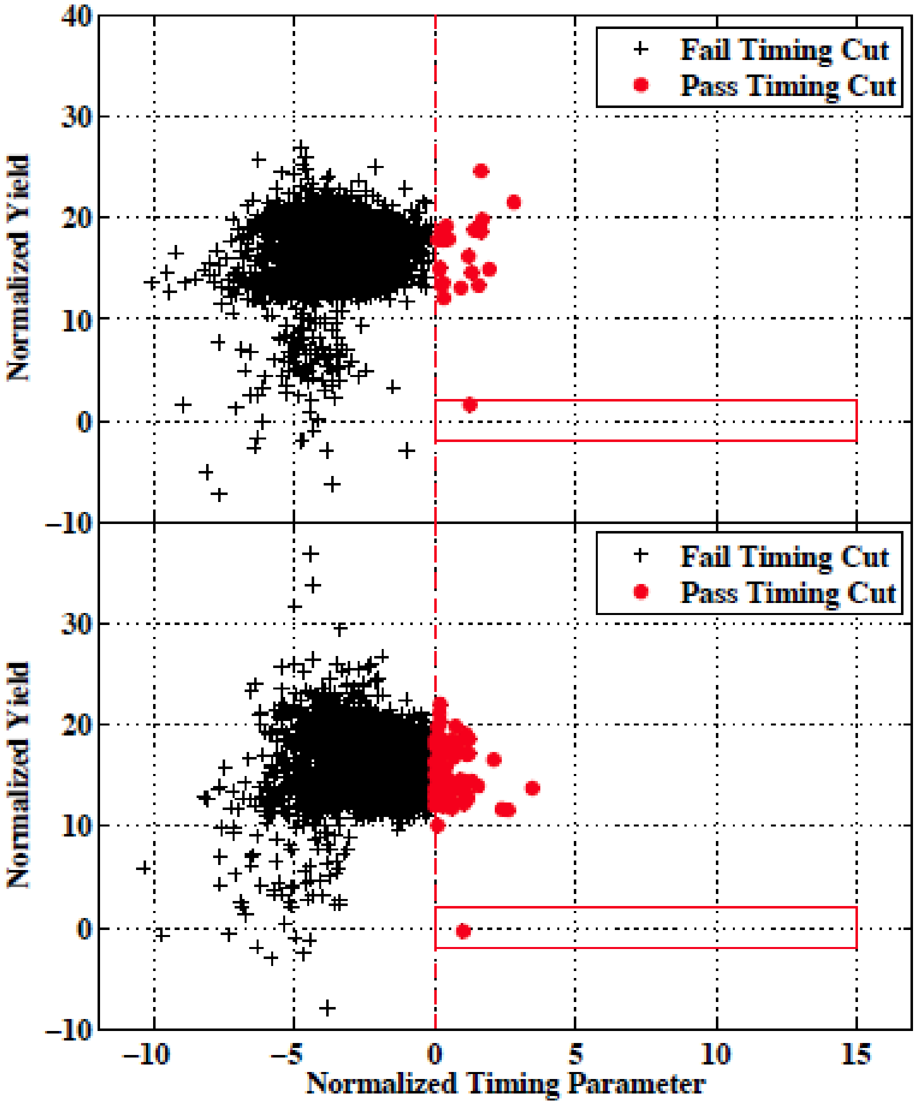

Figure 2.2: Events in the new CDMS data. Two events were observed in the acceptance region (red box). (taken from [3])

tive contaminants in the NaI crystals. However it found a signal which modulates annually and sinusoidally with a relative amplitude of a few percent [15] (Fig. 2.3). Based on this annual modulation, the authors claimed discovery of dark matter by noting that this high amplitude of modulation cannot be produced by any background, which were monitored and analyzed closely.

Another experiment, CoGeNT, released their results recently in 2010 [5]. In the low energy region of the event data (Fig. 2.4), an exponentially decreasing spectrum is found with ten's of events and is well the above the background. The energy spectrum between $0.4 - 3.2$ keVee is consistent with the energy spectrum of a dark matter signal (zoomed-in in Fig. 2.4). Together with DAMA, the results of CoGeNT show disagreement from the XENON and CDMS experiments.

However, theorists have found ways to explain the seeming inconsistency among the results of the above experiments. By fitting the recoil energy spectrum of the DAMA modulation amplitude and the CoGeNT event rate to the expected spectrum of the WIMP, the DAMA and the CoGeNT results are found to be compatible with WIMP signal of low WIMP masses, which are 10 and 7 GeV respectively. At the same time, due to the fact that

(1) the target nucleus of XENON is heavy, and

(2) the high energy threshold of XENON and CDMS compared to DAMA and CoGeNT,

the XENON and the CDMS detectors are relatively insensitive to light mass WIMPs. Hence DAMA and CoGeNT remain compatible with XENON and CDMS. The status of the cross section upper limit before the new results of the XENON and CDMS experiments is shown in Fig. 2.5. In addition to low WIMP mass WIMPS, theorists have also proposed inelastic dark matter (iDM) as an alternative explanation (detailed in Sec. 3.3.6.1). Based on this new model,

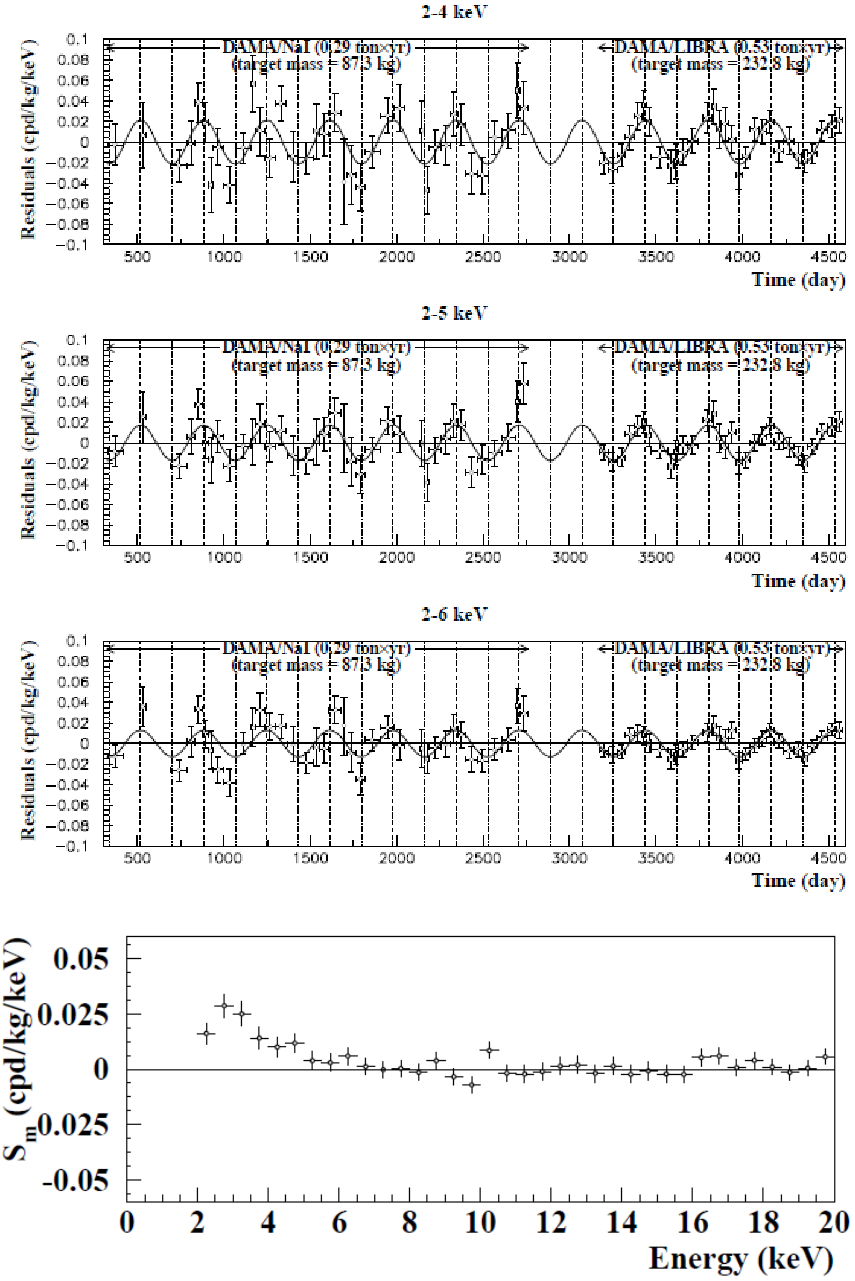

Figure 2.3: Top: Sinusoidal variation of the DAMA event rate. Bottom: Modulation amplitude as a function of the recoil energy. (Figures taken from [15])

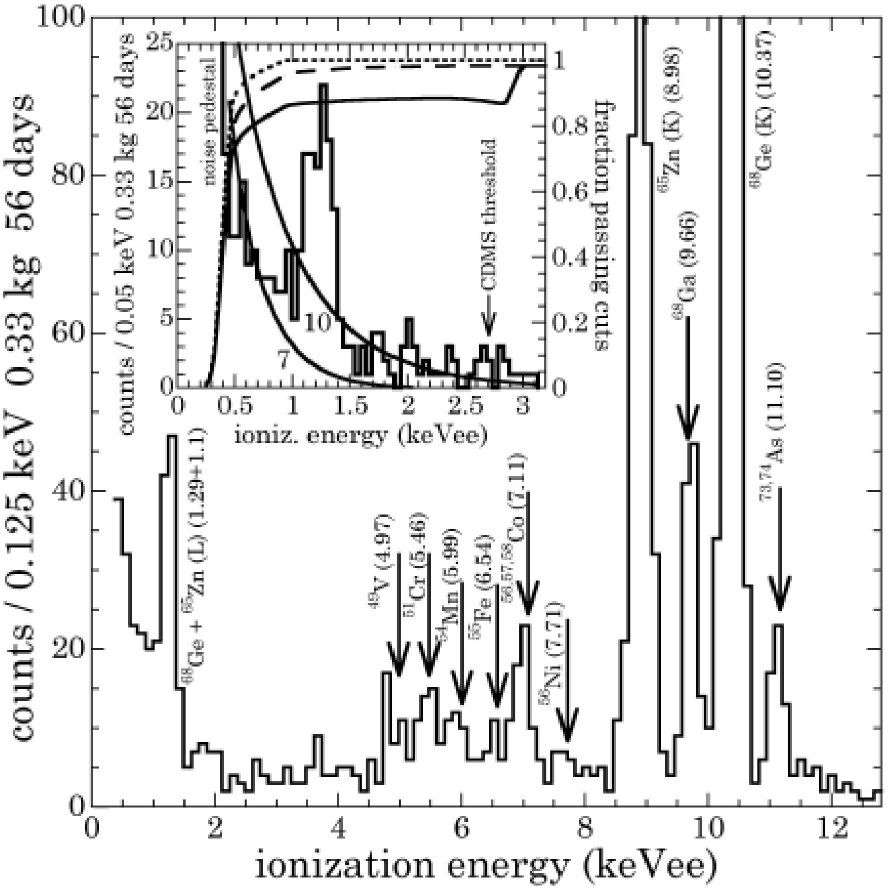

Figure 2.4: Energy spectrum of the CoGeNT data. The exponentially decreasing spectrum at low energy is consistent with a dark matter signal. (Figure taken from [5])

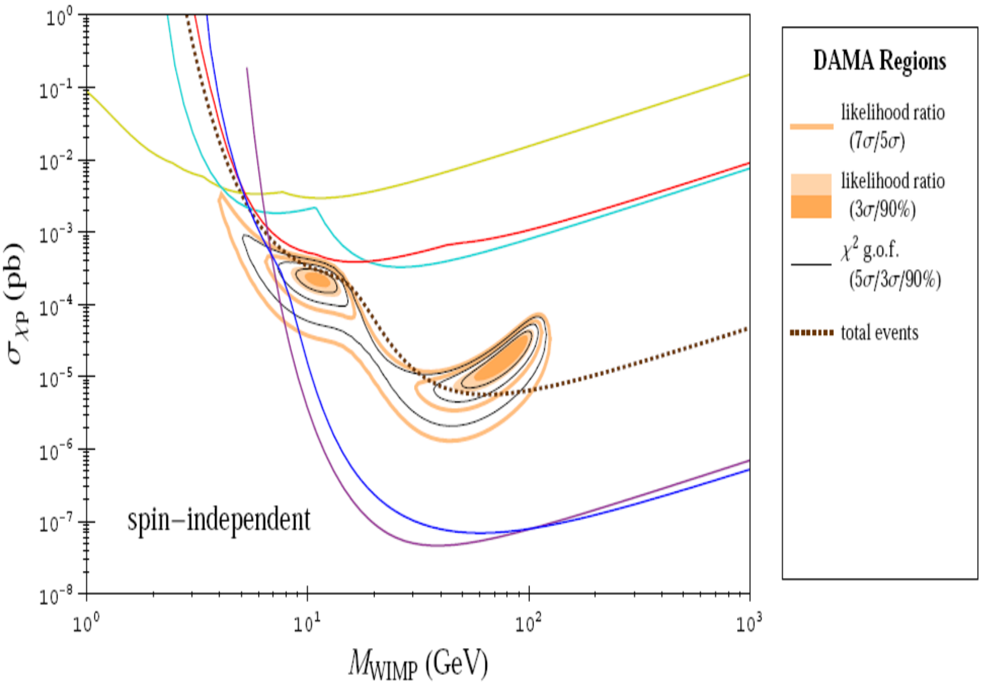

Figure 2.5: Status of the Spin-independent limits in 2009 before the release of the XENON100 and new CDMS results. Plot shows the allowed regions of DAMA (orange and black contours) and the upper limits of XENON10 (purple), CDMS (blue), CoGeNT (red), CRESST (yellow), and TEXONO (light blue). Figure taken from [16]

a new parameter is introduced and the energy spectrum of the dark matter signal is significantly modified, which allows for reconciliation between the experiments.

In the analysis of the XENON100 data, I will focus on the two explanations of the DAMA results: low mass WIMPs, and inelastic dark matter. While these two scenarios can reconcile the discrepancy between DAMA and other experiments, the XENON100 data, with increased exposure and better background rejection, will achieve better limit and shed light on the current situation. Here I look at the XENON100 data in these two models and draw conclusion based on the results.

2.3 Liquid Xenon as a Direct Detection Target

2.3.1 Spin-independent Interaction between WIMP and atomic nucleus

2.3.1.1 Recoil Energy Spectrum

WIMP in the dark matter halo can undergo elastic scattering with atomic nuclei. The differential event rate per unit nuclear mass for a recoil energy E_R is [17]

$$\frac{dR}{dE_R} = \frac{\rho_\chi \sigma}{2M_\chi \mu^2} F^2 \int \frac{1}{v} f(\vec{v}) d^3\vec{v} \tag{2.1}$$

where M_χ is the WIMP mass, σ is the WIMP-nucleus cross section, μ is the WIMP-nucleus reduced mass. The WIMP density of the dark matter halo ρ_χ is taken to be 0.3 GeV/c^2/cm^3. Since σ depends on the target material, we express σ in terms of the WIMP-nucleon cross section (Eq. 2.2) σ_n [16] (assuming the WIMP has same coupling to proton and neutron). In Eq. 2.2, the coherence factor A^2 enhances the event rate for heavier nuclei.

$$\sigma = \sigma_n (\frac{\mu}{\mu_n})^2 A^2 \tag{2.2}$$

2.3.1.2 WIMP Velocity Distribution

In Eq. 2.1, the differential cross section has been integrated over the velocity distribution $f(\vec{v})$ of the incident WIMP particle. The dark matter halo is assumed to have a Maxwellian velocity distribution $f(\vec{v}) \sim e^{-(\vec{v}+\vec{v}_E)^2/v_o^2}$ (where $\vec{v}_E$ is the velocity of the earth w.r.t. the halo) with a cutoff at the galactic escape velocity v_{esc}. The integral is carried between $|\vec{v}| > \frac{1}{\mu}\sqrt{\frac{M_N E_R}{2}}$ and $|\vec{v} + \vec{v}_E| < v_{esc}$, with $v_{esc} = 544$ km/s, and M_N is the nucleus mass. A WIMP characteristic velocity $v_o = 220$ km/s is assumed.

2.3.1.3 Form Factor Correction

The recoil energy spectrum describes the scattering process of a billiard-ball collision between two particles. However, due to the finite size of the atomic nucleus, it is necessary to correct the energy spectrum for the nuclear structure. The nuclear form factor F describes the structure of the nucleus and F^2 is multiplied to the energy spectrum in Eq. 2.1. It is the Fourier transform of the spatial density distribution of the nucleus. The commonly used Helm form factor (Eq. 2.3) has the advantage of giving an analytic expression [17] for faster computation and so is used here,

$$F(qr_n) = 3\frac{j_1(qr_n)}{qr_n} \times e^{-(qs)^2/2} \tag{2.3}$$

where $s = 0.9$ fm, q is the momentum transfer in the scattering process, r_n is the nuclear radius detailed in [17], and j_1 is the Bessel function of the first kind.

2.3.1.4 Event Rate for Xenon

Fig. 2.6 gives the recoil energy spectrum for different target materials assuming a WIMP mass of 100 GeV and a WIMP-nucleon cross section of 10^{-45} cm^2.

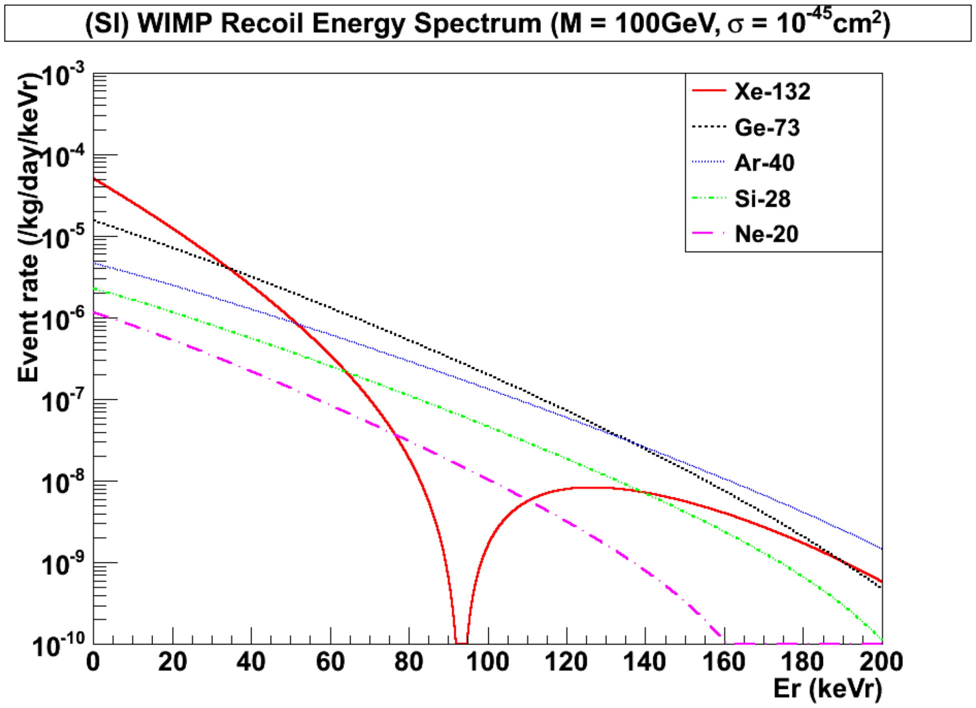

Figure 2.6: Recoil Energy Spectrum for Different Target Nuclei for a 100 GeV WIMP.

Because of the coherence factor A^2 in the energy spectrum, xenon, which has high atomic mass, is favored as a target for Spin-independent interaction. The dip at $\sim$ 95 keV for xenon is due to the form factor correction. The dips for lighter nuclei occur at higher recoil energies, which are not shown in the figure.

2.3.2 Spin-dependent Interaction between WIMP and atomic nucleus

In the case of spin-dependent elastic scattering, the scattering amplitude changes sign with spin-direction [17]. Since the scattering amplitude is summed over all nucleons in a nucleus, only nuclei with an odd number of protons or neutrons are more sensitive to spin-dependent interaction. A xenon atom has 54 protons, and there are isotopes of xenon with odd number of neutrons, ^{129}Xe and ^{131}Xe, with isotopic abundances of 26.4% and 21.2% respectively [18].

The recoil energy spectrum for spin-dependent elastic scattering is similar to Eq. 2.1, except that the WIMP-nucleus cross section [19] is given [16] by:

$$\sigma(q) = \frac{4\mu^2}{2J+1}(a_p^2 S_{pp}(q) + a_p a_n S_{pn}(q) + a_n^2 S_{nn}(q)) \tag{2.4}$$

In Eq. 2.4, J is the spin of the nucleus, and a_p and a_n are the WIMP couplings to proton and neutron. The structure functions [20] S_{pp}, S_{pn}, and S_{nn} replace the form factor correction.

2.3.3 Scintillation and Ionization Properties of Liquid Xenon

WIMP, neutrons, and gammas that interact with the LXe deposit energy in the form of a recoiling nucleus (for WIMP and neutron) or a recoiling electron (for gamma). The recoiling nucleus or electron travels along in the liquid and excites (Xe*) and ionizes (Xe$^+$) xenon atoms. An ionized xenon atom combines with another xenon atom, and some of them recombine with an electron, which, after a series of processes (Eq. 2.5), will be converted to an excited xenon atom (Xe^*). The excited xenon atoms combine with another xenon atom to become an excited dimer (Xe_2^*), which, upon de-excitation, emits scintillation photons of 175 nm wavelength [21]. The processes are illustrated in Fig. 2.7.

$$\mathrm{Xe}^* + \mathrm{Xe} + \mathrm{Xe} \rightarrow \mathrm{Xe}_2^* + \mathrm{Xe} \tag{2.5}$$

$$\mathrm{Xe}_2^* \rightarrow 2\ \mathrm{Xe} + h\nu \tag{2.6}$$

$$\mathrm{Xe}^+ + \mathrm{Xe} \rightarrow \mathrm{Xe}_2^+ \tag{2.7}$$

$$\mathrm{Xe}_2^+ + e^- \rightarrow \mathrm{Xe}^{**} + \mathrm{Xe} \tag{2.8}$$

$$\mathrm{Xe}^{**} \rightarrow \mathrm{Xe}^* + heat \tag{2.9}$$

$$\mathrm{Xe}^* + \mathrm{Xe} + \mathrm{Xe} \rightarrow \mathrm{Xe}_2^* + \mathrm{Xe} \tag{2.10}$$

$$\mathrm{Xe}_2^* \rightarrow 2\ \mathrm{Xe} + h\nu \tag{2.11}$$

The fractions of energy that goes to scintillation and ionization will change in the presence of an electric field. More importantly, it also depends on whether the energy deposition comes from a recoiling nucleus or a recoiling electron. This allows for discrimination between nuclear and electron recoils by the use of an S2/S1 cut, which will be further discussed in Sec. 3.2 and 3.3.1.1.

2.3.4 Energy scale: keVr and $\mathrm{keV_{ee}}$

Because of loss of energy to heat (phonon), not all of the energy deposited in the form of a recoiling nucleus or electron is converted into scintillation and ionization. Having a greater mass, a recoiling nucleus is more likely than an electron to lose energy by phonon by inelastic collision in the liquid xenon. This is referred to

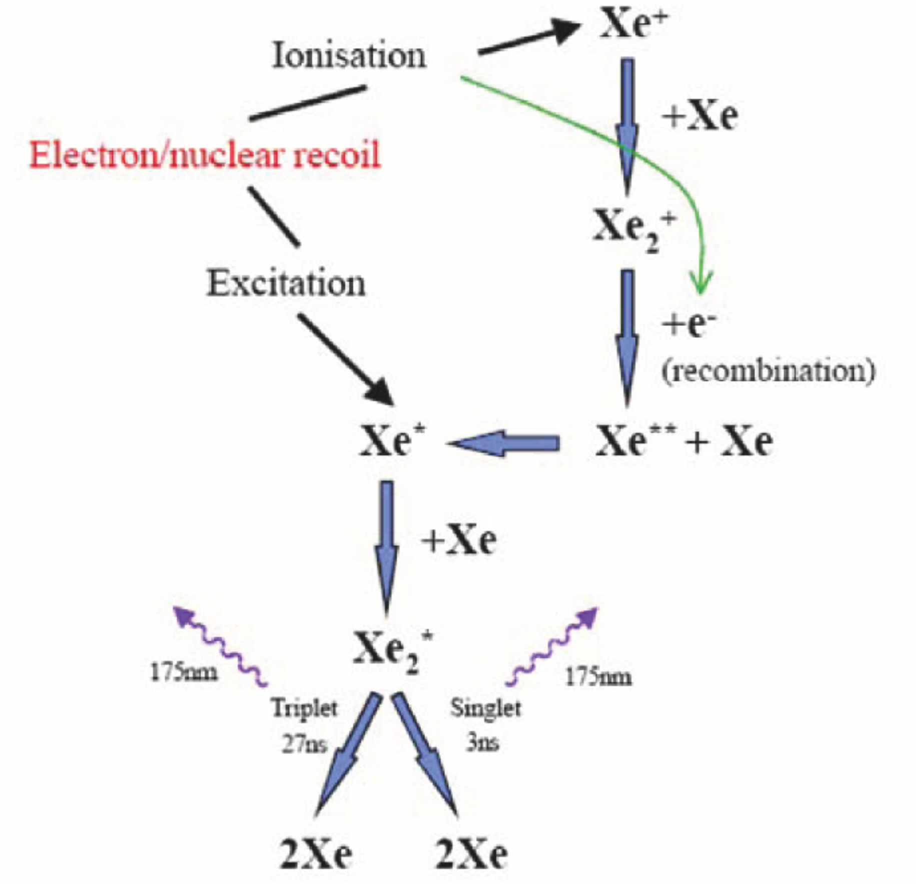

Figure 2.7: Scintillation and Ionization Process in Liquid Xenon. Figure taken from [22].

as 'quenching' for nuclear recoils. The scintillation efficiency of nuclear recoils depends on the kinetic energy of the recoiling nucleus as well as the strength of the electric field in the liquid xenon, and their relation is described in detail in Sec. 3.3.2. One defines keVr (or $\mathrm{keV_{nr}}$) to be the unit for energy values calculated from the number of photo-electrons assuming nuclear recoil scintillation efficiency. On the other hand, $\mathrm{keV_{ee}}$ is defined to be a unit linear to the number of detected photo-electrons in the detector. For the XENON100 detector, it is calculated using the light yield for ^{57}Co 122 keV γ rays.

CHAPTER 3

The XENON100 Experiment

3.1 Introduction

The XENON100 experiment, located at the Laboratori Nazionali del Gran Sasso (LNGS) under the Gran Sasso mountains in Italy, is designed for dark matter direct detection with liquid xenon as the target. It is an ultra-low background experiment utilizing the principle of time projection chamber. It is the successor of the XENON10 experiment by the XENON collaboration, based on the same detection principle but with greater target mass and better background rejection. Below I describe the non-blind analysis on the 11.17 days data, which were acquired in October and November 2009, and the results [23] released in May 2010 achieved one of the world's best limits to date.

3.2 The XENON100 Detector

In the XENON100 detector (Fig. 3.1), a total of 161 kg of liquid xenon (LXe) is contained a double-walled stainless steel cryostat at about -91 degrees Celsius. About 62 kg of the LXe is in a time projection chamber (TPC) made from a thin-walled (6 mm thick) Teflon cylinder (Fig. 3.2, top). The dimension of the LXe is 30.5 cm in diameter and 30.6 cm in height. Two arrays of Hamamatsu R8520 photomultipliers (98 at top, 80 at bottom) are embedded in Teflon structures at the top and the bottom of the TPC to detect scintillation light produced from dark matter particle interacting with xenon nuclei (Fig. 3.2, bottom). The Teflon cylinder acts as light reflector which increases the light collection efficiency of the detector. Between the liquid xenon and the top PMTs is a layer of gas xenon, which is crucial in the production of S2 signals which will be described below. The time projection chamber is further surrounded by a layer of 99 kg of LXe forming the veto region, which is equipped with additional 64 PMTs. A downward pointing electric field of 530 V/cm is applied in the LXe by a field cage made from wires around the cylinder and metal grid meshes near the top and the bottom of the liquid. A stronger electric field is applied in the GXe region between two meshes near the liquid-gas boundary.

When a particle (WIMP, gamma, or neutron) comes into the detector, there is a probability that it will interact with the LXe by scattering off of either a xenon nucleus (for WIMP or neutron) or an electron (for gamma). The recoiling nucleus or electron will then cause the liquid to scintillate, producing photon of 175 nm wavelength, and ionize xenon atoms as it travels along in the liquid. The scintillation light will be detected promptly by the top and the bottom PMTs and known as the primary or prompt scintillation signal (S1). On the other hand, the free electrons produced from ionization will be drifted upward by the electric field at a speed of 1.8 mm/μs. As the electrons reach the liquid-gas boundary and enters the high electric field region in the gas, it causes the gas to scintillate. The scintillation light is detected by the PMTs as the secondary or proportional scintillation signal (S2). The S1 and S2 signals together constitute the detection of an event. Having both an S1 and an S2 signal in an event is crucial to the principle of the XENON detector as follows. A WIMP particle interacts with the LXe only by nuclear recoils, while a gamma ray interacts only by electron recoils. An event from an electron recoil has a much greater S2/S1 ratio than

Figure 3.1: The XENON100 detector at LNGS.

Figure 3.2: Top: The Time Projection Chamber (TPC). Bottom: The top and bottom PMT arrays.

a nuclear recoil. Therefore using the S2/S1 ratio, one can discriminate gamma events from WIMP events effectively, which greatly reduces background events due to gammas (see Sec. 3.3.1.1 for the analysis). In addition, the time delay between the S1 and the S2 signal allows for determination of the z position of an event, and the S2 signal of each event creates a hit pattern for the top PMTs, which allows for determination of the x and y position of the event (Sec. 3.2.1). The x, y, and z position information allows for fiducialization of the detector volume, which is useful in reducing background events from decays of radioactive contaminants in materials around and external to the LXe.

3.2.1 Position Reconstruction

The fiducialization of the detector is implemented in the analysis as a software cut, which selects events with their position within the fiducial region, and it is described in Sec. 3.3.1. The z position of an event can be determined by the time difference between the S1 and the S2 signal, i.e. the drift time, which is equal to the time it takes for the ionization electrons to be drifted up from the event location to the liquid-gas boundary by the electric field. The x and y position can be determined by position reconstruction algorithms which take the hit pattern of the top PMTs of the S2 signal as the input. It is based on the fact that the PMTs that are directly above the event location will have the highest signal output. In the analysis of the 11.17 days data, three different position reconstruction algorithms were used: χ^2 minimization, support vector machine regression (SVM), and neural network (NN). The algorithms were trained using Monte Carlo simulations results with the GEANT4 code. The three algorithms produced consistent results inside the fiducial volume, with the x and y resolution better than 3 mm as determined from calibration with a collimated gamma source [24].

3.2.2 Radioactive Backgrounds

In dark matter direct experiments, one expects zero or very few dark matter events to be observed. Hence one of the major challenges in improving the sensitivity of the detector is to limit the number of background events. Background events are gamma rays or neutrons which also interact in the LXe with electrons or xenon nuclei. They may come from

(1) decays of radioactive contaminants in detector components, such as the PMTs, the Teflon cylinder, the stainless steel cryostat, and the detector shielding,

(2) gamma and neutrons from radioactivity in the rocks in the Gran Sasso lab,

(3) high energy neutrons produced from cosmic-ray muons interacting with the rocks, and

(4) intrinsic contaminants in the LXe, such as ^{85}Kr.

Radioactive contaminants in detector components mainly include ^{238}U, ^{232}Th, ^{40}K, and ^{60}Co, which decay and produce gamma rays and α particles. The α particles then interact with the detector materials and produce neutrons by an (α, n) reaction. The techniques used in reducing the background include fiducialization of the detector volume (Sec. 3.3.1.2), distinguishing electron recoils from nuclear recoils by S2/S1 discrimination (Sec. 3.3.1.1), and external shielding of the detector, which consists of a 20 cm thick layer of polyethylene and a 20 cm thick outer layer of lead. The ^{85}Kr level in the XENON100 detector is reduced by orders of magnitude by partial distillation through the Krypton distillation column. The Kr level was measured to be 143 (+130 $-$ 90) ppt, which gives close to zero background events for the 11.17 days data of interest. Monte Carlo simulations of the GEANT4 code show that the expected background in the WIMP search region is less than 0.2 events for the 11.17 days data, and so the probability of observing 1 or more background events is less than 20%. No background subtraction is applied when deriving the resulting limit.

3.3 Data Analysis

3.3.1 Software Cuts and Acceptance

3.3.1.1 S2/S1 Cut

As described in Sec. 3.2, one of the advantages of the XENON100 detector is its ability to effectively discriminate electron recoil (ER) background due to gamma rays from nuclear recoil (NR) signal due to WIMP events. By defining an acceptance region in the parameter space of $\log_{10}(\mathrm{S2/S1})$ and $S1$, most of the electron recoil events, which has a higher value of $\log_{10}(S2/S1)$ than nuclear recoil events, can be rejected. The acceptance region is defined by calibrating the detector with radioactive sources. A ^{60}Co source, which produces gamma rays of 1.17 and 1.33 MeV, was used for calibration of the electron recoil band. A ^{241}AmBe neutron source was used for calibration of the nuclear recoil band. Fig. 3.3 shows the data in the electron recoil (top) and the nuclear recoil (bottom) calibration. The data are shown for the chosen fiducial volume of 40 kg and the energy window of $4-20$ photo-electrons (PE) (vertical dashed lines). An S2 software threshold of 300 PE (long dashed line) is applied in the data. The blue and the red lines show the median value of of $\log_{10}(\mathrm{S2/S1})$ for the electron and the nuclear recoil events respectively. The acceptance region is defined to be below the neutron median, which gives an acceptance of 50% for the S2/S1 cut.

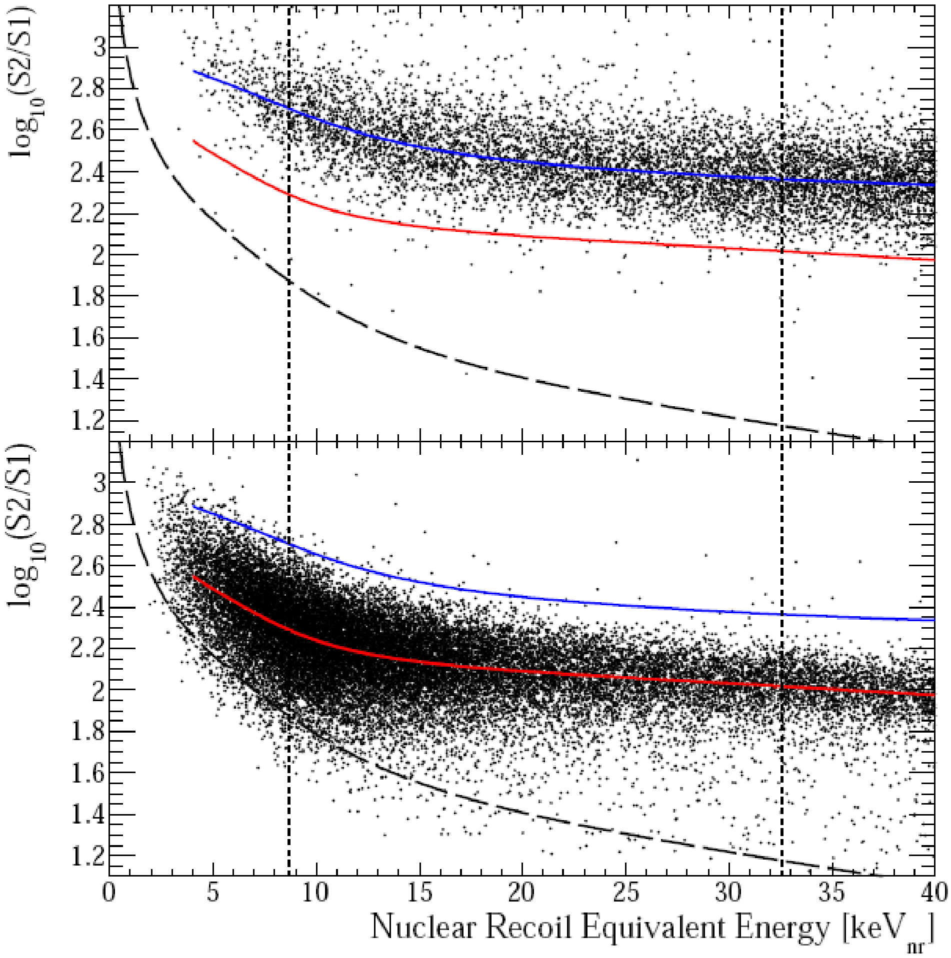

Figure 3.3: $\log_{10}$(S2/S1) as a function of recoil energy for ^{60}Co (top) and ^{241}AmBe (bottom) calibration data. The electron and nuclear recoil band median values are shown as blue and red lines. Also shown are the WIMP search window between 4 – 20 PE (vertical dashed lines) and the S2 software threshold of 300 PE (long dashed line). Figure from Ref. [23].

Since the nuclear recoil and the electron recoil events follow Gaussian distributions centered near the neutron and electron medians respectively, the choice of the neutron median as the boundary of the acceptance box is favored for being able to maximize the acceptance and minimize the electron recoil backgrounds. As seen in Fig. 3.3 (top), most of the electron recoil events are above the neutron median and are rejected by the cut. The rejection efficiency of the S2/S1 cut is determined to be above 99% by counting events in the electron recoil calibration data. This rejection efficiency happens to be sufficient for the 40 kg $\times$ 11.17 days data, as it gives an expected background of less than 0.2 events between the $4 - 20$ PE WIMP search window.

3.3.1.2 Fiducial Volume Cut

One of the techniques to reduce the background in the XENON100 detector is self-shielding of the liquid xenon. A fiducial volume is defined in the detector which consists of an inner central portion of the LXe, and the rest of the xenon is considered as a passive shield. Only events that occur within the fiducial volume are counted toward the data. This passive shielding of liquid xenon, a high density material, effectively prevents gamma rays and neutrons, produced from decays of the radioactive contaminants in detector components, from reaching the fiducial volume. The radioactive background can thus be greatly reduced, as shown in Fig. 3.6 for the 11.17 days data as an example. The fiducial volume cut is defined to select the events with $r < 135$ mm and -276 mm $< z < -33$ mm, which corresponds to a self-shielding of 33 mm, 29 mm, and 17.4 mm at the top, bottom, and side respectively.

3.3.1.3 Multiple-hit Cut

One way to discriminate background events from WIMP signal events is to reject events with more than one scatters in the detector volume. Due to its low scattering cross section, a WIMP particle that enters the LXe does not interact with more than one xenon nucleus. On the other hand, background events from gamma rays and neutrons may scatter off of more than one electron or xenon nucleus, producing two or more hits in a single event. Although these multiple hits occur within a few ns, they can be seen separately in the form of multiple S2 signals. The difference in z locations of two hits is translated into a time separation of two S2 signals, as given by the drift velocity of the electrons which is 1.8 mm/μs. The multiple hit cut is defined to be a software cut that reject events with their second largest S2 signal greater than 300 photoelectrons. The choice of 300 PE is a balance between

(1) rejecting events that are real multiple scatters and

(2) keeping events that is a single scatter but with a noise peak that is accidentally too large and is misidentified as a second S2 signal.

$$Area\ of\ 2nd\ largest\ S2\ peak < 300\ \mathrm{PE} \tag{3.1}$$

3.3.1.4 Veto Anti-coincidence Cut

In the same spirit of removing background, an active-veto anti-coincidence cut is applied to remove events from a particle that interacts not only in the fiducial volume, but also in the active veto region. Similar to the multiple hit cut, this can reduce background events that scatter more than once in the detector. The cut is defined to keep only events that have no signal peaks in the veto region within 100 ns of the largest S1 peak:

$$(Coincidence\ of\ largest\ veto\ peak < 1) \tag{3.2}$$

or

$$(Time\ difference\ between\ largest\ S1\ peak\ and\ largest\ veto\ peak > 100\ \text{ns}) \tag{3.3}$$

3.3.1.5 2-fold PMT Coincidence Cut

A software cut is applied to remove events that may come from a PMT dark count, or a single electron S2 signal misidentified as an S1 signal. This cut keep only events with more than one PMT hit in the S1 peak:

$$Coincidence\ of\ largest\ S1\ peak > 1 \tag{3.4}$$

3.3.1.6 Signal-to-noise Ratio Cut

A software cut is applied to reject events with their noise level too high. This cut is defined to keep only the events with the sum of the S1 and S2 signals greater than the time integral of the noise:

$$(S1 + S2)/(Total\ area - S1 - S2) > 1 \tag{3.5}$$

3.3.1.7 Other Software Cuts

Other software cuts that are used include a cut that remove anomalous events with more than one S1 peaks. This cut is defined to reject events with a second S1 peak that has at least a 2-fold PMT coincidence. An S2 width cut is applied to remove some of the events that happen above the anode. Some software cuts are applied to remove events from a few of the PMTs that that has too high noise level.

3.3.1.8 Total Acceptance of the Software Cuts

While the software cuts described above reject events that are due to gamma and neutron background, they also potentially remove dark matter signals. This results in a loss of efficiency of the detector. In order to calculate the cross section upper limit in Sec. 3.3.5, one needs to obtain the acceptance of the software cuts, which is the probability that a WIMP event will pass all the cuts. This acceptance is determined experimentally by analyzing the ^{241}AmBe neutron calibration data. This is based on the assumption that WIMP events have the same acceptance as neutron events, since both of them are due to nuclear recoils. Since we know that a WIMP signal is always a single scatter while a neutron could be multiple scatters, the multiple-hit cut and the veto anti-coincidence cut are not included when determining the acceptance. Also, this efficiency does not include the acceptance of the S2/S1 cut, which is found separately to be 50% in Sec. 3.3.1.1. The acceptance is then computed using the neutron calibration data as:

$$\frac{Number\ of\ events\ passing\ all\ cuts}{Number\ of\ events\ passing\ all\ cuts + Number\ of\ events\ failing\ exactly\ one\ cut} \tag{3.6}$$

where the set of cuts considered in the above expression include the 2-fold PMT coincidence cut, the signal-to-noise ratio cut, and the remaining cuts in Sec. 3.3.1.7. The reason that the neutron events that fail two or more cuts are not counted towards the calculation of the acceptance is that they are considered to be non-valid events which will not occur in WIMP signals. This was confirmed by visual inspection of the waveforms of hundreds of such events [24]. The efficiency of the detector (not including the S2/S1 acceptance), or the total software cut accep-

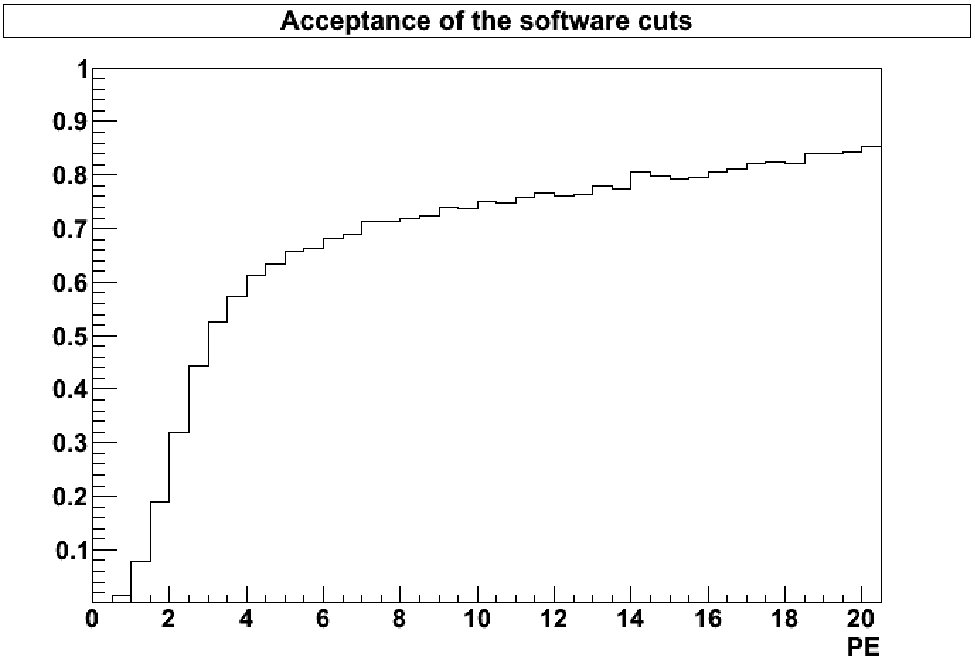

Figure 3.4: Acceptance of the software cuts vs. number of detected photo-electrons.

tance, is shown in Fig. 3.4 as a function of number of photoelectrons. It is about 65% at 4 PE and rises to about 90% above 35 keVr.

3.3.2 Nuclear Recoil Scintillation Efficiency

In the XENON100 detector, the recoil energy of a particle scattering off of a xenon nucleus is measured by detecting the light from the prompt scintillation (S1). Since the amount of scintillation light is not proportional to the recoil energy, several measurements of the scintillation efficiency were carried out in the range of recoil energy of interest to find out the dependence of scintillation light on the nuclear recoil energy. To account for the fact that the amount of scintillation light produced varies among different detectors depending on the detector geometry and light collection, measurements results are expressed relative to a reference point of energy, which is the scintillation signal of 122 keV γ rays from radioactive ^{57}Co isotopes. Also, in the presence of an electric field, the scintillation light is reduced, which can be characterized by a constant factor. Hence the recoil energy can be expressed in terms of the S1 scintillation signal as:

$$E_{\mathrm{nr}} = S1/L_y \cdot 1/\mathcal{L}_{\mathrm{eff}}(E_{\mathrm{nr}}) \cdot S_{\mathrm{ee}}/S_{\mathrm{nr}} \tag{3.7}$$

Here L_y is the light yield of 122 keV γ rays, which was measured to be 2.2 PE/keV$_{\mathrm{ee}}$ in the XENON100 detector. S_{ee} and S_{nr} are quenching factors of electron and nuclear recoils respectively due to the electric field, and were measured to be 0.58 and 0.95 at 530 V/cm at which the detector is operated [25]. The Lindhard factor [26], $\mathcal{L}_{\mathrm{eff}}$, is the scintillation efficiency of nuclear recoils relative to 122 keV γ rays. Several sets of measurements of $\mathcal{L}_{\mathrm{eff}}$ were made in the range of 3.9 − 100 keVr with varying results, all with large statistical errors. For the purpose of choosing the $\mathcal{L}_{\mathrm{eff}}$ values for further calculations, three different fits to the measurements data are described below, and the final results obtained from the different fits are compared (Sec. 3.3.5).

3.3.2.1 Fits to $\mathcal{L}_{\mathrm{eff}}$ Measurements

Global best fit A global fit to all the available sets of direct measurements data is made in Fig. 3.5 (top). The fit utilizes the data points of the experimental measurements ([27], [28], [29], [30], [31], [32], and [33]) as well as their uncertainty values. A cubic-spline fit is performed, with the spline knots fixed at 5, 10, 25, 50, 100 keVr. Above the highest spline point 100 keVr, a constant value of $\mathcal{L}_{\mathrm{eff}}$ is assumed. Below the lowest spline point 5 keVr, a linear extrapolation assuming constant value of $\mathcal{L}_{\mathrm{eff}}$, as implied by the trend of the Aprile *et al.* data points [32], is used for the global fit.

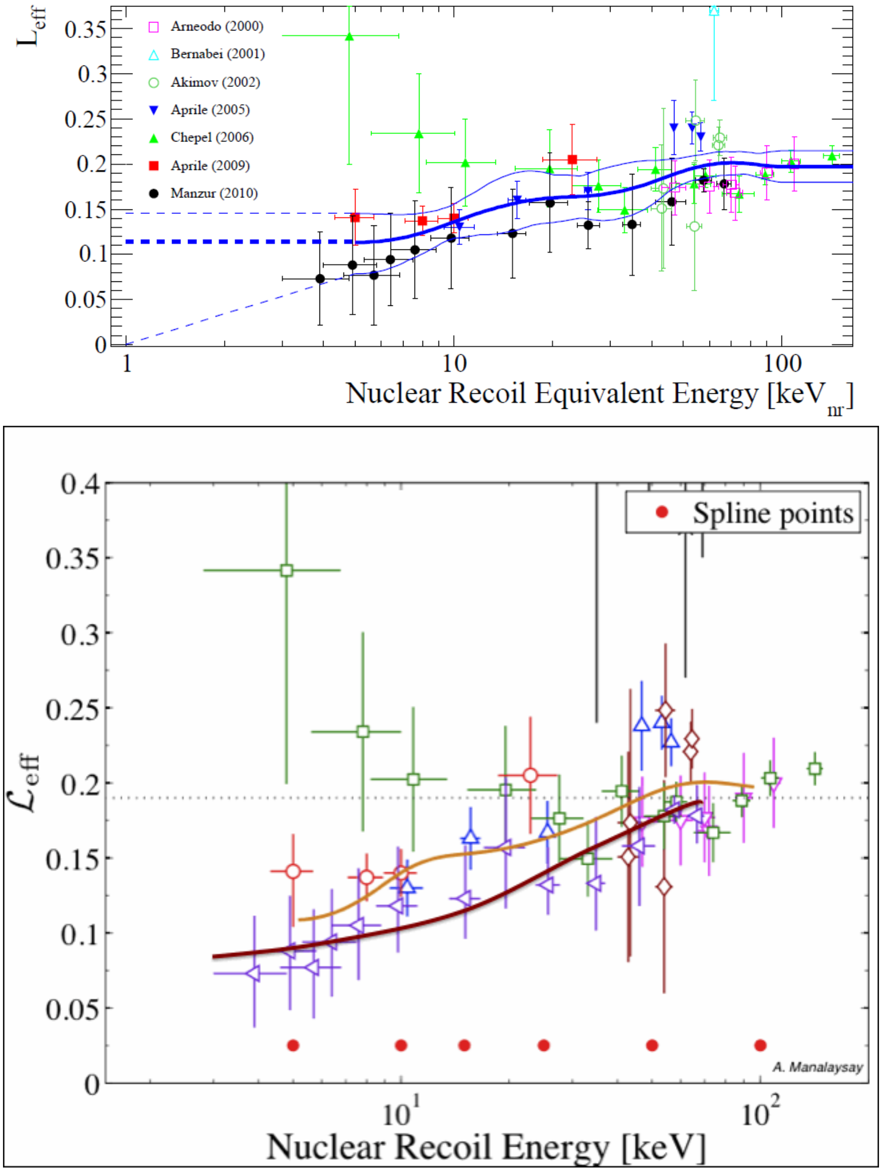

Figure 3.5: Top: Global fit to $\mathcal{L}_{\text{eff}}$ measurements (thick blue curve) and the 90% confidence contours (thin blue curves) (Figure from Ref. [23]). The linear and logarithmic extrapolations at low energy are shown in dashed lines. Bottom: Fit to Yale $\mathcal{L}_{\text{eff}}$ measurements (red) with a logistic function. The global best fit is also shown (orange curve) for comparison.

Lower 90% Confidence Contours of the global fit We also consider the 90% confidence contours of the global fit, which are shown as the thin lines in Fig. 3.5 (top). From Eq. 3.7, it can be seen that a lower $\mathcal{L}_{\text{eff}}$ value will give a higher recoil energy for a given number of photo-electrons. Since the WIMP recoil energy spectrum is exponentially decreasing, a higher energy window will result in fewer expected dark matter events. Therefore, aside from the global fit, the results are also computed using the lower 90% confidence contour and consider it as the most conservative choice. Similar to the global fit, a constant value of $\mathcal{L}_{\text{eff}}$ is assumed above the highest spline point 100 keVr. Below the lowest spline point 5 keVr, a logarithmic extrapolation is made using a slope from the lowest Manzur *et al.* data points, which shows a trend of decreasing $\mathcal{L}_{\text{eff}}$. This extrapolation gives lower $\mathcal{L}_{\text{eff}}$ values, and so is consistent with the fact that the fit is being used as the conservative case.

Manzur fit Due to the large experimental uncertainties of $\mathcal{L}_{\text{eff}}$, I also consider an additional fit based on results from a single set of measurements. A fit to the Manzur *et al.* (Yale) measurements [33] is used as an intermediate case between the global fit and the lower 90% confidence contour mentioned above. The fit to the Yale data is done using a logistic function (Eq. 3.8), with fit parameters $c_0 = 4.852 \times 10^{-2}$, $c_1 = 7.906$, $c_2 = 0$, and $c_3 = 0.1953$.

$$\mathcal{L}_{\text{eff}}(E) = c_3 \times (c_2 + \frac{1 - c_2}{1 + e^{-c_0(E - c_1)}}) \tag{3.8}$$

The fit curve is shown in Fig. 3.5 (bottom). Since the measurements were made between 3.9 – 66.7 keVr, assumptions need to be made for the $\mathcal{L}_{\text{eff}}$ values beyond this range. Again, above the highest data point 66.7 keVr, a constant value of $\mathcal{L}_{\text{eff}}$ is assumed. Below the lowest data point 3.9 keVr, a linear extrapolation assuming constant value of $\mathcal{L}_{\text{eff}}$ down to zero recoil energy is used similar to the global fit.

3.3.3 Energy Resolution

When calculating the sensitivity of the XENON100 detector, two detector effects, the detector efficiency (detailed in Sec. 3.3.1.8) and the energy resolution, need to be considered. Since these two effects start to dominate at low recoil energy, they become important limiting factors of the sensitivity of the detector at low WIMP mass range where majority of recoils are expected to be at low energy (Sec. 2.3.1). To properly estimate the expected number of WIMP events in the energy window, the finite energy resolution of the detector needs to be taken into account. In the XENON100 detector, the nuclear recoil energy of an event is obtained by measuring the number of photo-electrons detected by the PMTs. The number of photo-electrons that are detected is much smaller than the number of photons produced in a scattering event. This is due to the finite light collection efficiency of the detector as well as the quantum efficiency ($\sim 30\%$) of the PMTs. Therefore one can assume that the number of detected photo-electrons follows a Poisson distribution. To account for the finite energy resolution when calculating the limits, the expected WIMP energy spectrum is obtained by convoluting the theoretical spectrum given in Sec. 2.3.1 with a Poisson distribution, so that the spectrum is redistributed, or 'smeared'. The calculation of smearing is done as shown in Eq. 3.9, where $\frac{dR}{dE}$ and $\frac{dR}{dE'}$ are the smeared spectrum and the theoretical spectrum, and n is the number of detected photo-electrons. In Eqs. 3.10 and 3.11, ϵ relates the recoil energy to the number of photo-electrons according to the measured light yield and the scintillation efficiency as detailed in Eq. 3.7.

$$\frac{dR}{dE} = \frac{1}{n!\epsilon(E)} \int \frac{dR}{dE'} (\frac{E'}{\epsilon(E')})^n e^{-(E'/\epsilon(E'))} dE' \tag{3.9}$$

$$E = n \cdot \epsilon(E) \tag{3.10}$$

$$\epsilon(E) = 1/L_y \cdot 1/\mathcal{L}_{\text{eff}}(E) \cdot S_{\text{ee}}/S_{\text{nr}} \tag{3.11}$$

After smearing the energy spectrum, the detector efficiency (Fig. 3.4), which begins to roll off at about 5 keVr, is then multiplied to the energy spectrum to give the final expected results. Finally, because of the steepness of the energy spectrum, the sensitivity of LXe detectors strongly depends on the energy threshold. Due to unknown factors that could affect the efficiency and that the efficiency may not be well determined at low energy, a threshold of 4PE has been chosen for the XENON100 results. However, three different cases of 4PE, 3PE, and 2PE threshold are considered here to investigate the possibility of improving low WIMP-mass sensitivities by lowering the energy threshold.

3.3.4 Dark Matter Data

The results shown here are based on a non-blind analysis of 11.17 live days of data acquired in October and November 2009. Fig. 3.6 (top) shows the location of each event in the TPC cylinder. The external background has been greatly reduced by defining a fiducial region of 40 kg (dashed line). We consider only events in the energy window of $4 - 20$ PE and use the global fit of $\mathcal{L}_{\text{eff}}$ to convert the unit of photoelectrons to energy. After applying the software cuts, there are 22 events remaining in the fiducial region (black dots). In addition, the S2/S1 cut is used to discriminate electron recoil backgrounds. Fig. 3.6 (bottom) shows the $\log_{10}$(S2/S1) values of the remaining events and the effect of the S2/S1 cut. Most of the events fall around the electron median (blue), which is indicative of being γ events. The acceptance region is defined to be below the neutron median (red), which leads to a 50% acceptance of neutron and WIMP events as described in Sec. 3.3.1.1. After applying the S2/S1 cut, no events are observed in the fiducial

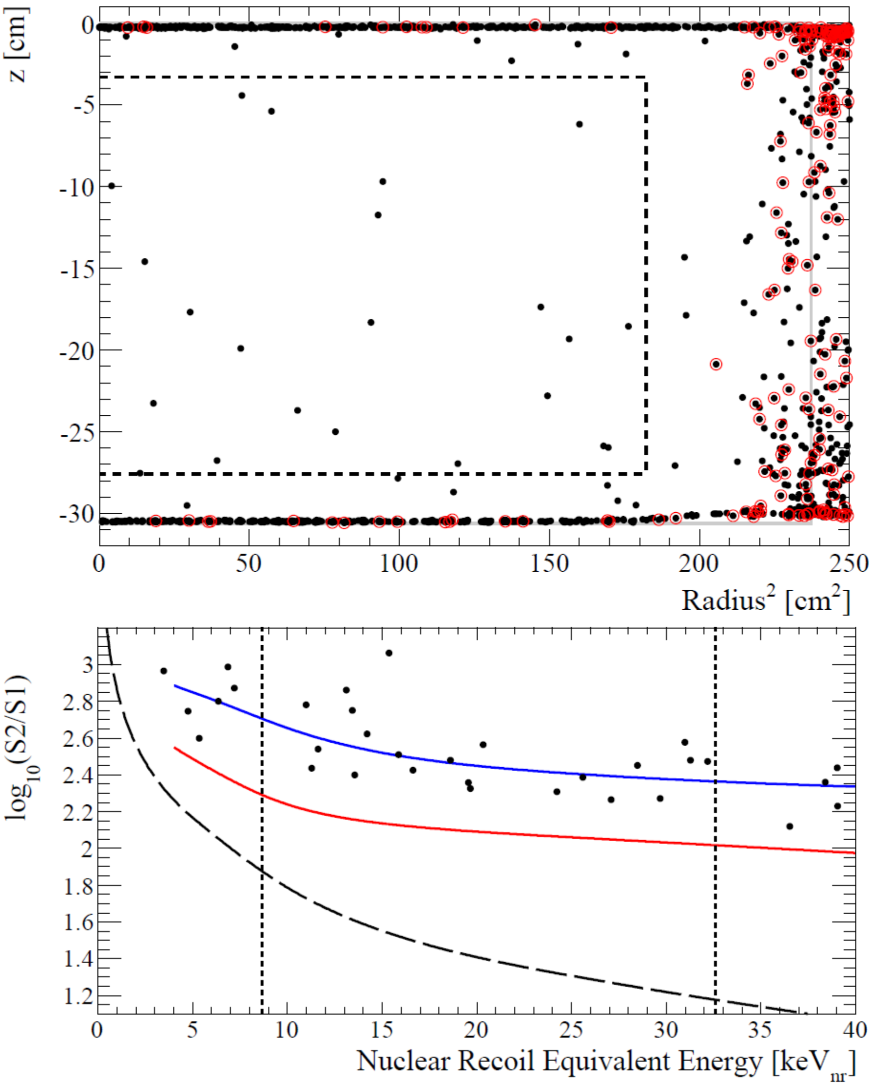

Figure 3.6: Top: r vs z distributions of all events (dots) in the 11.17 days data set and below the neutron median (red circles) in the 8.67 – 32.59 keVr (4 – 20 PE) energy window. Bottom: $\log_{10}$(S2/S1) as a function of recoil energy in the 40 kg fiducial region during the 11.17 days (The 4 – 20 PE energy window and the S2 software threshold of 300 PE are indicated by vertical dashed lines and long dashed line). Figures taken from Ref. [23].

region (red dot), which our calculation of the cross section upper limit will be based on.

3.3.5 Case Studies of DAMA and CoGeNT

3.3.5.1 Introduction

The allowed regions suggested by the DAMA [15] and the recent CoGeNT [5] results appear in the low WIMP mass range. Although most of these regions have been ruled out by the current limits of previous experiments, there are still remaining areas that are still allowed. It becomes important to consider the possibility of the 40 kg × 11.17 days data being able to exclude all of the DAMA and the CoGeNT areas. For the DAMA region I consider a benchmark case of 10 GeV WIMP mass and 10^{-5} pb WIMP-nucleon cross section, and for the CoGeNT region the case of 7 GeV WIMP mass and 5×10^{-5} pb cross section is considered. The DAMA and CoGeNT allowed regions are taken from [16] and [5].

3.3.5.2 Recoil Energy Spectrum at Low WIMP Masses

As shown in Sec. 2.3.1, the recoil energy spectrum of WIMP-nucleon elastic scattering is exponentially decreasing in general. The shape of the recoil energy spectrum is affected by (1) the incident velocity of the WIMP as determined by the WIMP velocity distribution in the dark matter halo, (2) kinematics of the collision between the WIMP and the atomic nucleus, and (3) the structure of the atomic nucleus which determines the nuclear form factor. The most relevant factor when looking at the case of DAMA and CoGeNT and their allowed region is the mass of the WIMP, which is relatively low in the parameter space and lies below 15 GeV. As expected from kinematics, the recoil energy of the nucleus tends to be lower when the WIMP is less massive compared to the nucleus. Therefore the shape of the recoil energy spectrum varies with the WIMP mass in a way such that it is steeper and decreases more sharply for lower WIMP mass, and this is more so for heavy target, or, as in our case, xenon nucleus. This leads to very few expected WIMP events and low sensitivity for xenon detectors. Therefore, in order to achieve better sensitivity in the lower WIMP mass range, it is important for our detector to be able to have a low energy threshold, i.e. the lower bound of the energy window, as the expected number of WIMP-induced recoils decreases quickly with increasing recoil energy.

3.3.5.3 Energy Spectra and Cross Section Limits for Different $\mathcal{L}_{\mathbf{eff}}$ Fits

Here I apply the three $\mathcal{L}_{\rm eff}$ fits described in Sec. 3.3.2.1 and investigate the energy spectra for the DAMA and the CoGeNT benchmark points respectively. I also compare the cross section upper limits for the different fits based on the 40 kg × 11.17 days data, which has no observed events even with 2 PE threshold. The expected background between $2-20$ PE is less than 0.2 events and so is negligible.

3.3.5.4 Best global fit

The theoretical spectrum, without detector effects, is shown in Fig. 3.8 and 3.9 (top, dashed black) for the DAMA and CoGeNT benchmark cases. The spectrum is close to 0 above 3PE, and in the case of CoGeNT, very low even at 2PE. However, thanks to the finite energy resolution of the detector, the spectrum is redistributed (solid black), and many low energy WIMP events are observed above the energy thresholds due to Poisson fluctuations. The energy dependent detector efficiency (Fig. 3.7) reduces the spectrum at low energy and gives the

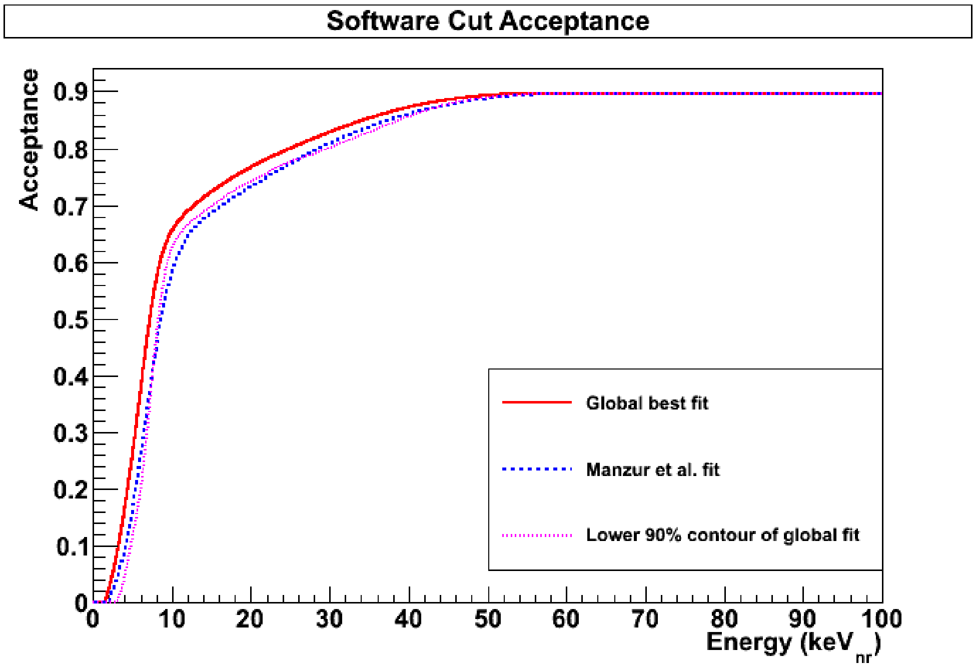

Figure 3.7: Acceptance of the software cuts for different $\mathcal{L}_{\rm eff}$ fits. Solid red: global best fit. Dashed blue: Manzur *et al.* fit. Dotted pink: lower 90% confidence contour of the global fit.

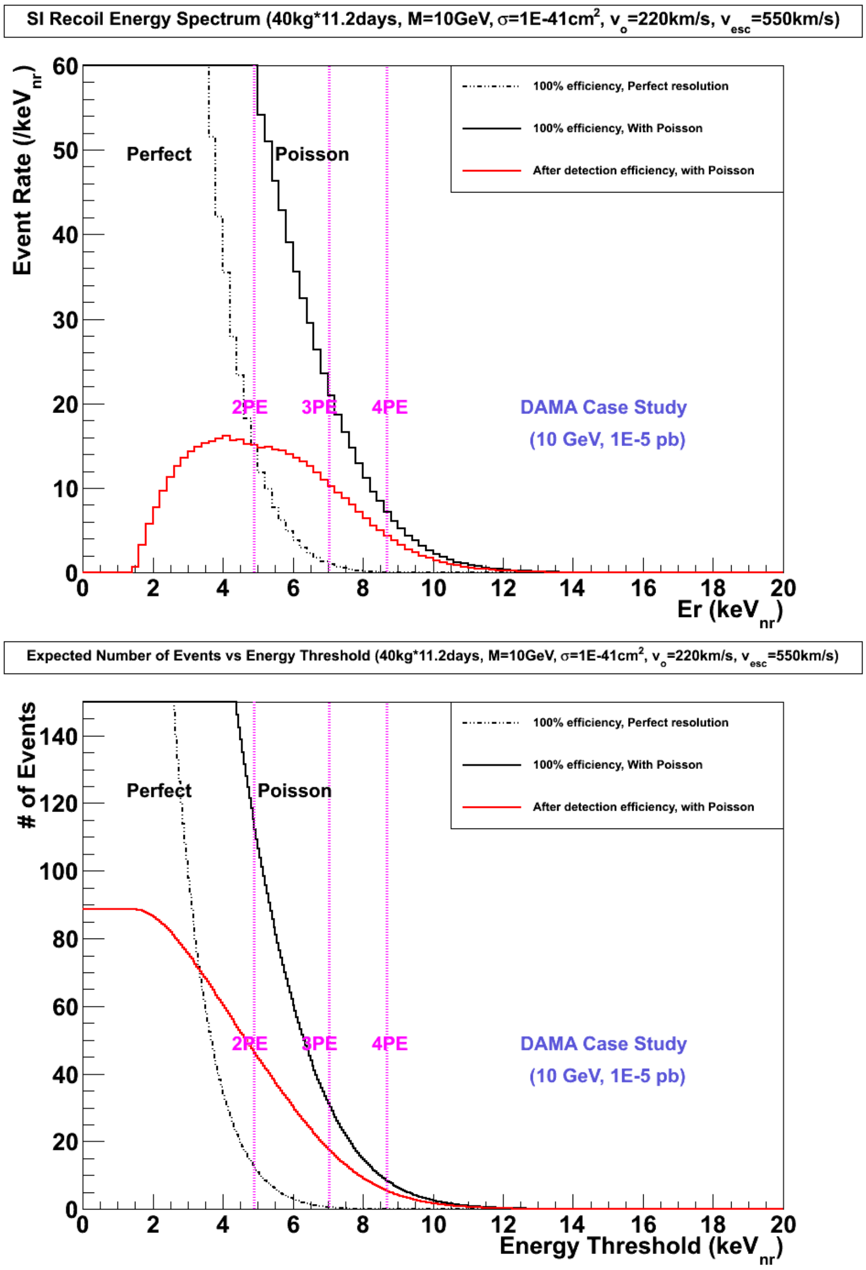

Figure 3.8: Top: WIMP Energy spectrum for perfect energy resolution (dashed black), finite energy resolution (solid black), finite energy resolution with efficiency (red) at 10 GeV WIMP mass and 10^{-5} pb cross section, using the best global fit to $\mathcal{L}_{\text{eff}}$. Bottom: Number of WIMP events as a function of energy threshold for the 40 kg × 11.17 days data.

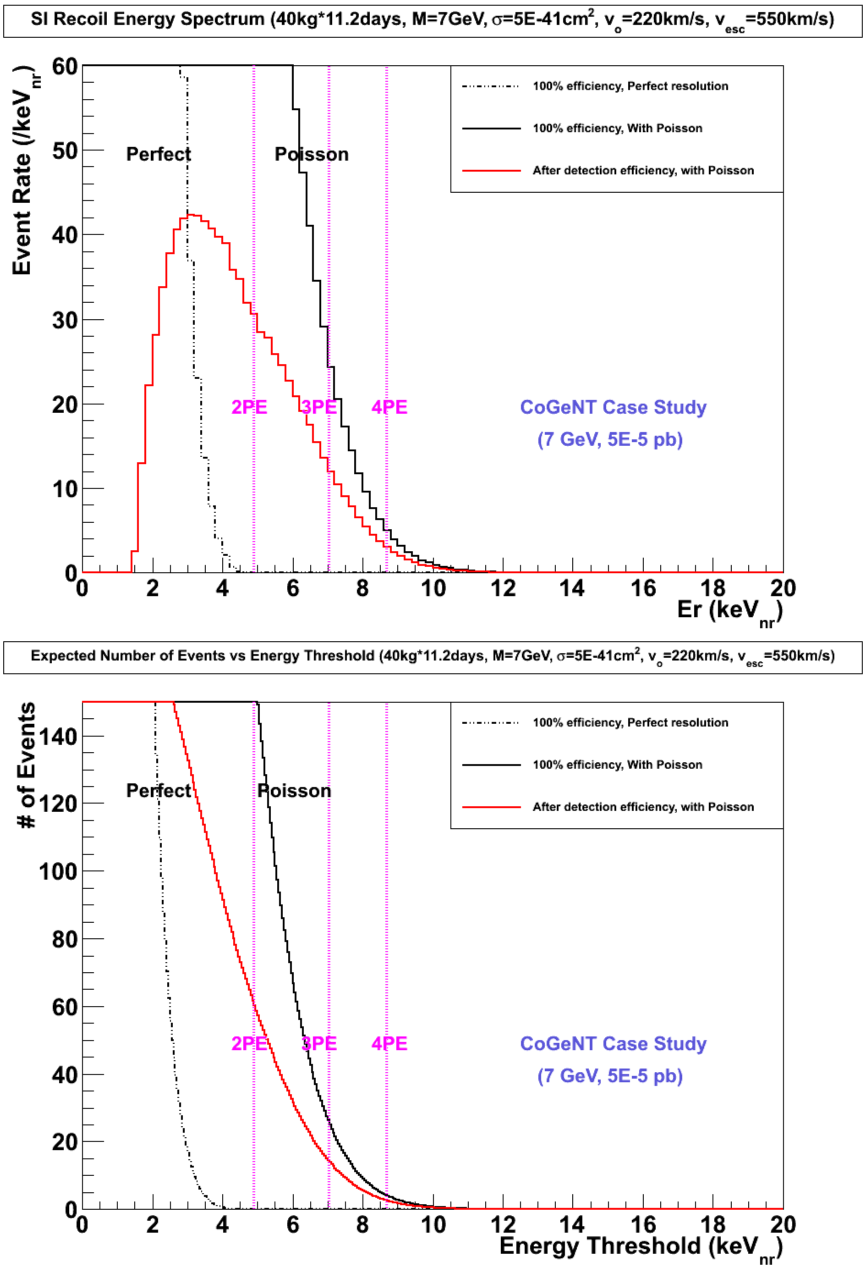

Figure 3.9: Top: WIMP Energy spectrum for perfect energy resolution (dashed black), finite energy resolution (solid black), finite energy resolution with efficiency (red) at 7 GeV WIMP mass and 5×10^{-5} pb cross section, using the best global fit to $\mathcal{L}_{\mathrm{eff}}$. Bottom: Number of WIMP events as a function of energy threshold for the 40 kg × 11.17 days data.

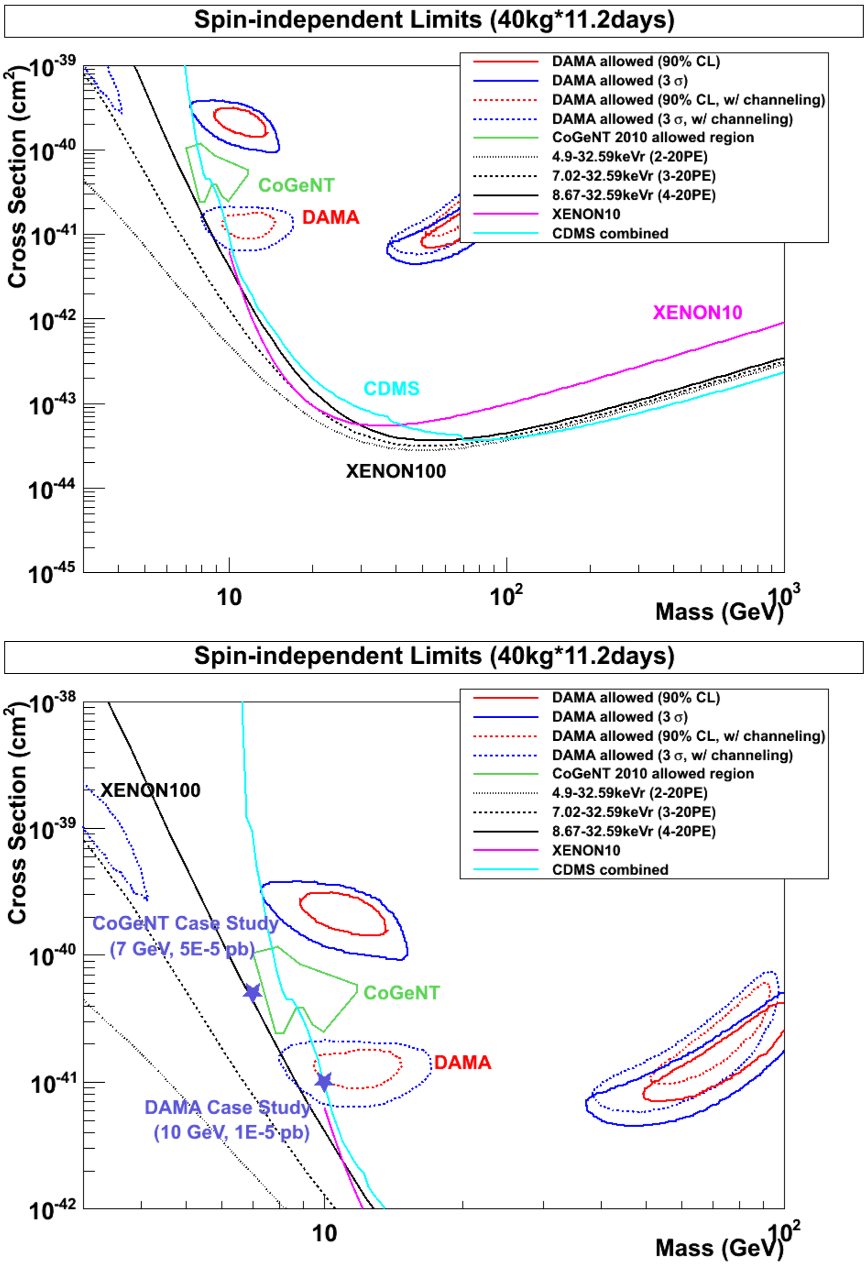

Figure 3.10: Top: 90% CL upper limit of cross section for the 40 kg × 11.17 days data with energy threshold of 4PE (solid), 3PE (dotted), and 2PE (dashed) using best global fit to $\mathcal{L}_{\rm eff}$. Bottom: Limit near the DAMA and CoGeNT allowed region.

final (red) spectrum. Fig. 3.8 and 3.9 (bottom) show the total expected number of WIMP events as a function of energy threshold. At 4PE threshold, the number of events is 5.5 and 2.7 for the DAMA and the CoGeNT case, both of which are > 2.3 and so are above the 90% CL upper limit of the 11.17 days data. Hence in the case of the best global fit, a threshold of 4PE is enough to exclude both the DAMA and the CoGeNT regions completely, as confirmed in Fig. 3.10 (bottom).

3.3.5.5 Manzur *et al.* (Yale) fit

The study is repeated using a fit to the Yale measurements of $\mathcal{L}_{\text{eff}}$. Compared to the best global fit, the Leff values are lower, and so the energy becomes higher given the same number of PE, which in general gives a more conservative result. The energy spectrum with and without detector effects are shown again in (Fig. 3.11 and 3.12, top, red). At 4PE threshold, the expected number of events is 2.6 and 1.1 for DAMA and CoGeNT respectively (Fig. 3.11 and 3.12, bottom, red), and so only DAMA (> 2.3) is excluded by the 90% CL upper limit but not CoGeNT (< 2.3). At 3PE threshold, the number of events is 10.0 (DAMA) and 7.5 (CoGeNT) and so both are ruled out by the 11.17 days data. As shown in Fig. 3.13 (bottom), the limit curve for 4PE threshold (solid black) can only exclude DAMA fully but not CoGeNT. If the threshold is lowered to 3PE (dashed black), both DAMA and CoGeNT can be completely excluded.

3.3.5.6 Most conservative fit

Lastly, the most conservative case is considered, using the lower 90% confidence contour of the $\mathcal{L}_{\text{eff}}$ global fit. The energy spectrum for the DAMA and the CoGeNT cases is plotted in Fig. 3.8 and 3.9 (top, red). The kinks of the spectrum are due to the $\mathcal{L}_{\text{eff}}$ function where the spline fit and the logarithmic extrapolation

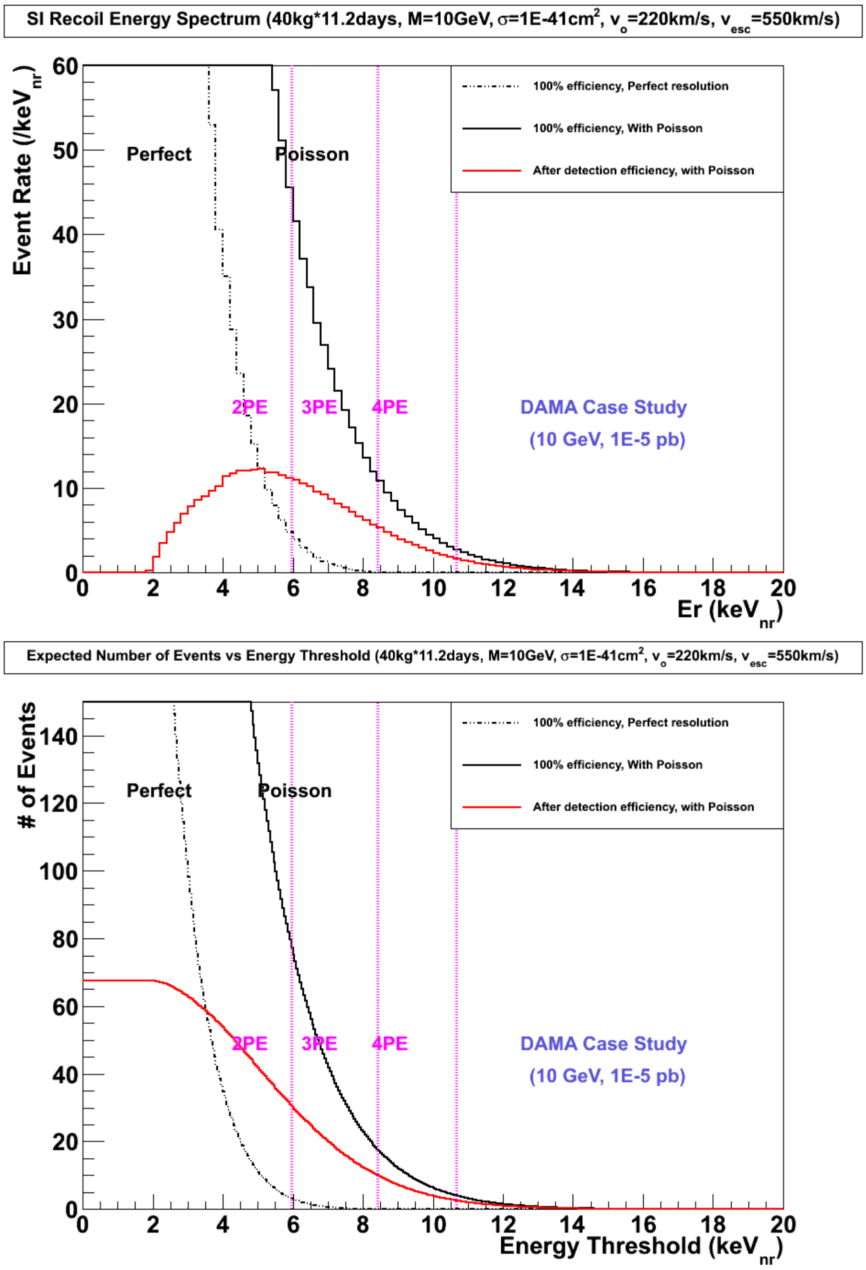

Figure 3.11: Top: WIMP Energy spectrum for perfect energy resolution (dashed black), finite energy resolution (solid black), finite energy resolution with efficiency (red) at 10 GeV WIMP mass and 10^{-5} pb cross section, using the fit to $\mathcal{L}_{\rm eff}$ from Yale data. Bottom: Number of WIMP events as a function of energy threshold for the 40 kg × 11.17 days data.

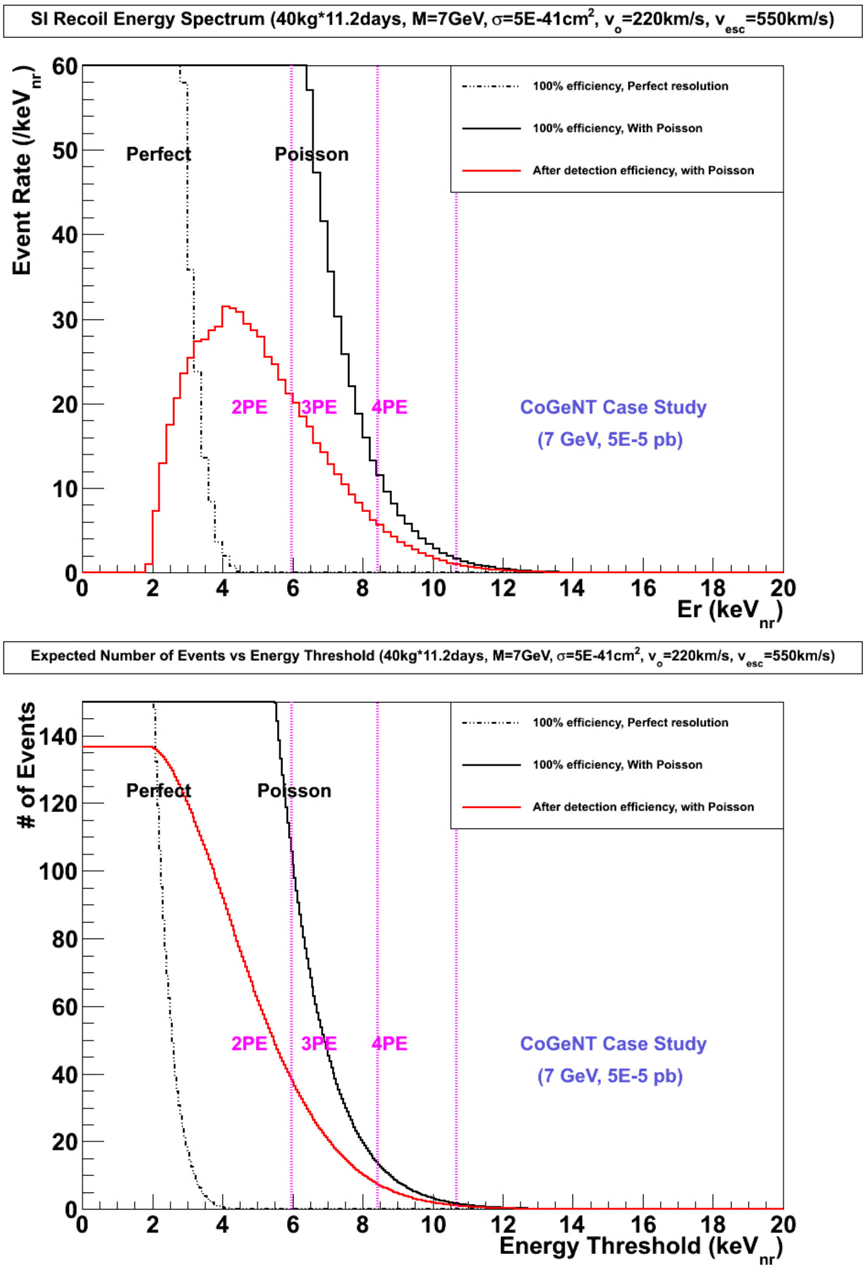

Figure 3.12: Top: WIMP Energy spectrum for perfect energy resolution (dashed black), finite energy resolution (solid black), finite energy resolution with efficiency (red) at 7 GeV WIMP mass and 5×10^{-5} pb cross section, using the fit to $\mathcal{L}_{\text{eff}}$ from Yale data. Bottom: Number of WIMP events as a function of energy threshold for the 40 kg × 11.17 days data.

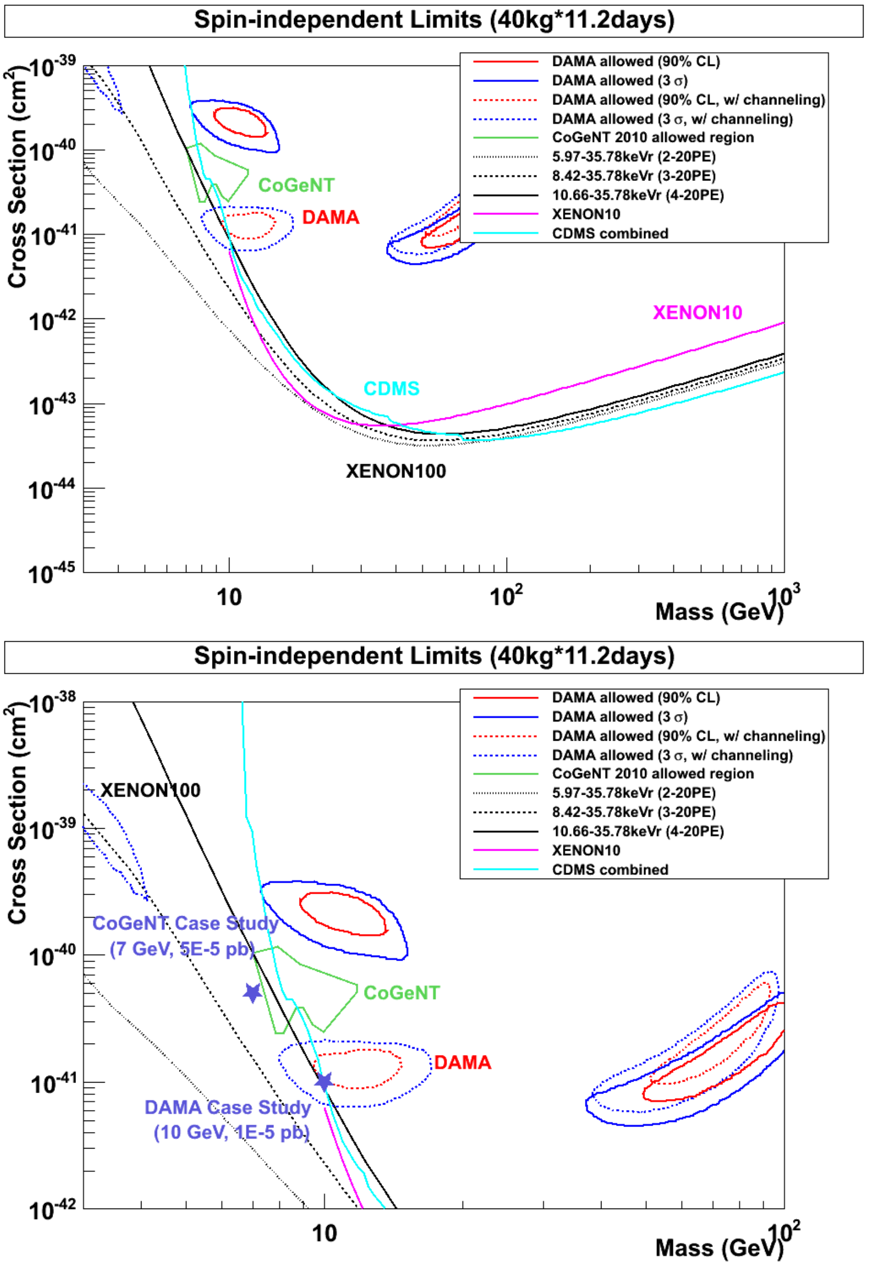

Figure 3.13: Top: 90% CL upper limit of cross section for the 40 kg × 11.17 days data with energy threshold of 4PE (solid), 3PE (dotted), and 2PE (dashed) using fit to $\mathcal{L}_{\rm eff}$ from Yale data. Bottom: Limit near the DAMA and CoGeNT allowed region.

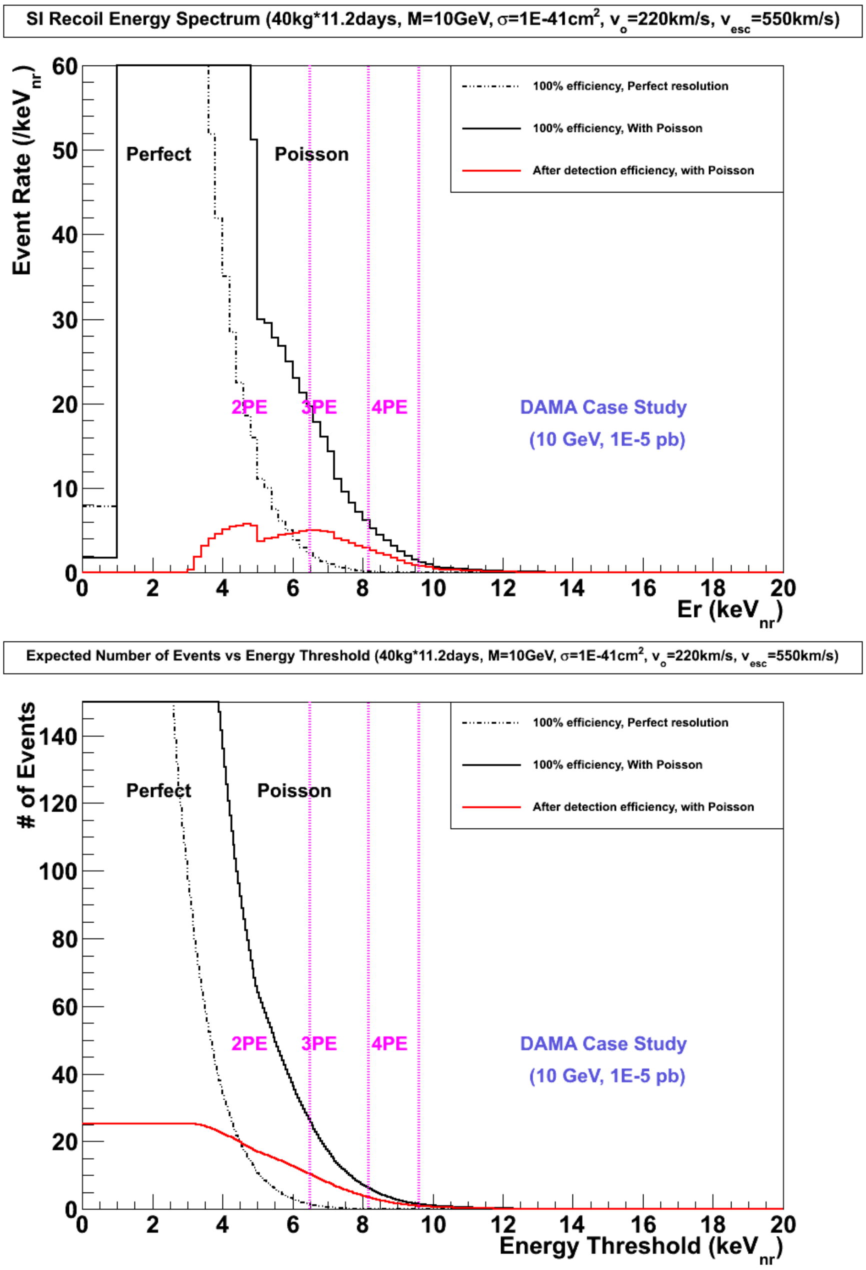

Figure 3.14: Top: WIMP Energy spectrum for perfect energy resolution (dashed black), finite energy resolution (solid black), finite energy resolution with efficiency (red) at 10 GeV WIMP mass and 10^{-5} pb cross section, using the lower 90% confidence contour of the global fit to $\mathcal{L}_{\text{eff}}$. Bottom: Number of WIMP events as a function of energy threshold for the 40 kg × 11.17 days data.

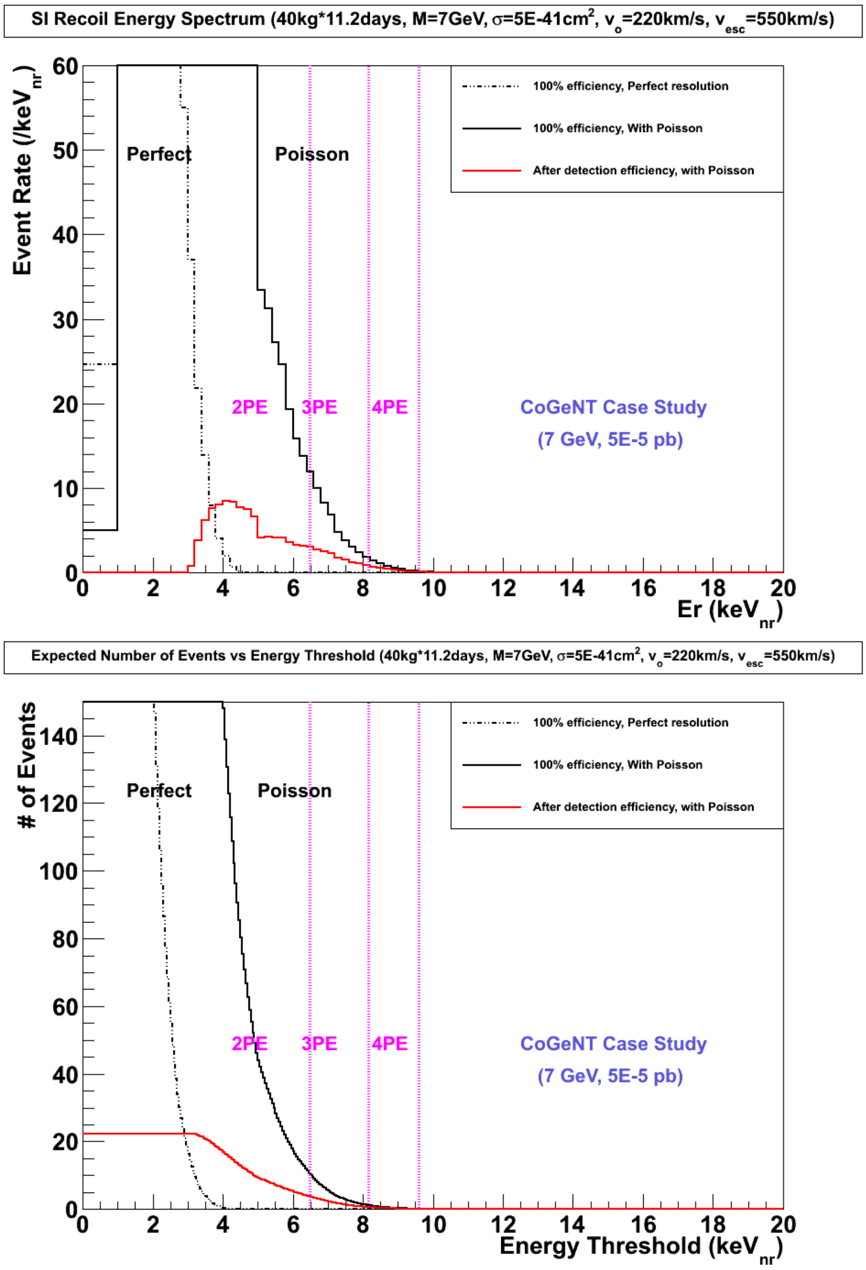

Figure 3.15: Top: WIMP Energy spectrum for perfect energy resolution (dashed black), finite energy resolution (solid black), finite energy resolution with efficiency (red) at 7 GeV WIMP mass and 5×10^{-5} pb cross section, using the lower 90% confidence contour of the global fit to $\mathcal{L}_{\text{eff}}$. Bottom: Number of WIMP events as a function of energy threshold for the 40 kg × 11.17 days data.

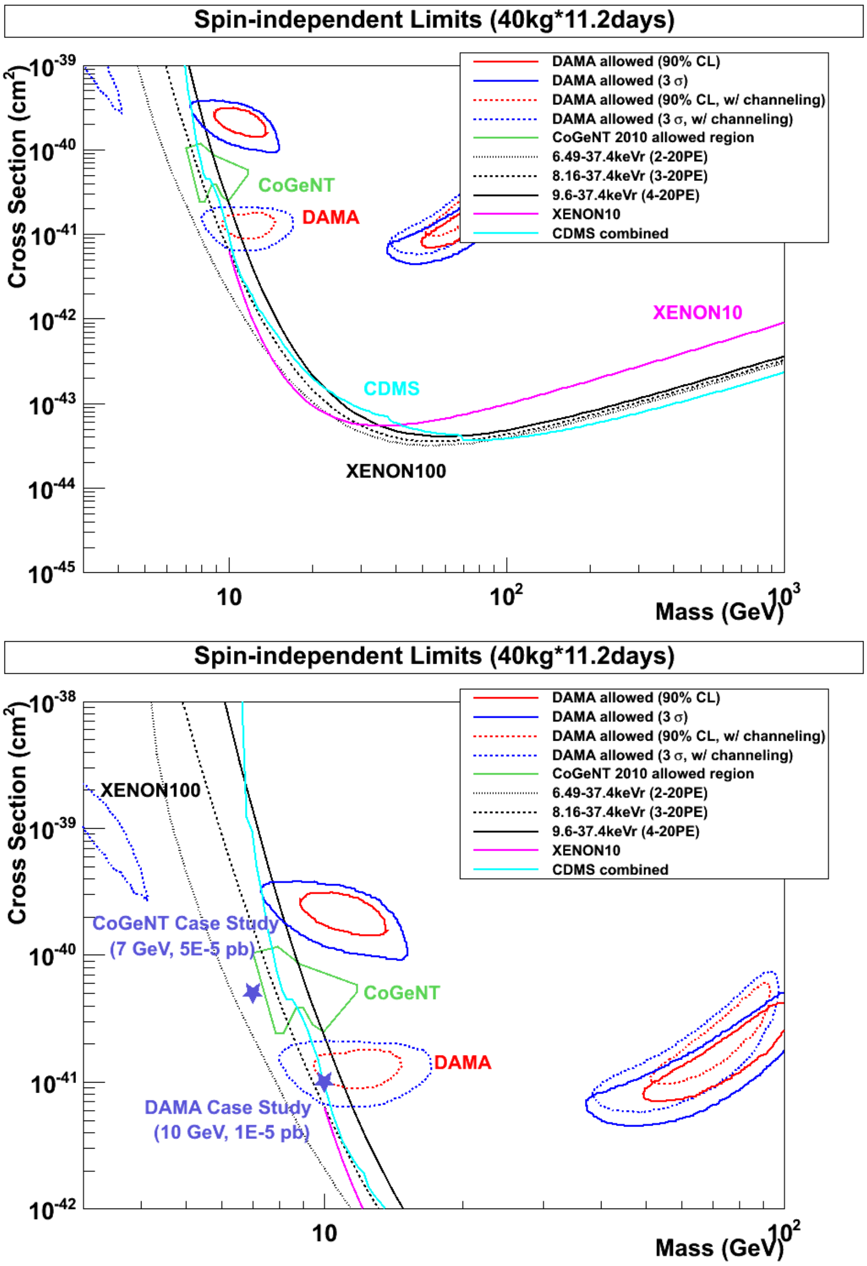

Figure 3.16: Top: 90% CL upper limit of cross section for the 40 kg × 11.17 days data with energy threshold of 4PE (solid), 3PE (dotted), and 2PE (dashed) using lower 90% confidence contour of global fit to $\mathcal{L}_{\mathrm{eff}}$. Bottom: Limit near the DAMA and CoGeNT allowed region.

are joined together non-smoothly at 5 keVr. Fig. 3.8 and 3.9 (bottom, red) show the total number of WIMP events as a function of energy threshold. At 4PE threshold, the expected number of events is 1.0 and 0.09 for DAMA and CoGeNT respectively, and so neither DAMA nor CoGeNT can be excluded. At 3PE threshold, the expected number of events is 3.5 (DAMA) and 0.6 (CoGeNT), and so only DAMA (> 2.3) is excluded by the 90% CL upper limit but not CoGeNT (< 2.3). At 2PE threshold, the number of events is 10.5 (DAMA) and 3.8 (CoGeNT) and so both are ruled out by the 40 kg × 11.17 days data. The results above are confirmed by Fig. 3.16 (bottom), in which the limit curve for 4PE threshold (solid black) cannot exclude either DAMA or CoGeNT. The limit curve for 3PE threshold (dashed black) can exclude DAMA but not CoGeNT. If the threshold is lowered to 2PE (dotted black), both DAMA and CoGeNT can be completely excluded.

3.3.5.7 Summary

Table 3.1 summarizes the energy thresholds and the number of expected WIMP events in all three cases of $\mathcal{L}_{\rm eff}$ fit. The final results of the cross section limits of the 40 kg × 11.17 days data between $5 - 1000$ GeV WIMP mass are shown in Fig. 3.17 (top). The minimum of the limit is at a cross section of 3.4×10^{-44} cm^2 for a WIMP mass of 55 GeV. Due to a much greater fiducial mass and a high background rejection power, this limit, based only on 11.17 days of exposure, shows the capability of the XENON100 detector, as it has achieved limits comparable to the previous XENON10 and the current CDMS experiments, both of which have much longer live time. It also demonstrates that, with increased live time for which the detector is currently being run, a much better limit with order of magnitude improvements over other experiments will be reached. In terms of

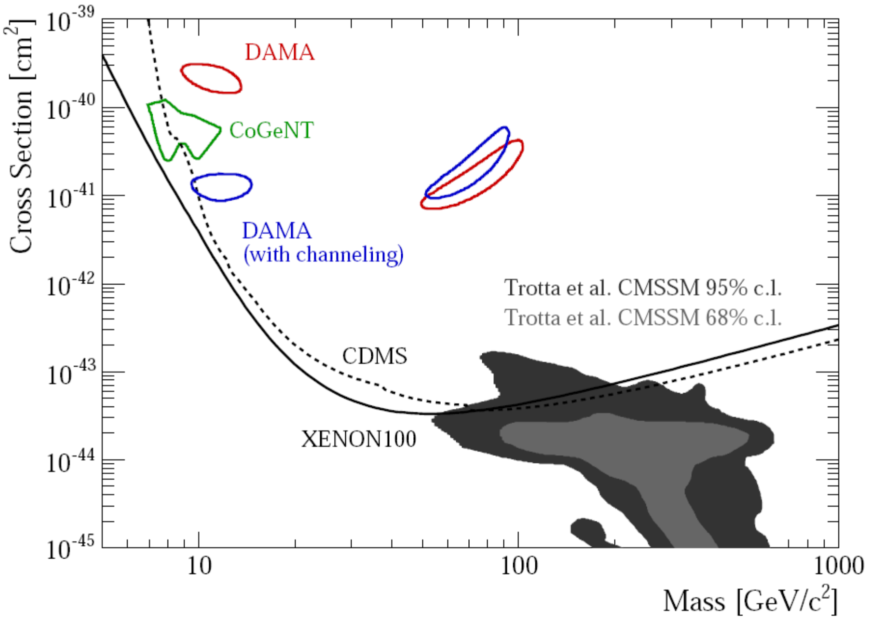

Figure 3.17: Final cross section upper limit for the 40 kg × 11.17 days data. The XENON100 and CDMS [3] limits are shown as solid and dashed black lines. CoGeNT [5] and DAMA [16] (with and without channeling) allowed regions are shown as green, blue, and red contours. Grey areas show the expectations from a theoretical model [34]. Figure taken from [23].

	Global fit			Yale fit			Lower 90% CL		
Threshold (PE)	4PE	3PE	2PE	4PE	3PE	2PE	4PE	3PE	2PE
Threshold (keVr)	8.67	7.02	4.90	10.66	8.42	5.97	9.60	8.16	6.49
# events (DAMA case)	5.5	17.8	46.1	2.6	10.0	30.5	1.0	3.5	10.5
# events (CoGeNT case)	2.7	14.5	60.2	1.1	7.5	38.4	0.09	0.6	3.8

Table 3.1: Expected number of WIMP events in the DAMA and the CoGeNT case study for all three $\mathcal{L}_{\text{eff}}$ fits

ruling out low mass WIMPs as an explanation for the DAMA and CoGeNT signal, additional improvements are still needed in order for a convincing statement to be made. As shown above, the resulting limit is highly dependent on the choice of $\mathcal{L}_{\text{eff}}$ fits. Because of the high experimental uncertainty of $\mathcal{L}_{\text{eff}}$ and the absence of its measurements at low energy, one could not estimate the limit at low WIMP masses with high accuracy due to the steepness of the energy spectrum. Because of the high mass of the xenon nucleus, the sensitivity of the XENON detector is limited at low WIMP masses by nature. With (1) more accurate measurements of $\mathcal{L}_{\text{eff}}$ at lower energy, (2) lower energy threshold, and (3) increased exposure in future detectors, it will become possible for a better conclusion to be drawn.

3.3.6 Inelastic Dark Matter (iDM) Analysis

3.3.6.1 Introduction

In addition to low mass WIMPs, other models have been proposed [35] to reconcile the discrepancy between the DAMA [15] experiment and the other experiments with null results. The theory of inelastic dark matter [36] was first motivated by the upturn of the positron fraction in the PAMELA [37] experiment and the electron+positron excess in the ATIC [38] experiment. However, it was found to be possible to attribute the modulated signal in DAMA to an inelastic dark matter signal. The theory of inelastic dark matter requires that, in addition to the dark matter particle χ, there exists an excited state χ^* with a higher mass [39] (Eq. 3.12). The difference in mass of the two states is referred to as the mass splitting δ.

$$m_{\chi^*} = m_\chi + \delta \tag{3.12}$$

A dark matter particle, after scattering inelastically off of an atomic nucleus, will turn into the excited state, such that some of the kinetic energy is converted to the mass of the dark matter particle (Eq. 3.13).

$$\chi N \to \chi^* N \tag{3.13}$$

The iDM theory has the properties of having an enhanced modulation amplitude, and a drastically different shape of the energy spectrum that decreases to zero at low energy. Both of these are helpful in reconciling DAMA and the other experiments.

Below I will first describe the recoil energy spectrum for scattering of inelastic dark matter. Then a data analysis will be performed on the same 11.17 days dataset, except that the upper bound of the energy window is extended to 100 keVr (see Sec. 3.3.6.4). The upper limit of cross section will be computed in the parameter space of mass splitting δ and WIMP mass M_χ. The results will then be compared with the region in the parameter space allowed by the DAMA results, and conclusion will be drawn on whether the 11.17 days data can rule out inelastic dark matter (with 90% CL) as an explanation for the signals found in the DAMA experiment.

3.3.6.2 Energy Spectrum

The iDM differential event rate per unit detector mass for a recoil energy E_R is [39]

$$\frac{dR}{dE_R} = A^2 \frac{\rho_\chi \sigma_{\chi-p}}{2M_\chi \mu_{ne}^2} F^2 \int_{v_{min}}^{\infty} \frac{1}{v} f(\vec{v}) d^3\vec{v} \tag{3.14}$$

where M_χ is the WIMP mass, $\sigma_{\chi-p}$ is the WIMP-nucleon cross section, and μ_{ne} is the WIMP-nucleon reduced mass. $v_{min} = \sqrt{\frac{1}{2M_N E_R}}(\frac{M_N E_R}{\mu} + \delta)$ is the minimum velocity for a DM particle to scatter, which depends on the mass splitting $\delta = M_{\chi^*} - M_\chi$. M_N is the nucleus mass, and μ is the WIMP-nucleus reduced mass. Similar to spin-independent scattering, a Maxwellian velocity distribution $f(\vec{v}) \sim e^{-(\vec{v}+\vec{v}_E)^2/v_o^2}$ with a cutoff at escape velocity v_{esc} is used. Since the choice of the value of the escape velocity has a greater effect on the iDM energy spectrum than in the case of elastic scattering, I consider various escape velocity values: $v_{esc} = 490, 544, 650$ km/s, which is the range the galactic escape velocity is likely to lie within ([44] [45]). A WIMP characteristic velocity of $v_o = 220$ km/s and WIMP density of $\rho_\chi = 0.3$ GeV/c^2/cm^3 have been assumed. For the nuclear form factor F^2, the Helm form factor detailed in [17] is used.

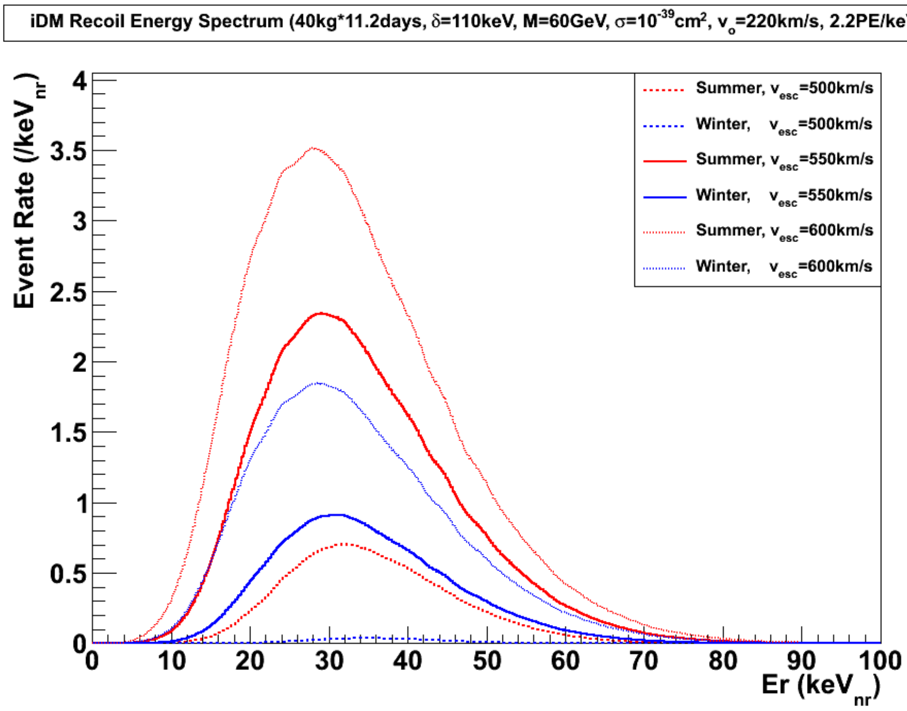

Figure 3.18: Recoil energy spectrum in summer (red) and winter (blue) for 40 kg × 11.17 days of exposure for $M_\chi = 60$ GeV and $\delta = 110$ keV (Escape velocity $v_{esc} = 500$ (dashed line), 550 (solid), 600 (dotted) km/s)

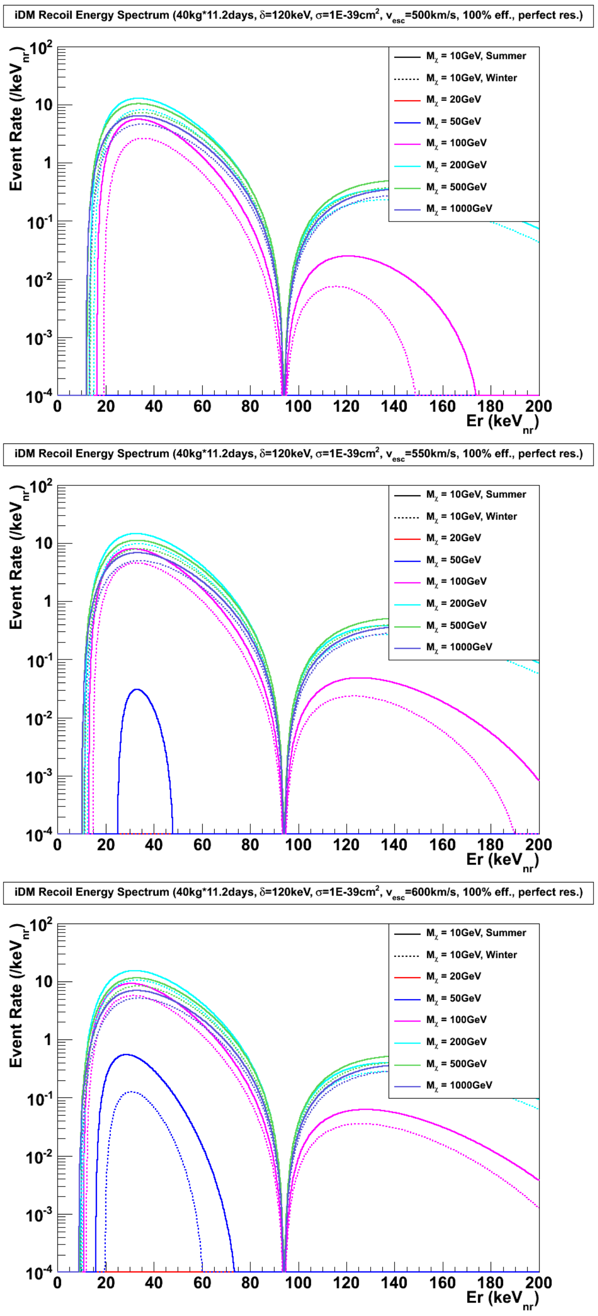

Figure 3.19: Recoil energy spectrum in summer (solid) and winter (dashed) for 40 kg × 11.17 days of exposure at $\delta = 120$ keV for $M_\chi = 10, 20, 50, 100, 200, 500, 1000$ GeV (Escape velocity $v_{esc} = 500$ (top), 550 (middle), 600 (bottom) km/s)

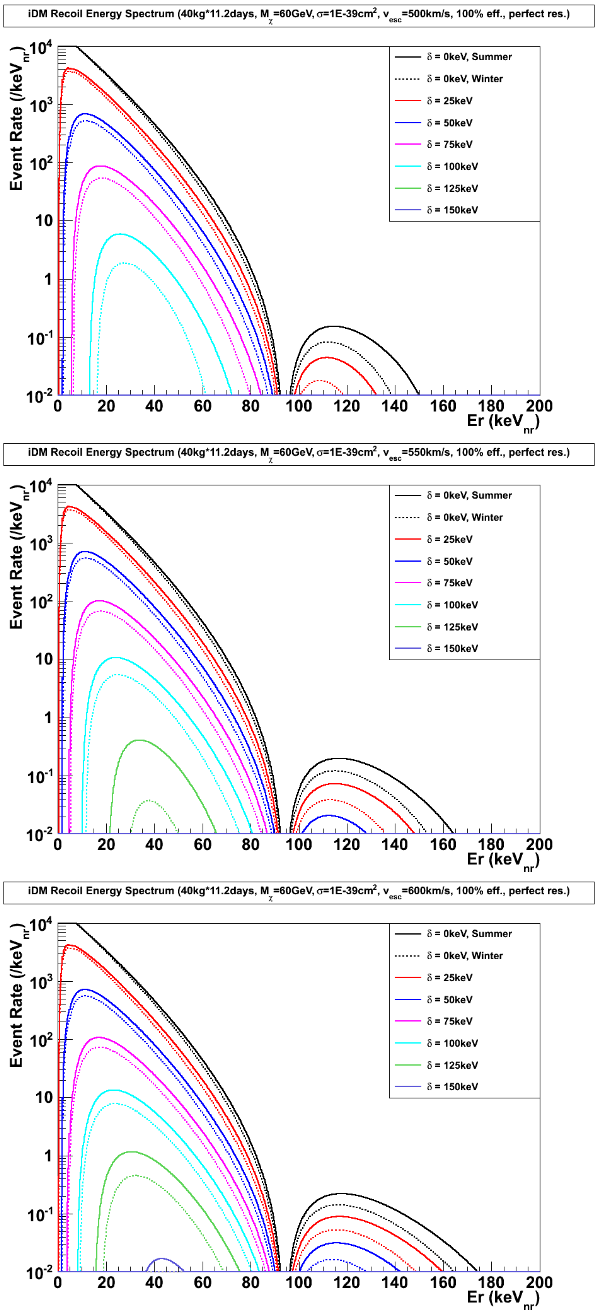

Figure 3.20: Recoil energy spectrum in summer (solid) and winter (dashed) for 40 kg × 11.17 days of exposure at $M_\chi = 60$ GeV for $\delta = 0, 25, 50, 75, 100, 125, 150$ keV (Escape velocity $v_{esc} = 500$ (top), 550 (middle), 600 (bottom) km/s)

3.3.6.3 Annual Modulation

The annual modulation effect has also been considered and is introduced into the WIMP velocity distribution through the earth velocity $\vec{v}_E$, which is the velocity of the earth w.r.t. the dark matter halo, and is given by

$$\vec{v}_E = \vec{u}_r + \vec{u}_s + \vec{u}_E, \tag{3.15}$$

where

1. $\vec{u}_r = (0, v_o, 0)$ is the rotation velocity of the local standard of rest (L.S.R.).
2. $\vec{u}_s$ is the sun velocity w.r.t. the L.S.R. which is taken from [40].
3. $\vec{u}_E$ is the earth's orbital velocity around the sun taken from [17].

To account for annual modulation, I numerically average the recoil energy spectrum for varying values of $\vec{u}_E$ over the data-taking period. Fig. 3.18 gives an example of the effect of annual modulation on the energy spectrum for different DM escape velocities for WIMP mass $M_\chi = 60$ GeV and mass splitting $\delta = 110$ keV.

3.3.6.4 Data Analysis

Data Set The limits on inelastic dark matter is calculated based on a 11.17 days data set taken between Oct. and Nov. 2009 with a fiducial mass of 40 kg. The energy window is chosen to be $8.67 - 100$ keVr, which corresponds to an energy threshold of 4 photo-electrons. The choice of 100 keVr as the upper bound of the energy window is a compromise between obtaining more iDM events and limiting the number of background events. In most of the iDM parameter space, the recoil energy spectrum is peaked within the energy window and decreases to well below the peak value at 100 keVr. Also, the first zero of the form factor occurs at about 100 keVr as seen in Fig. 3.19 and 3.20. Therefore raising the upper bound of the energy window above 100 keVr would not improve the limit significantly but may lead to more observed events due to backgrounds. The same software cuts detailed in Sec. 3.3.1 have been applied to reject the background events.

3.3.6.5 Allowed regions and upper limits

Allowed regions The DAMA allowed region was obtained based on a goodness-of-fit test with 90%CL on the DAMA modulation amplitude data [15]. The DAMA modulation data is available between $2-20$ keV$_{\mathrm{ee}}$ in 0.5 keV$_{\mathrm{ee}}$ bins. The data is consistent with zero above ~ 10 keV$_{\mathrm{ee}}$, and there are various choices in the literature [41] in choosing the energy window when fitting the data, which may affect the results. Noting that the modulation amplitude is close to zero above ~ 10 keV$_{\mathrm{ee}}$, I adopt the choice of binning in [16] by combining the data between $10-20$ keV$_{\mathrm{ee}}$ into one single bin. The allowed region is then computed based on 17 bins (16 equally-sized bins between $2-10$ keV$_{\mathrm{ee}}$ and 1 bin between $10-20$ keV$_{\mathrm{ee}}$) with 17 d.o.f. ($\chi^2 = 24.77,\ 33.41$ for 90%, 99% CL). The effect of ion-channeling [42] is not included in the calculation as it will have negligible effect on the allowed region based on newly computed channeling fraction in recent paper [43]. The allowed regions are obtained in the parameter space of M_χ, δ, and $\sigma_{\chi-p}$. Slices of the regions for various constant values of δ and M_χ are plotted in Fig. 3.21 ($\delta = 20,\ 40,\ 60,\ 80,\ 100,\ 120,\ 140,\ 155$ keV) and Fig. 3.22, 3.23 ($M_\chi = 10,\ 20,\ 40,\ 60,\ 80,\ 100,\ 150,\ 200$ GeV) respectively for $v_{esc} = 544$ km/s.

Upper limits The 90%CL upper limit of $\sigma_{\chi-p}$ is based on 40 kg × 11.17 days of exposure with 0 observed events in the $8.67-100$ keVr energy window. Similar to the Spin-independent limit calculation, it is a 1-sided limit (the expected number of DM events is 2.303 at the 90% CL upper limit). The limit does not have background subtraction. Since the 11.17 days data set was taken between Oct20 $-$ Nov12, the annual modulation effect in the recoil energy spectrum needs to be included, which gives a lower event rate during winter than summer. I also take into account the finite energy resolution by using a simple assumption of smearing based on photo-electron statistics and convolute the energy spectrum with a Poisson distribution. The best global fit in Sec. 3.3.2.1 is used when converting the energy between keVr and photo-electrons. After smearing the recoil energy spectrum, it is multiplied by the nuclear recoil acceptance and the energy dependent detector efficiency in Fig. 3.4, and I integrate the spectrum between 8.67 $-$ 100 keVr to find the expected number of events for any given $\sigma_{\chi-p}$. The resulting limits for 11.17 days of exposure are shown in Fig. 3.21, 3.22, and 3.23.

For comparison I also computed the upper limit based on an exposure of 137 days for part of a run during the first half of 2010. The data have not been unblinded, and it is unknown how many events will be found. I consider a pessimistic scenario where 30 events are observed, which is well above the expected background of $\sim$ 20 events [24]. The 90% CL upper limit is computed using Poisson method without background subtraction. Given the cross section at the upper limit, the probability of observing more than 30 events in an experiment is 90%, and since the observed number of events follows a Poisson distribution, the expected number of events at the upper limit is 38.3 (Eq. 3.16). The limit for this exposure benefits from the annual modulation effect as it includes live time in summer.

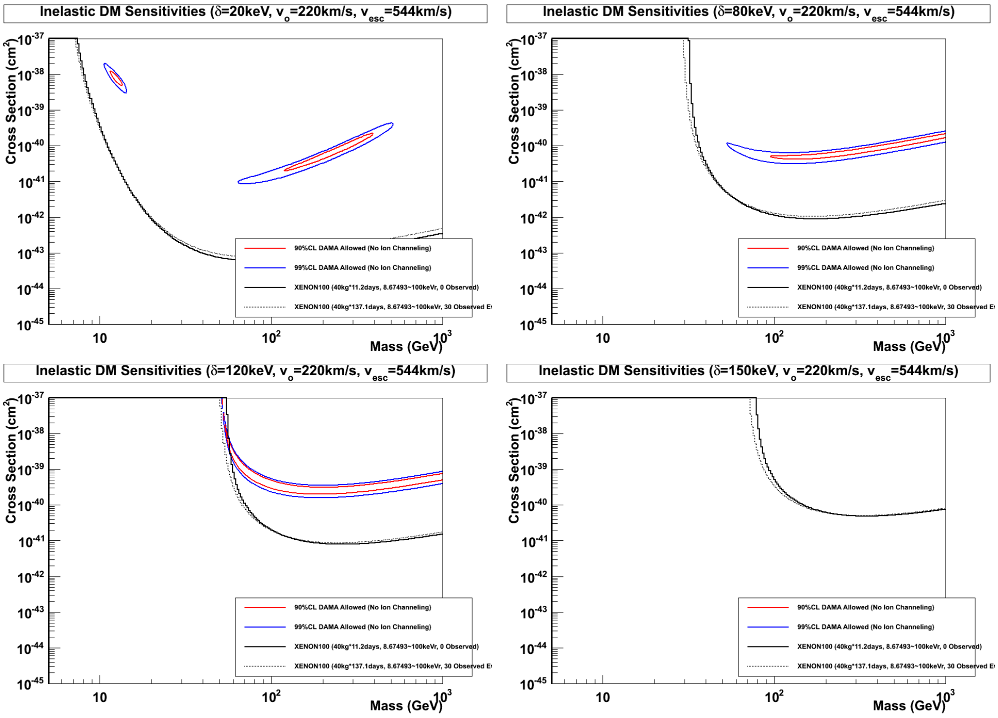

Figure 3.21: Allowed regions of DAMA with 90%CL (red), 99%CL (blue) and $\sigma_{\chi-p}$ upper limits of 11.17 days (solid black) and 137 days (dotted black) exposure versus DM mass M_χ for different values of mass splitting $\delta = 20,\ 80,\ 120,\ 150$ keV. (Escape velocity of 544 km/s has been assumed).

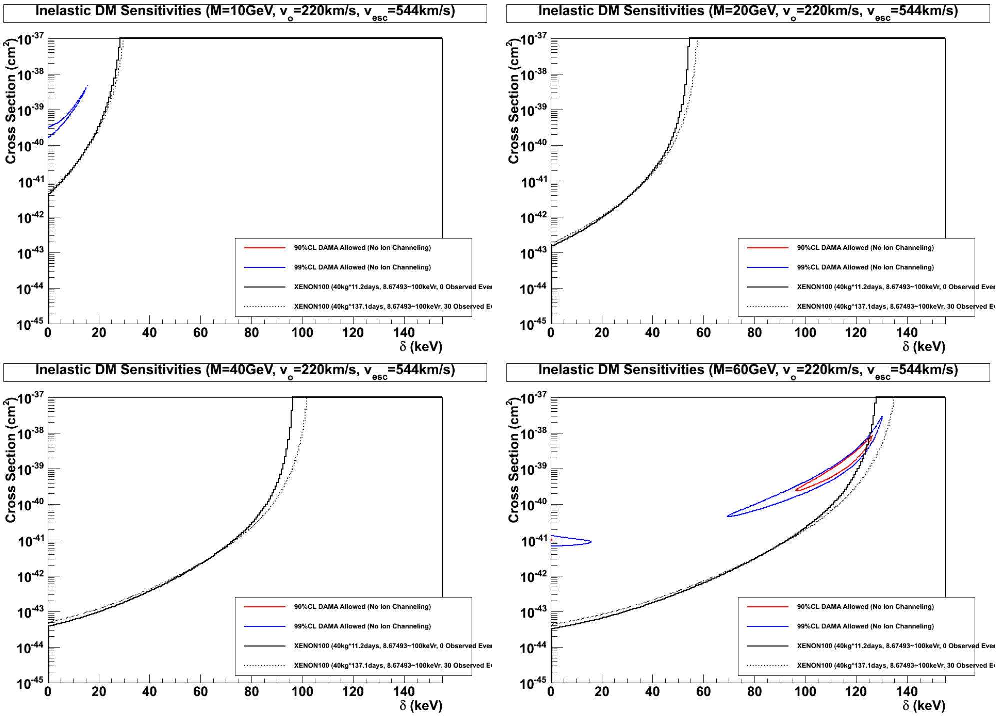

Figure 3.22: Allowed regions of DAMA with 90%CL (red), 99%CL (blue) and $\sigma_{\chi-p}$ upper limits of 11.17 days (solid black) and 137 days (dotted black) exposure versus mass splitting δ for different values of DM mass $M_\chi = 10,\ 20,\ 40,\ 60$ GeV. (Escape velocity of 544 km/s has been assumed)

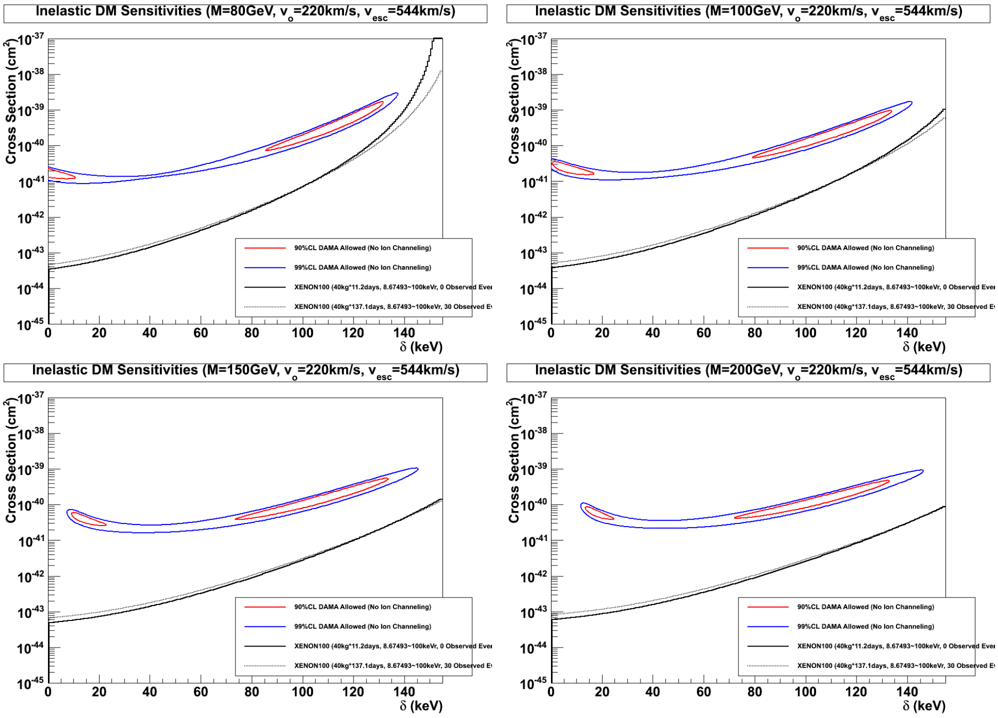

Figure 3.23: Allowed regions of DAMA with 90%CL (red), 99%CL (blue) and $\sigma_{\chi-p}$ upper limits of 11.17 days (solid black) and 137 days (dotted black) exposure versus mass splitting δ for different values of DM mass $M_\chi = 80,\ 100,\ 150,\ 200$ GeV. (Escape velocity of 544 km/s has been assumed)

$$\sum_{k>31} \frac{\lambda^k e^{-\lambda}}{k!} = 0.9 \;\rightarrow\; \lambda \simeq 38.3 \tag{3.16}$$

Finally, Fig. 3.24 shows, in the parameter space of WIMP mass M_χ and mass splitting δ, allowed regions of DAMA that are completely ruled out for all values of $\sigma_{\chi-p}$ by the 11.17 days and 137 days exposure. The grey region represents values of WIMP mass and mass splitting for which there exist a cross section allowed by the DAMA results at 90%CL. The pink and blue contours show areas in which the DAMA-allowed regions are excluded at 90%CL by the 11.17 days and 137 days exposure. The results are plotted for $v_{esc} = 490,\ 544,\ 650$ km/s. The 11.17 days data set almost completely excludes DAMA, except for small region near $M_\chi \sim 60$ GeV, $\delta \sim 120$ keV. This can be partly attributed to the annual modulation effect, since the WIMP event rate in winter can be lower than in summer by a factor of ~ 2 or more as shown in Fig. 3.18, depending on the value of δ. The 137 days exposure, even with 30 observed events, will exclude all of the allowed regions for escape velocities between $490-650$ km/s. The excluded regions for XENON10 and CDMS [3] are shown in Fig. 3.25 for comparison.

3.3.6.6 Summary

Using the above method, the 40 kg × 11.17 days data set can almost, but not fully, reject all DAMA regions with 90%CL as seen in Fig. 3.24. This is mainly because of annual modulation as the WIMP event rate in winter is much lower, and also because of insufficient exposure. However, the limits achieved by the 11.17 days data show much better improvement compared to current limits from previous experiments. It excludes substantial regions that have not been excluded by previous experiments such as XENON10 and CDMS (Fig. 3.25), and there are only very small regions that still remain compatible. Also, increased exposure

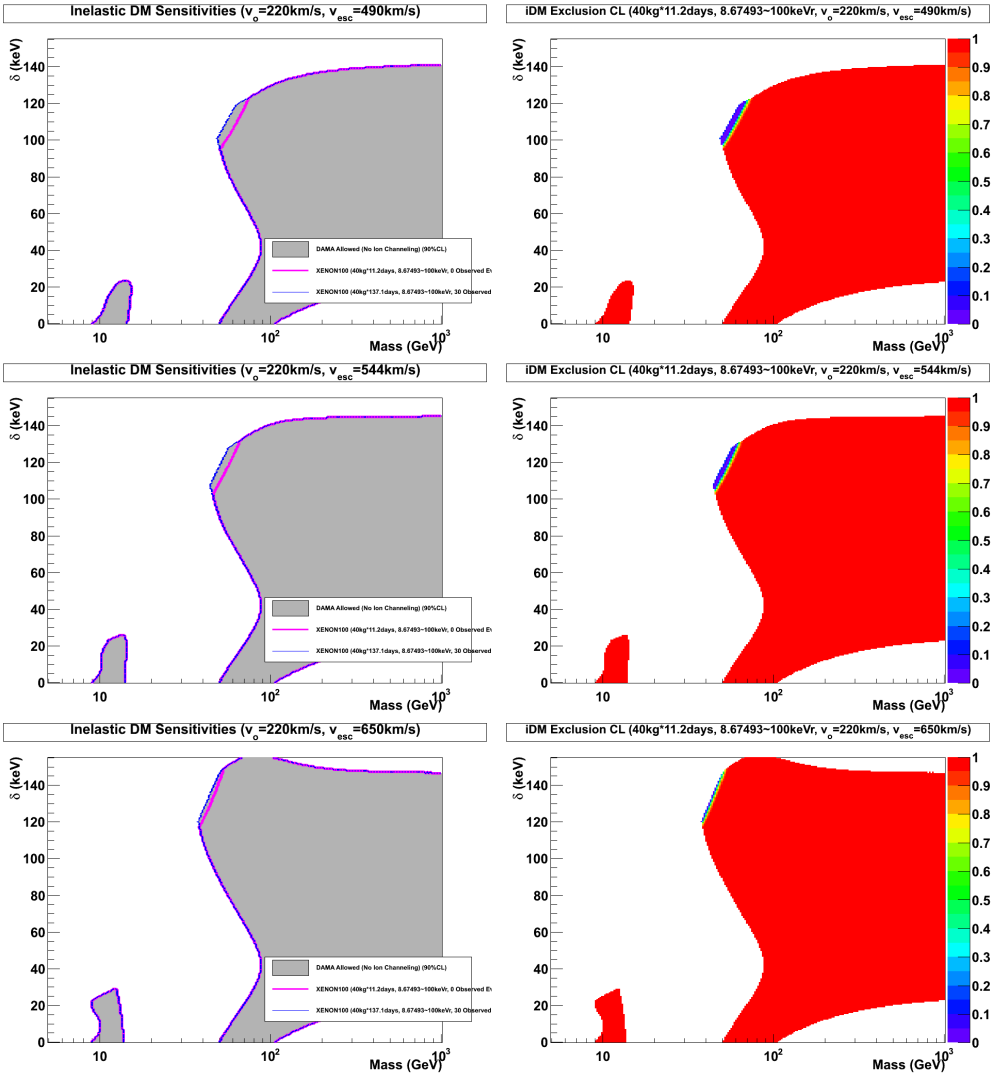

Figure 3.24: (Left) Regions in the parameter space of M_χ and δ allowed by DAMA with 90%CL (grey). Colored contours show regions excluded by the 11.17 days (pink) and 137 days (blue) exposure ($v_{esc} = 490$ (top), 544 (middle), 650 (bottom) km/s). (Right) Confidence level with which the 90% CL DAMA region is excluded by the 11.17 days data.

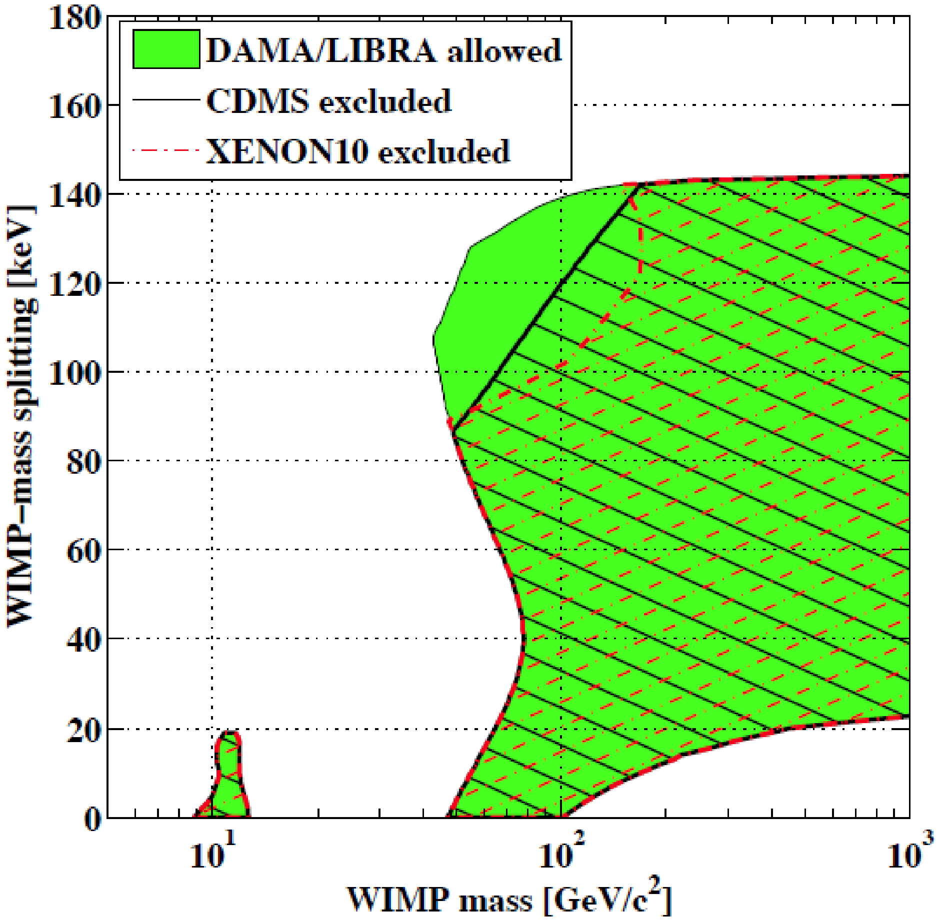

Figure 3.25: Regions in the parameter space of M_χ and δ allowed by DAMA with 90%CL (green). Also shown are regions excluded by CDMS II (black) and XENON10 (red) [46]. Figure taken from [3].

that contains summer data will be able to reject DAMA results.

CHAPTER 4

Background Simulations of Future Detectors

4.1 Introduction

Given the success of the XENON100 detector, the possibility of improving the sensitivity in the future with larger detectors, using not only liquid xenon but also liquid argon as the target material, is considered here. The ideas and advantages of using two different types of targets for direct detection are discussed in detail in [47]. By combining Xe and Ar in future large detectors, one will not only be able to achieve better sensitivity, but will also allow for verification of the A^2 dependence of spin-independent scattering, as well as measurements of WIMP parameters such as WIMP mass, WIMP velocity, and WIMP-nucleon cross section. In this chapter I look into an important aspect that needs to be studied for future detectors, that is, background estimation. The radioactive background will be estimated for four different future detectors: Xenon1T, Argon5T, Xenon10T, Argon50T. As implied by their names, The fiducial masses of these detectors are approximately 1 ton Xenon, 5 ton Argon, 10 ton Xenon, and 50 ton Argon. The geometries used in the estimation are based on past designs by the UCLA dark matter group [48]. Although they may be different from the actual geometries which are to be finalized in the future, they provide approximate estimation of the background level, which will serve as useful information for the design of these detectors. Lastly, the sensitivity of the future detectors will also be studied, including the cross section upper limits (in the case of zero or very few observed events) and measurements of WIMP parameters (in the case of many observed events).

4.2 Detector Designs

Each detector is contained in a Teflon cylinder inside a cylindrical double-walled titanium cryostat, with two arrays of Quartz Photon-Intensifying Detectors (QUPIDs) [47] at the top and the bottom of the detector for collection of scintillation light. The cryostat is contained in a tank of liquid scintillator [49] doped with 0.5% Gd (for high absorption of thermal neutrons) and equipped with PMTs, which is used as an active veto for rejecting neutron background events. The liquid scintillator veto is further surrounded by a water tank (also equipped with PMTs), which is used as a muon veto. Fig. 4.2 shows the detailed dimensions and masses of each detector component in the Xenon1T detector. Argon5T, Xenon10T, and Argon50T share a similar geometry but with larger detector sizes.

4.3 Background Estimation Method

The estimation of the background level in these future detectors are done by a detailed Monte Carlo simulation using the GEANT4 code [50] [51] and analyzed using ROOT [52] program. The detailed geometry is put into the code for accurate results. Fig. 4.1 and Fig. 4.2 show parts of the geometry for Xenon1T as put into the GEANT4 code. Radioactive contaminants including ^{238}U, ^{232}Th, ^{40}K, and ^{60}Co in each detector components are simulated for both the gamma and the neutron background. Simulations were run with UCLA dark matter group's

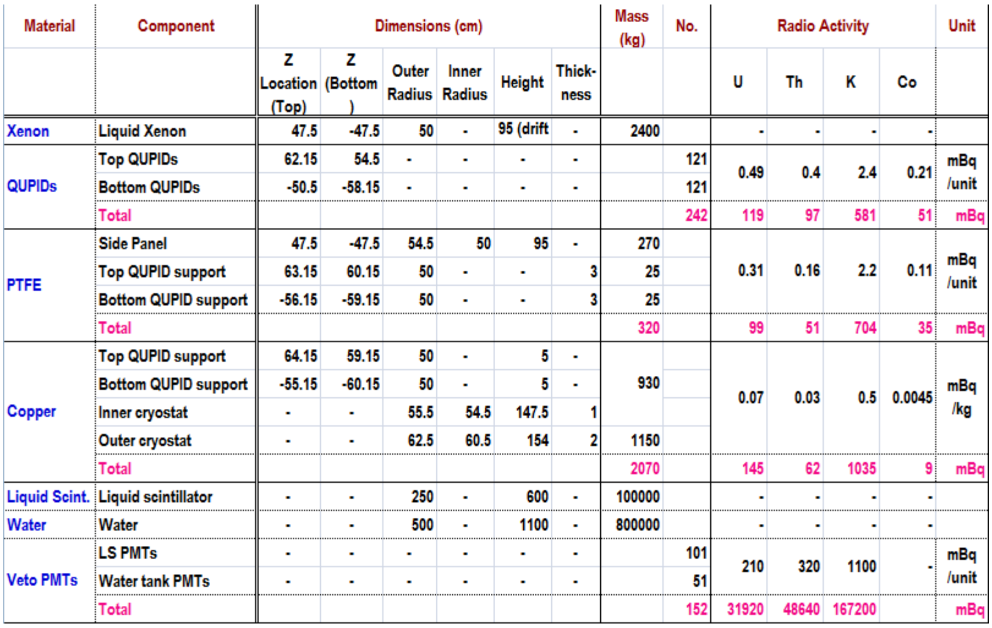

Material	Component	Dimensions (cm)						Mass (kg)	No.	Radio Activity				Unit
		Z Location (Top)	Z (Bottom)	Outer Radius	Inner Radius	Height	Thick-ness			U	Th	K	Co	
Xenon	Liquid Xenon	47.5	-47.5	50	-	95 (drift	-	2400		-	-	-	-	
QUPIDs	Top QUPIDs	62.15	54.5	-	-	-	-		121	0.49	0.4	2.4	0.21	mBq /unit
	Bottom QUPIDs	-50.5	-58.15	-	-	-	-		121					
	Total								242	119	97	581	51	mBq
PTFE	Side Panel	47.5	-47.5	54.5	50	95	-	270		0.31	0.16	2.2	0.11	mBq /unit
	Top QUPID support	63.15	60.15	50	-	-	3	25						
	Bottom QUPID support	-56.15	-59.15	50	-	-	3	25						
	Total							320		99	51	704	35	mBq
Copper	Top QUPID support	64.15	59.15	50	-	5	-	930		0.07	0.03	0.5	0.0045	mBq /kg
	Bottom QUPID support	-55.15	-60.15	50	-	5	-							
	Inner cryostat	-	-	55.5	54.5	147.5	1							
	Outer cryostat	-	-	62.5	60.5	154	2	1150						
	Total							2070		145	62	1035	9	mBq
Liquid Scint.	Liquid scintillator	-	-	250	-	600	-	100000		-	-	-	-	
Water	Water	-	-	500	-	1100	-	800000		-	-	-	-	
Veto PMTs	LS PMTs	-	-	-	-	-	-		101	210	320	1100	-	mBq /unit
	Water tank PMTs	-	-	-	-	-	-		51					
	Total								152	31920	48640	167200		mBq

Table 4.1: The location and size of each detector component in the Xenon1T detector.

computer cluster which consists of $\sim$ 30 machines.

4.4 Background Rejection Techniques

After the background events have been simulated, various software cuts are applied to the data. These cuts are designed to discriminate the backgrounds from the WIMP signals, and ideally they would reject all of the background events and none of the signal events. In reality this is not achievable, as some of the backgrounds will survive the cuts, resulting in a contamination of background events in the data; likewise a fraction of the signal events will be removed by the cuts, which causes a loss of efficiency of the detector. When defining the cuts, usually these two factors work against each other, and one would always want to maximize one without compromising the other. The goal is that the cuts are optimized in a way such that the number of background events left after all cuts is far less than 1 per year, so that after one year of running the detector, one could hope for a dataset of 0 observed events in the absence of signal.

The software cuts that are applied to the Monte Carlo background data include (1) multiple-hit cut (2) active-veto cut (3) fiducial-volume cut (4) S2/S1 discrimination cut. The definition of these cuts are given in Sec. 3.3.1. Below is a description of how the software cuts are applied in the Monte Carlo simulation. After the results of the simulations have been shown, the rejection power of these cuts will be studied.

4.4.1 Multiple-hit cut

The multiple-hit cut can be applied in the simulation by simply rejecting events that contain more than in one scatter in the detector. Due to the larger size of

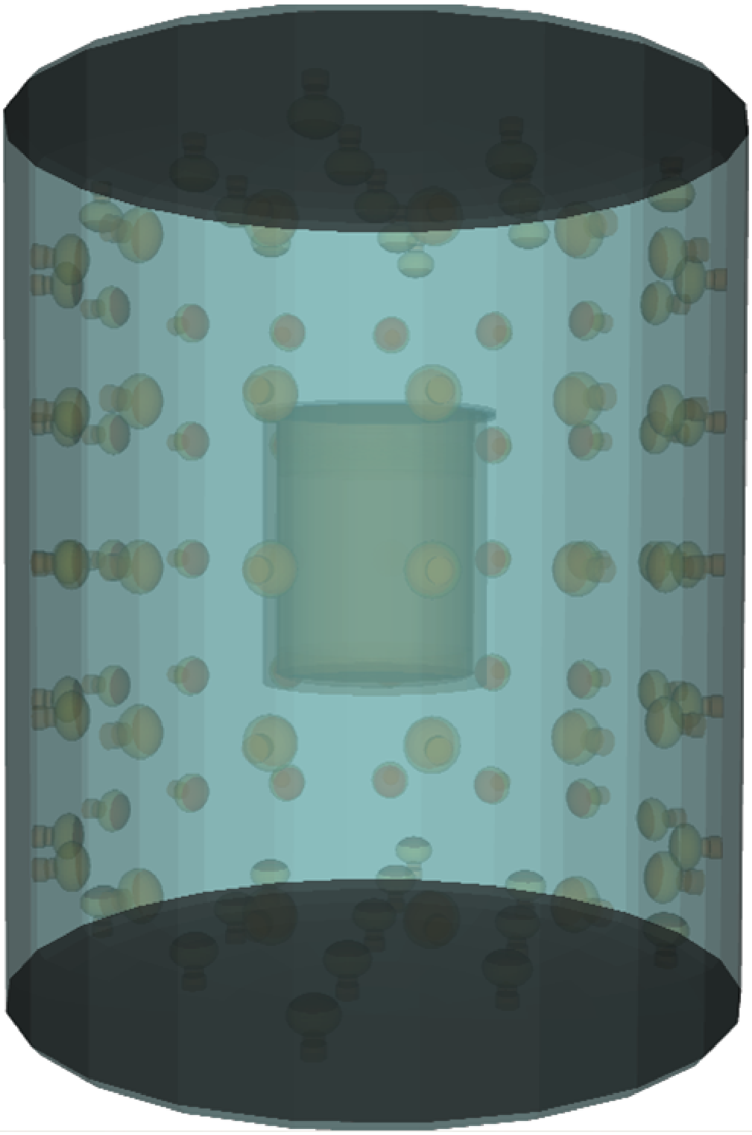

Figure 4.1: The Xenon1T geometry as put into the GEANT4 code. The detector is surrounded by the liquid scintillator veto which is equipped with PMTs

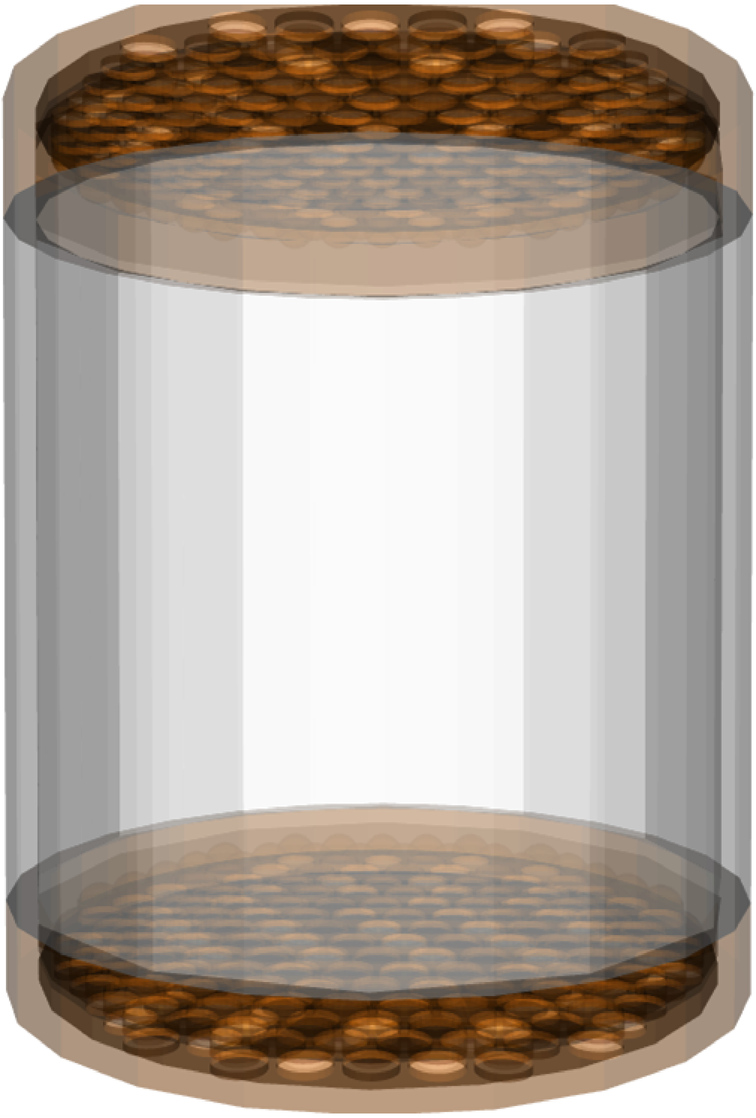

Figure 4.2: The Xenon1T geometry as put into the GEANT4 code. The TPC is shown with QUPIDs at the top and the bottom.

the future detectors, the rejection power of the multiple-hit cut may be increased as compared to the XENON100 detector.

4.4.2 Active-veto cut

The active veto cut is applied in the simulation by rejecting events that deposit energy in the liquid scintillator veto. The rejection power will be dependent on the energy threshold of the veto region.

4.4.3 Fiducial-volume cut

The fiducial volume cut is applied by requiring that the position of the simulated events lie within the fiducial region. The finite position resolution has been ignored, as its effect on the total volume is negligible. In the simulation, the event rate for different fiducial volumes will be compared, which will show that the current choice of fiducial volume is optimized and achieved a good balance between fiducial mass and background level.

4.4.4 S2/S1 cut

The S2/S1 cut is applied in the simulation simply as a constant factor of 0.01 (99% rejection) with no energy dependence. Since the energy spectrum of the gamma background is relatively flat, the use of a constant S2/S1 rejection power will not lead to increased errors of the estimation.

4.5 Radioactivity of materials

The cryostat of the future detectors, which are made with titanium, has lower radioactive contaminants than the stainless steel material that is currently used in XENON100. The conventional Hamamatsu R8520 phototubes will be replaced by the ultra-low radioactive QUPIDs, which are made from pure Quartz and contain no resister chains, further reducing the background [47]. The radioactivity of the QUPIDs were measured with a dedicated screening facility consisting of a 2.2 kg high purity Ge detector in an ultra-low background Cu cryostat and Cu/Pb shield, operated at LNGS. The radioactivity of the materials are listed in Table 4.2 [24]. The radioactivity of the R8520 phototubes and stainless steel in XENON100 is also listed for comparison.

Material	Unit	Quantity	^{238}U [mBq/unit]	^{232}Th	^{40}K	^{60}Co
QUPID	QUPID	242	<0.49	<0.4	<2.4	<0.21
PTFE	kg	40	<0.31	<0.16	<2.2	<0.11
Titanium	kg	400	<0.25	<0.2	<1.3	-
Acrylic	kg	130	<0.014	<0.0045	-	-
Copper	kg	140	<0.07	<0.03	-	<0.0045
R8520	PMT	-	0.31±0.04	0.24±0.06	11±2	0.6±0.1
S.S.	kg	-	<1.7	<1.9	<9.0	5.5±0.6

Table 4.2: Radioactivity of materials

4.6 Simulation Results

4.6.1 Electron Recoil Backgrounds

The internal electron recoil (ER) background is due to gamma rays from the decay chains of radioactive contaminants, mainly ^{238}U, ^{232}Th, ^{40}K, and ^{60}Co. Based on the radioactivity values in Table 4.2, the ER background from the detector materials is simulated with the GEANT4 code. The ER background is lowered by the S2/S1 discrimination with a $\sim$ 99% rejection efficiency.

4.6.1.1 Xenon1T

For Xenon1T, the ER background is greatly reduced, compared to XENON100, by allowing a 10cm LXe self-shielding, as shown in Fig. 4.5. Fig. 4.4 and 4.3 show the energy spectrum with and without multiple-hit cut for various fiducial volume cuts. The estimated number of ER background events are compared in Fig. 4.6.1.3, and the number of events is 0.07 in the 1.1 ton fiducial volume in a 1-ton-year exposure. It can be seen that the rejection power of the multiple-hit cut is very low in the case of electron recoil background. The self-shielding of LXe is very effective in attenuating gamma rays, and the background rate decreases quickly with deeper fiducial cuts. The (r,z) distribution as well as the dru (differential rate unit, events/kg/day/keV) level of the background events is shown in Fig. 4.6 for a 1-year exposure. It can be seen that QUPID is the dominant source of gamma background.

4.6.1.2 Xenon10T

For the Xenon10T detector, the gamma background exhibits similar behavior. Figs. 4.8 and 4.7 show the energy spectrum with and without multiple-hit cut

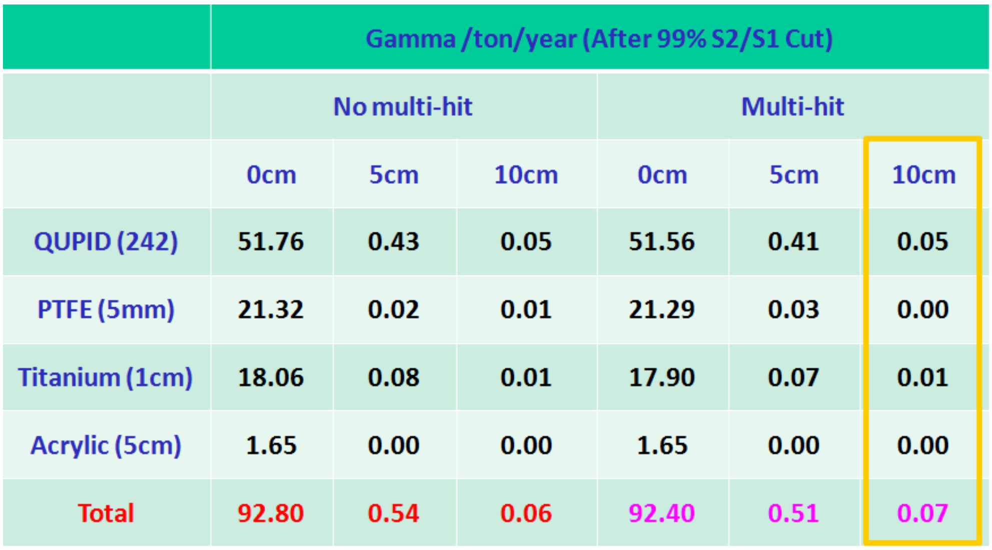

	Gamma /ton/year (After 99% S2/S1 Cut)					
	No multi-hit			Multi-hit		
	0cm	5cm	10cm	0cm	5cm	10cm
QUPID (242)	51.76	0.43	0.05	51.56	0.41	0.05
PTFE (5mm)	21.32	0.02	0.01	21.29	0.03	0.00
Titanium (1cm)	18.06	0.08	0.01	17.90	0.07	0.01
Acrylic (5cm)	1.65	0.00	0.00	1.65	0.00	0.00
Total	92.80	0.54	0.06	92.40	0.51	0.07

Table 4.3: Number of gamma background events for Xenon1T in a 1-ton-year exposure after 99% S2/S1 cut for different detector components. Results are shown with and without multiple-hit cut and for various fiducial cuts (0, 5, and 10 cm).

for various fiducial volume cuts. Since LXe self-shielding is very effective, the background level is further reduced to a negligible level after a 20 cm fiducial volume cut. The (r,z) distribution of the background events is shown in Fig. 4.9 for a 1-year exposure.

4.6.1.3 Argon5T and Argon50T

For argon detectors, electron recoil background can be significantly reduced by pulse shape discrimination [54] and becomes negligible and so were not simulated.

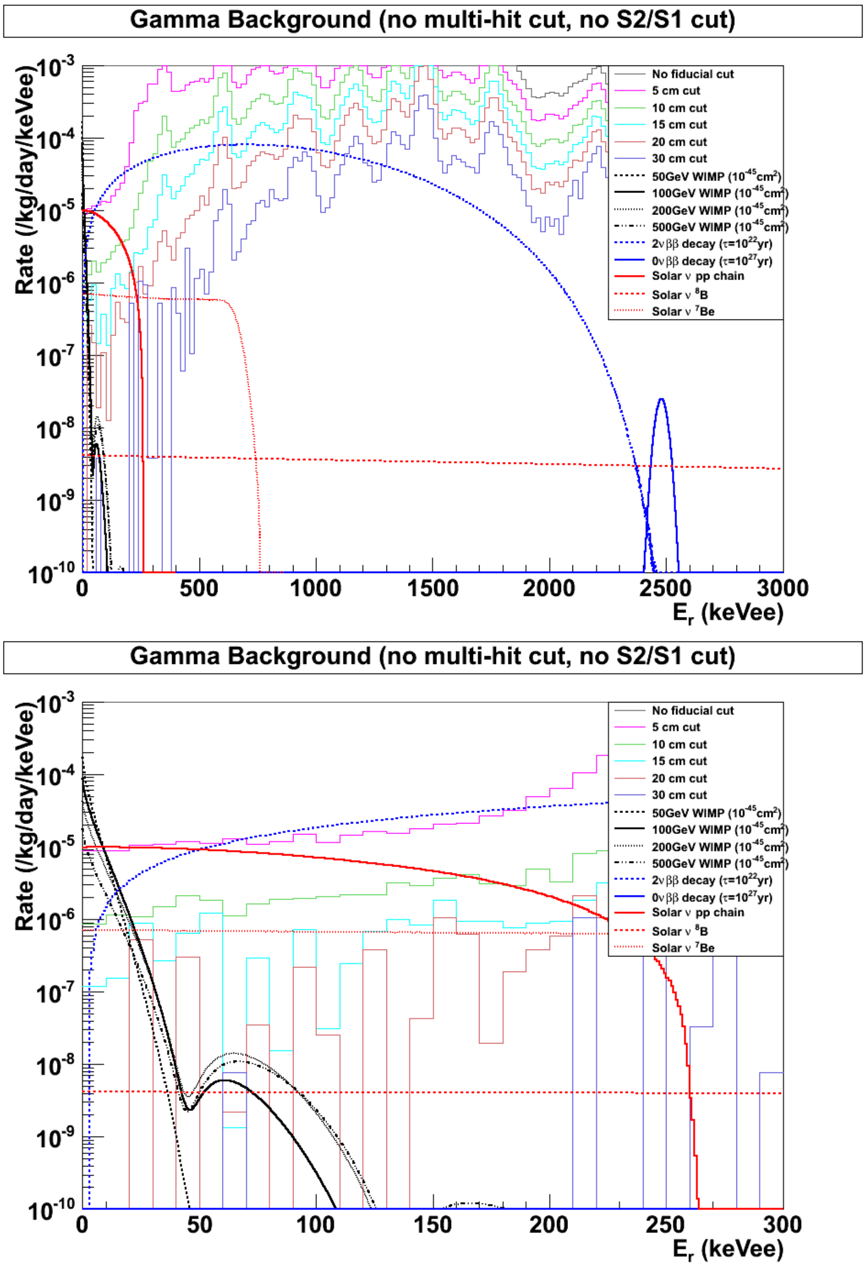

Figure 4.3: Energy spectrum of ER backgrounds (no S2/S1 cut) for Xenon1T without multiple-hit cut. Background rates are plotted for different fiducial cuts: 0 cm (black), 5 cm (pink), 10 cm (green), 15 cm (light blue), 20 cm (brown), and 30 cm (purple). Also shown are the WIMP spectrum at $\sigma = 10^{-45}$ cm^2 for various WIMP masses: 50 GeV (dashed), 100 GeV (solid), 200 GeV (dotted), 500 GeV (dash-dotted).

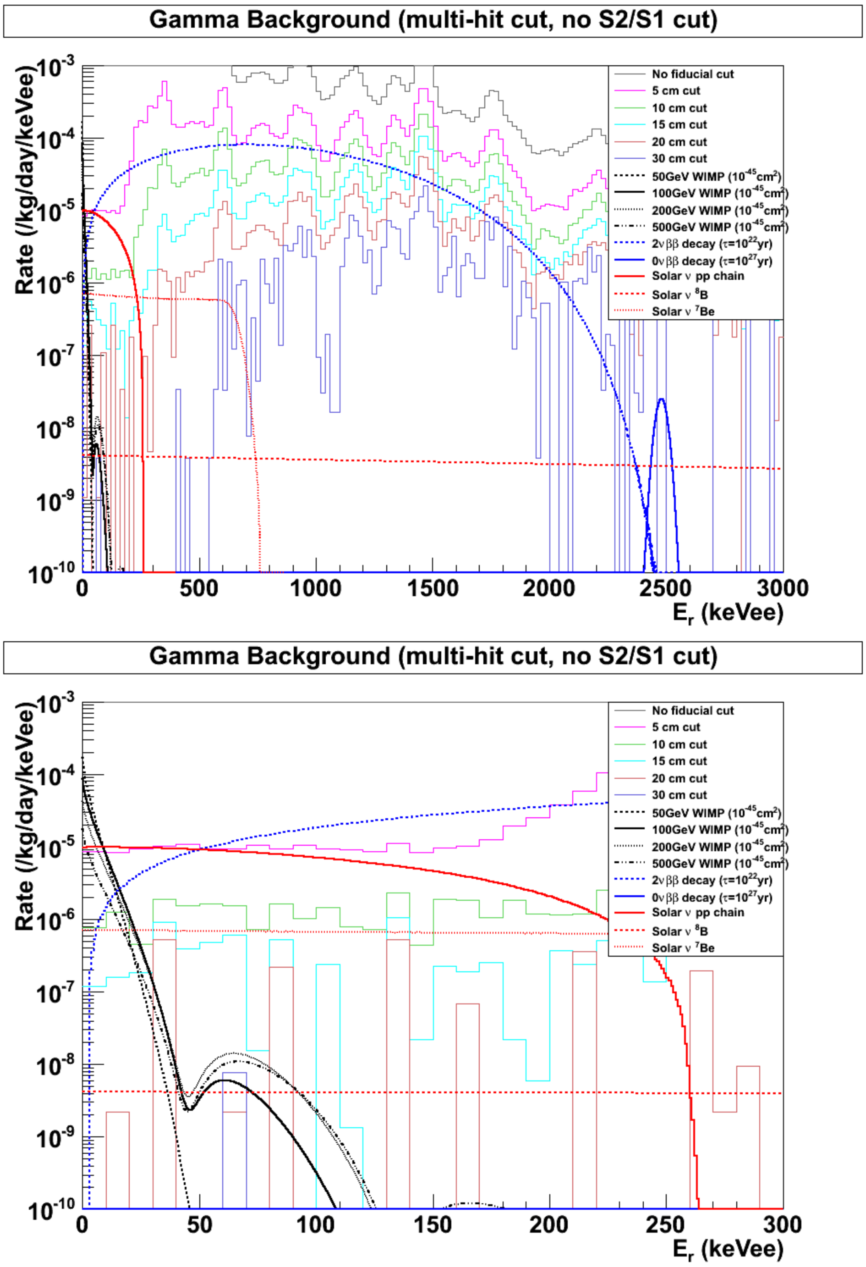

Figure 4.4: Energy spectrum of ER backgrounds (no S2/S1 cut) for Xenon1T with multiple-hit cut. Background rates are plotted for different fiducial cuts: 0 cm (black), 5 cm (pink), 10 cm (green), 15 cm (light blue), 20 cm (brown), and 30 cm (purple). Also shown are the WIMP spectrum at $\sigma = 10^{-45}$ cm^2 for various WIMP masses: 50 GeV (dashed), 100 GeV (solid), 200 GeV (dotted), 500 GeV (dash-dotted).

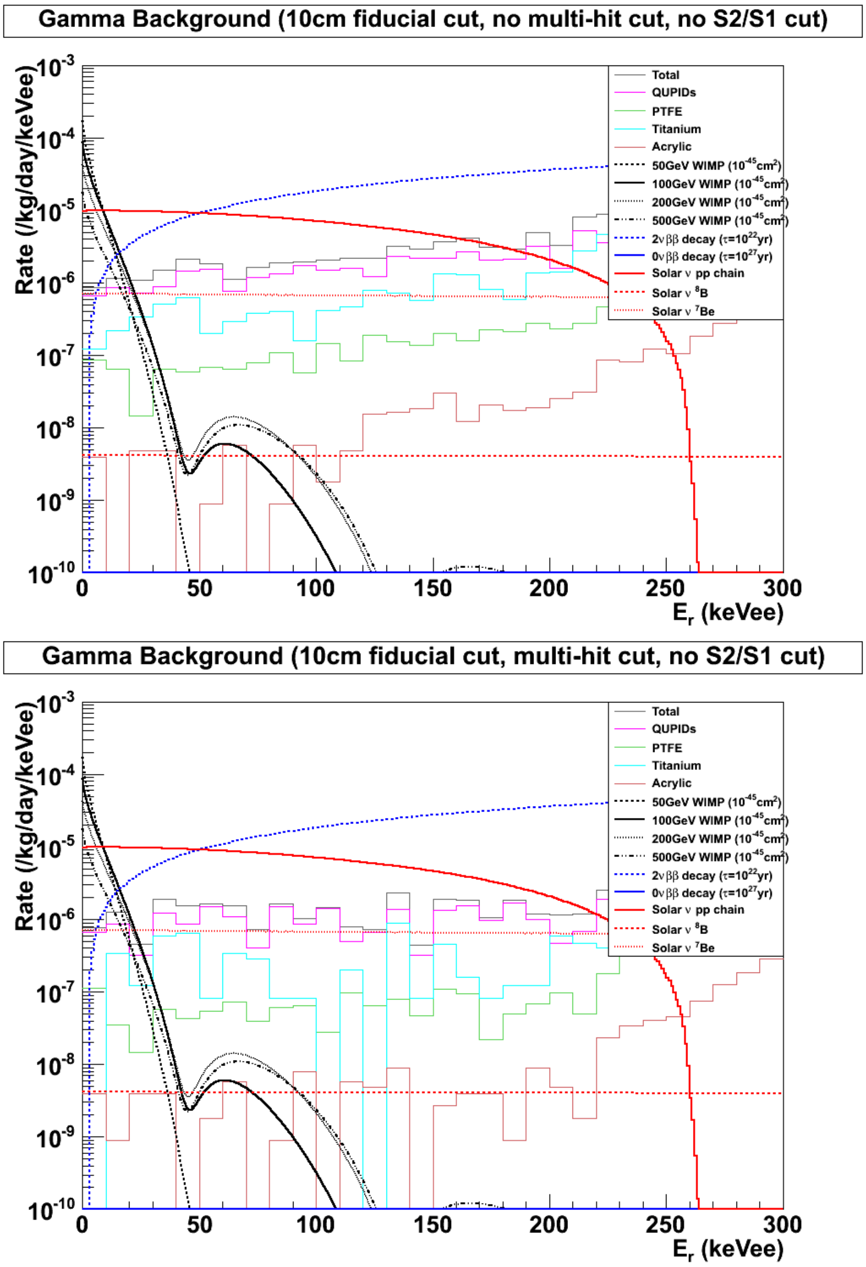

Figure 4.5: Energy spectrum of ER backgrounds (no S2/S1 cut) for Xenon1T for 10 cm fiducial cut with (bottom) and without (top) multiple-hit cut. Background rates are plotted for different detector materials: QUPID (pink), PTFE (green), titanium (light blue), acrylic (brown), and total (black). Also shown are the WIMP spectrum at $\sigma = 10^{-45}$ cm^2 for various WIMP masses: 50 GeV (dashed), 100 GeV (solid), 200 GeV (dotted), 500 GeV (dash-dotted).

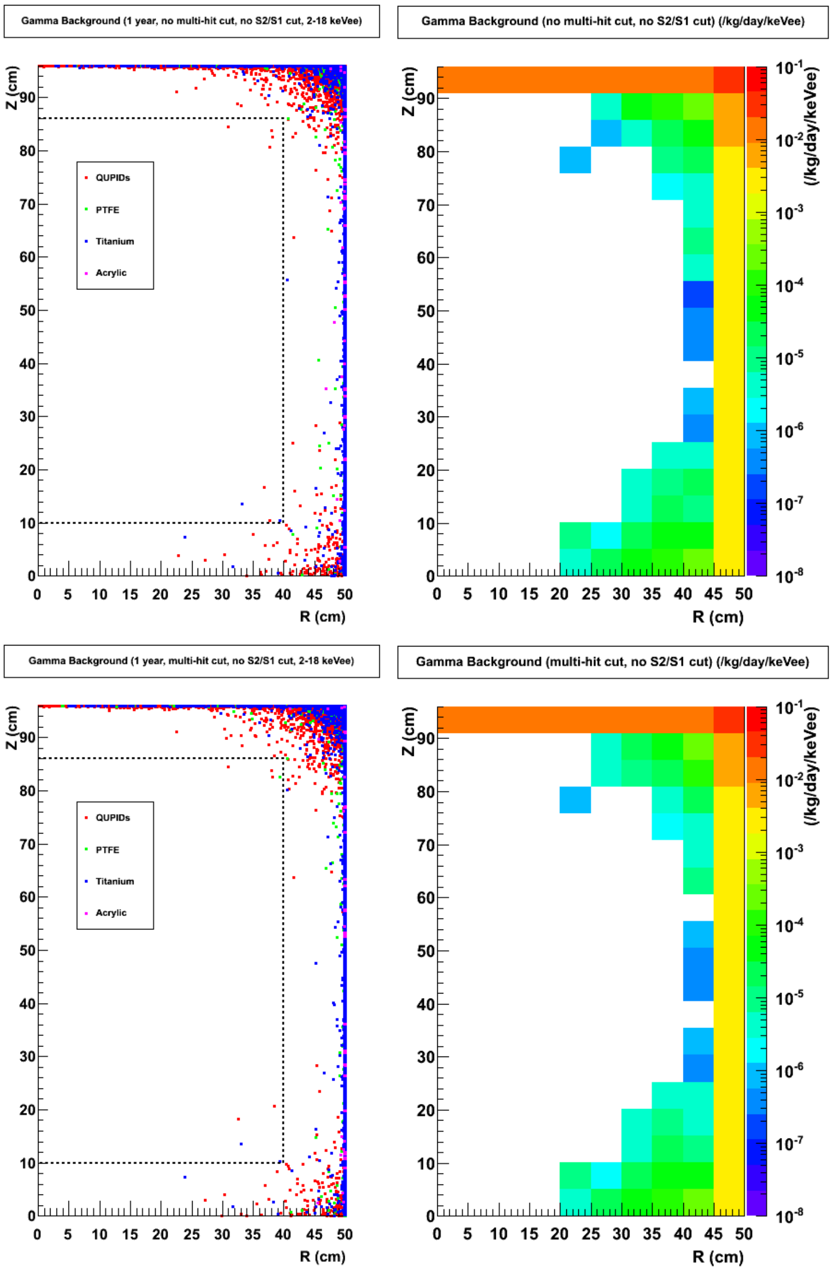

Figure 4.6: Left: r vs z distribution of Xenon1T ER background events (no S2/S1 cut) in a one-year exposure with (bottom) and without (top) multiple-hit cut, for QUPIDs (red), PTFE (green), titanium (blue), and acrylic (pink). Right: r vs z distribution of ER background rate in units of dru$_{ee}$ (/kg/day/keV$_{ee}$) with (bottom) and without (top) multiple-hit cut

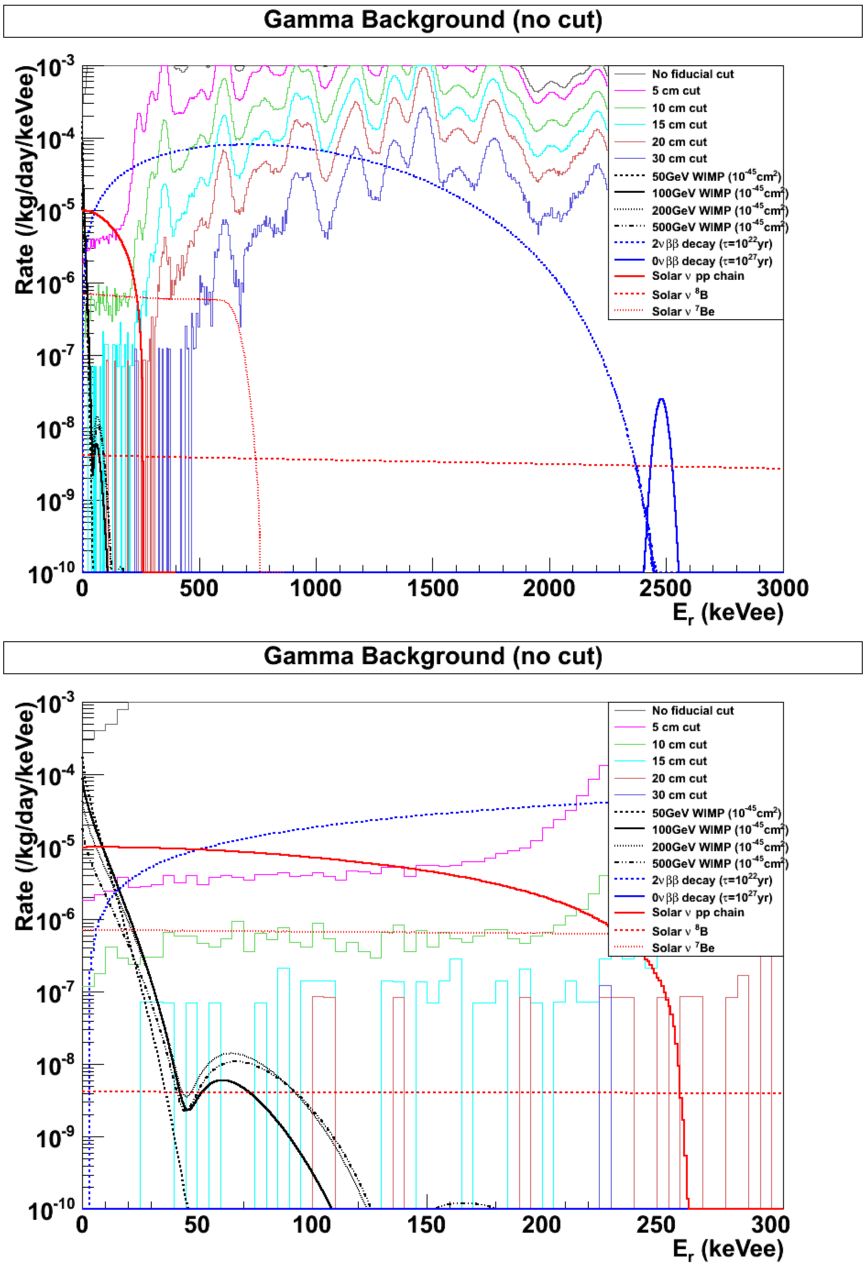

Figure 4.7: Energy spectrum of ER backgrounds (no S2/S1 cut) for Xenon10T without multiple-hit cut. Background rates are plotted for different fiducial cuts: 0 cm (black), 5 cm (pink), 10 cm (green), 15 cm (light blue), 20 cm (brown), and 30 cm (purple). Also shown are the WIMP spectrum at $\sigma = 10^{-45}$ cm^2 for various WIMP masses: 50 GeV (dashed), 100 GeV (solid), 200 GeV (dotted), 500 GeV (dash-dotted).

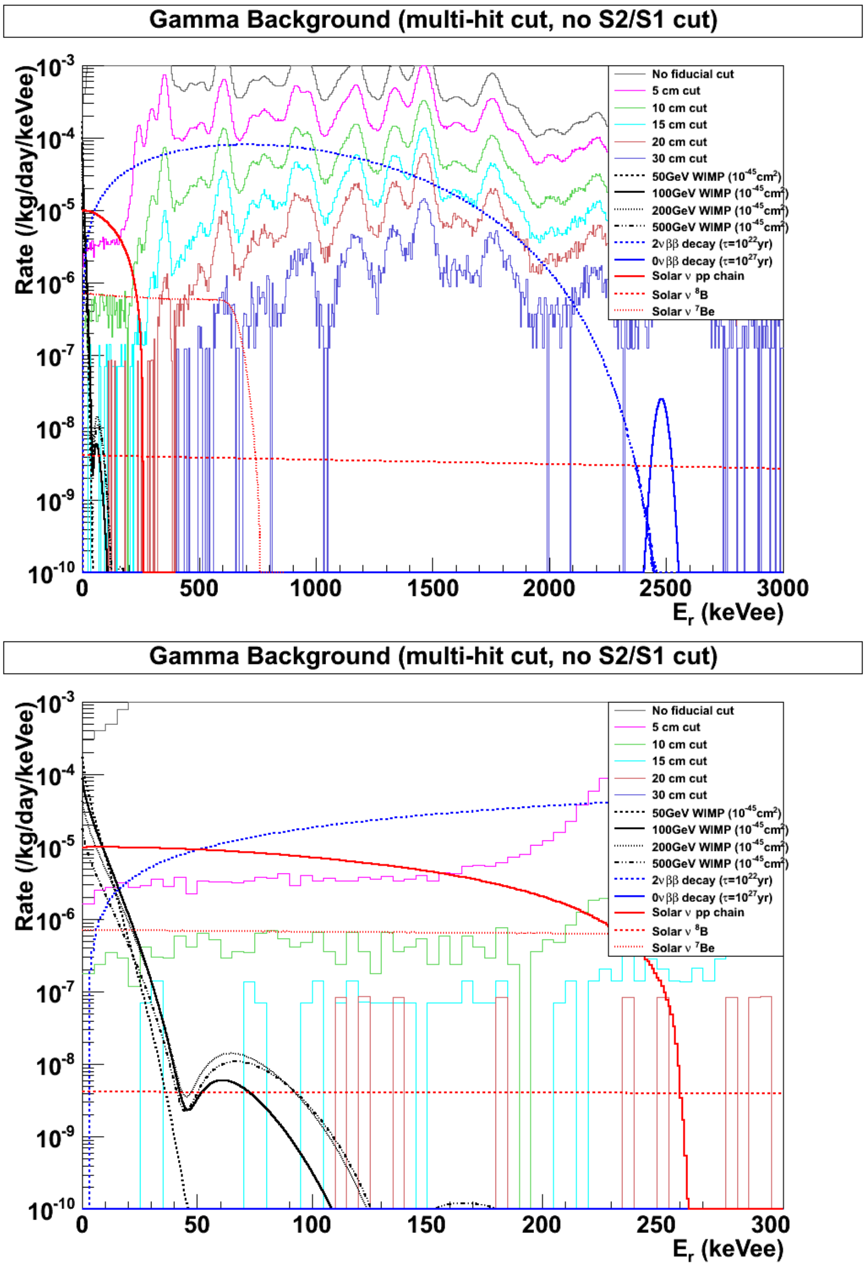

Figure 4.8: Energy spectrum of ER backgrounds (no S2/S1 cut) for Xenon10T with multiple-hit cut. Background rates are plotted for different fiducial cuts: 0 cm (black), 5 cm (pink), 10 cm (green), 15 cm (light blue), 20 cm (brown), and 30 cm (purple). Also shown are the WIMP spectrum at $\sigma = 10^{-45}$ cm^2 for various WIMP masses: 50 GeV (dashed), 100 GeV (solid), 200 GeV (dotted), 500 GeV (dash-dotted).

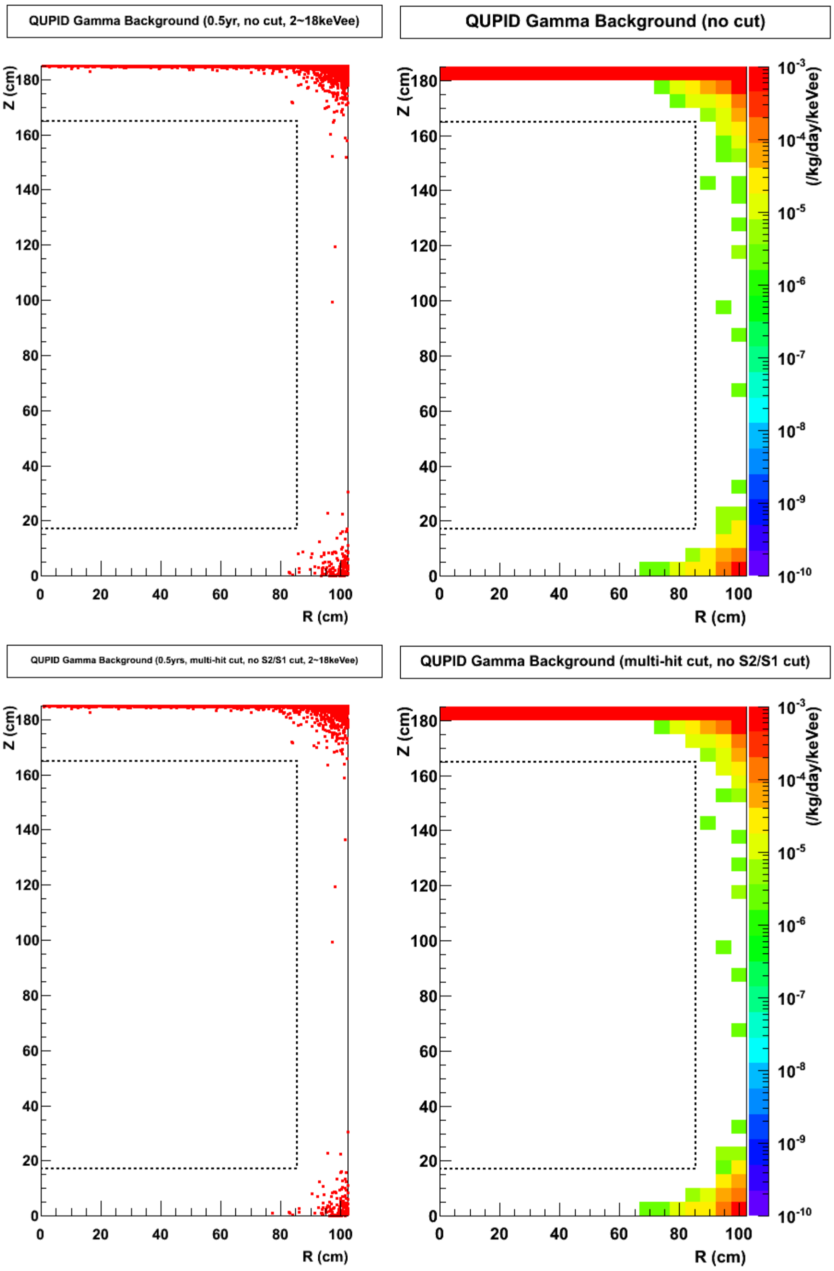

Figure 4.9: Left: r vs z distribution of Xenon10T ER background events (no S2/S1 cut) in a one-year exposure with (bottom) and without (top) multiple-hit cut. Right: r vs z distribution of ER background rate in units of dru$_{ee}$ (/kg/day/keV$_{ee}$) with (bottom) and without (top) multiple-hit cut

4.6.2 Nuclear Recoil Backgrounds

The internal nuclear recoil (NR) background is due to neutrons produced by spontaneous fission and (α, n) reactions of U/Th decays. Using the radioactivity values in Table 4.2, the NR background is estimated with the GEANT4 code, using the neutron spectra given in [53].

4.6.2.1 Xenon1T

Due to the large size of the Xenon1T detector, the neutron background can be reduced by rejecting multiple-scattered neutrons in the detector volume. The predicted number of NR background events is 0.1/ton/year (Table 4.5). The total background level from the detector materials is well below the event rate of a dark matter signal at 100 GeV WIMP mass and 10^{-45} cm^2 WIMP-nucleon cross section, as shown in Fig. 4.11. Fig. 4.12 shows the (r,z) distribution of the neutron background events in a 100-year exposure both with and without multiple-hit cut. The number of events is greatly reduced after the multiple-hit has been applied.

4.6.2.2 Xenon10T

Fig. 4.13 shows the energy spectrum of the neutron background for the Xenon10T detector. Fig. 4.12 shows the (r,z) distribution of the neutron background events in a 100-year exposure without multiple-hit cut, with multiple-hit cut, and with both the multiple-hit and active-veto cuts applied. The background is lowered by a factor of $\sim 1/7$ by the multiple-hit cut, and is lowered by a factor of $\sim 1/4$ by the active veto cut. The expected number of neutron background events is 0.03 neutron/year.

4.6.2.3 Argon5T

Fig. 4.15 shows the energy spectrum of the neutron background for the Argon5T detector. Compared to the xenon detectors, the neutron energy spectrum in argon is relatively flat, and so with the wider energy window of $45 - 200$ keVr, more neutron background events are expected to be seen. Fig. 4.16 shows the (r,z) distribution of the neutron background events in a 100-year exposure without multiple-hit cut, with multiple-hit cut, and with both the multiple-hit and active-veto cuts applied. The background is drastically lowered by a factor of $\sim 1/17$ by the multiple-hit cut, and is lowered by a factor of $\sim 1/8$ by the active veto cut. This shows that the rejection power of the multiple-hit cut is much higher in an argon detector than in a xenon detector. The expected number of neutron background events is 0.1 neutron/year.

4.6.2.4 Argon50T

Fig. 4.17 shows the energy spectrum of the neutron background for the Argon50T detector. Fig. 4.16 shows the (r,z) distribution of the neutron background events in a 100-year exposure without multiple-hit cut, with multiple-hit cut, and with both the multiple-hit and active-veto cuts applied. The background is drastically lowered by a factor of $\sim 1/20$ by the multiple-hit cut, and is lowered by a factor of $\sim 1/5.5$ by the active veto cut. The rejection power of the multiple-hit cut in the Argon50T detector is higher than that of the Argon5T detector as expected, since a neutron will have a higher chance of scattering multiple times in a larger volume. The expected number of neutron background events is 0.39 neutron/year. Fig. 4.6.2.4 summarizes the number of events in different detectors for various fiducial volume cuts.

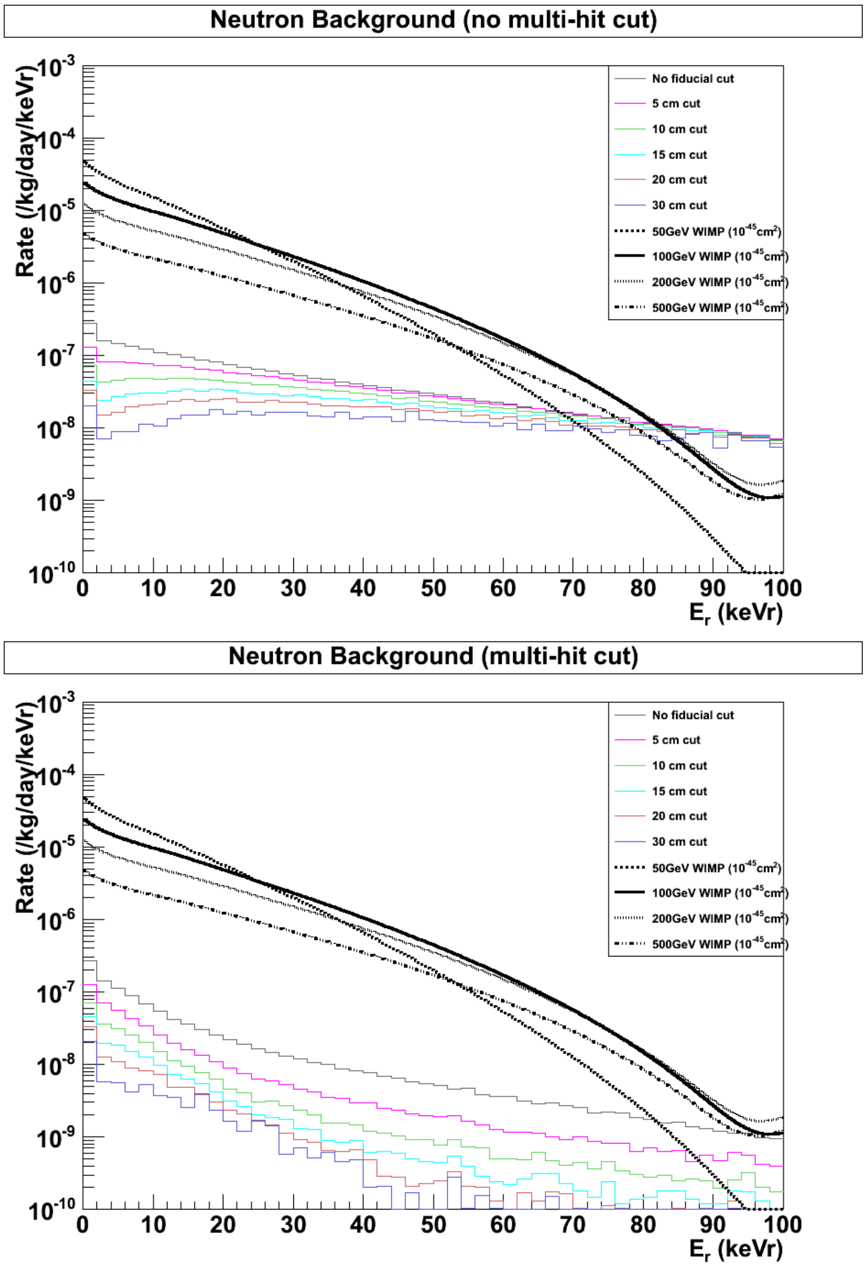

Figure 4.10: Energy spectrum of NR backgrounds for Xenon1T between $0 - 100$ keVr with (bottom) and without (top) multiple-hit cut. Background rates are plotted for different fiducial cuts: 0 cm (black), 5 cm (pink), 10 cm (green), 15 cm (light blue), 20 cm (brown), and 30 cm (purple). Also shown are the WIMP spectrum at $\sigma = 10^{-45}$ cm^2 for various WIMP masses: 50 GeV (dashed), 100 GeV (solid), 200 GeV (dotted), 500 GeV (dash-dotted).

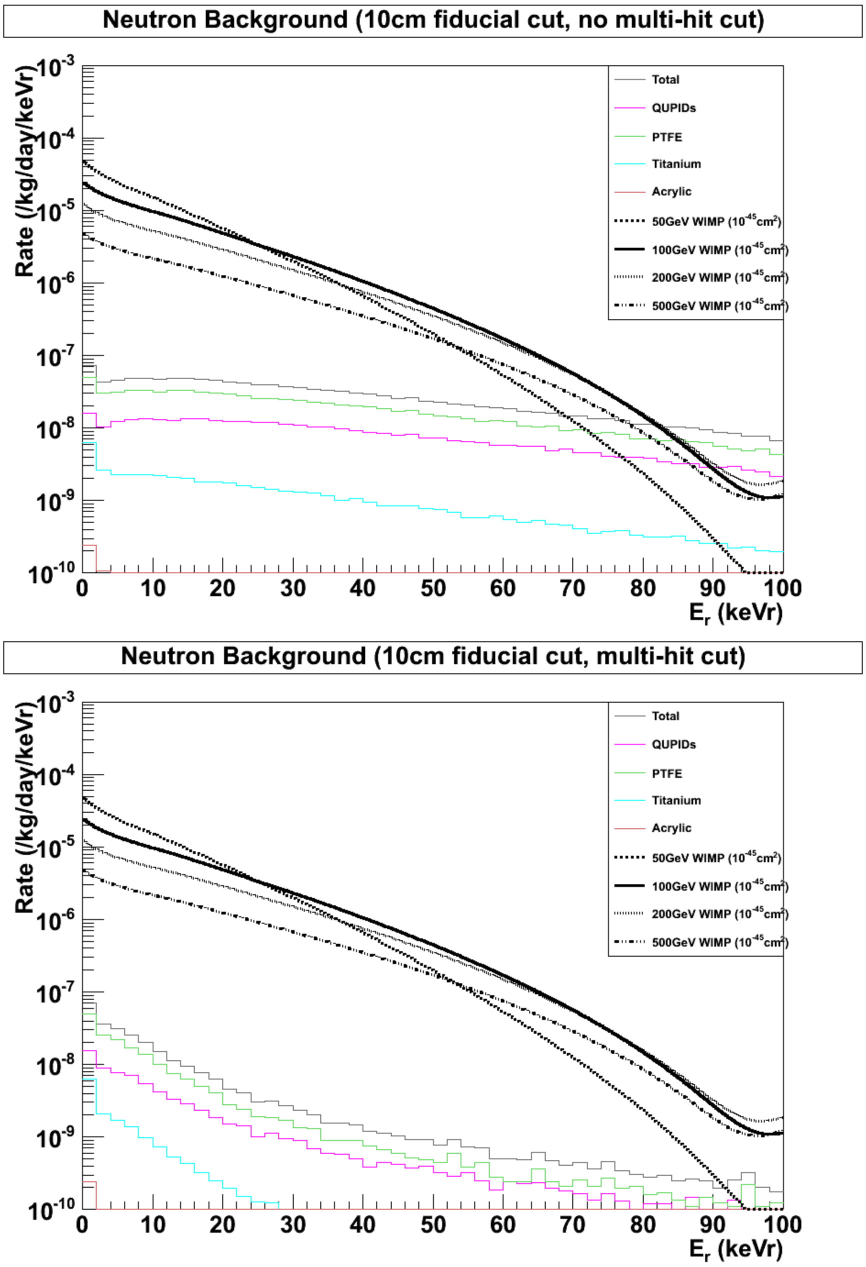

Figure 4.11: Energy spectrum of NR backgrounds for Xenon1T for 10 cm fiducial cut with (bottom) and without (top) multiple-hit cut. Background rates are plotted for different detector materials: QUPID (pink), PTFE (green), titanium (light blue), acrylic (brown), and total (black). Also shown are the WIMP spectrum at $\sigma = 10^{-45}$ cm^2 for various WIMP masses: 50 GeV (dashed), 100 GeV (solid), 200 GeV (dotted), 500 GeV (dash-dotted).

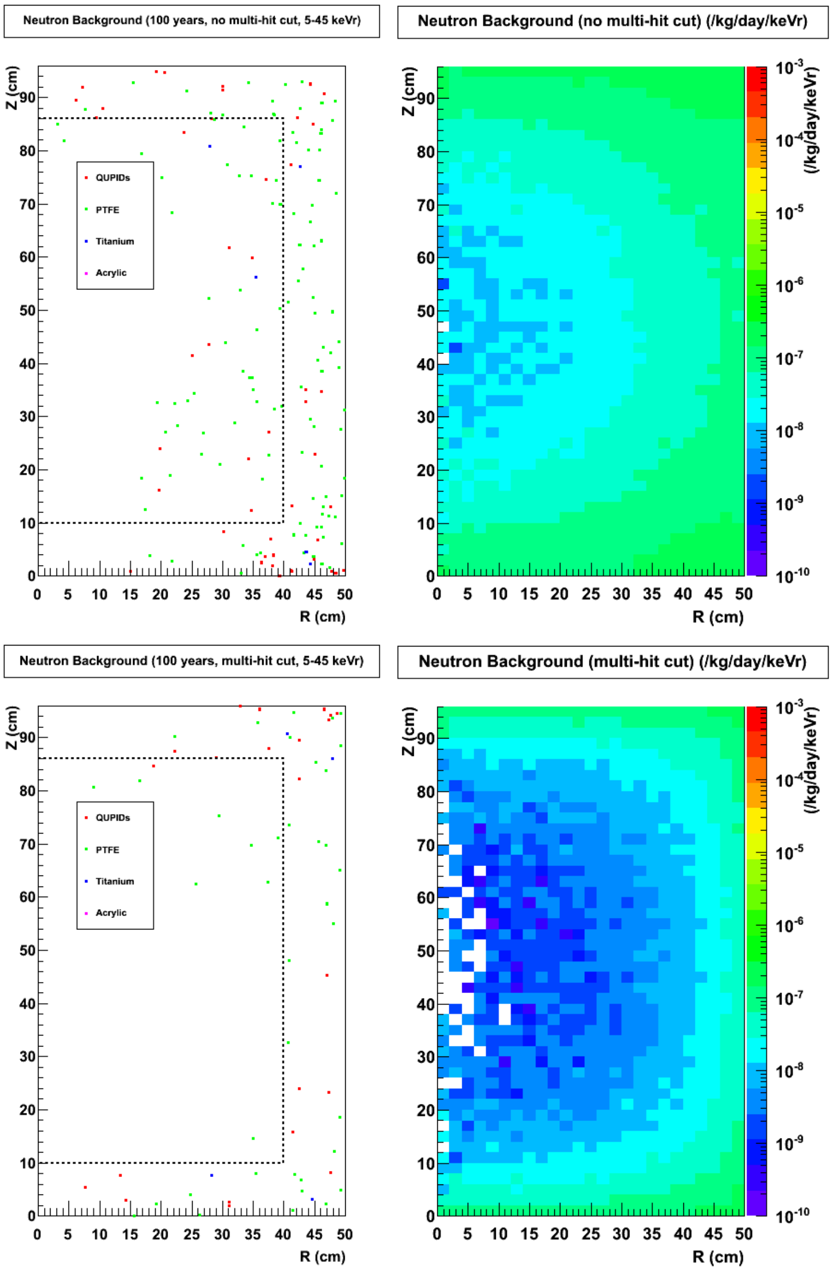

Figure 4.12: Left: r vs z distribution of Xenon1T NR background events in a 100-year exposure with (bottom) and without (top) multiple-hit cut, for QUPIDs (red), PTFE (green), titanium (blue), and acrylic (pink). Right: r vs z distribution of NR background rate in units of $\mathrm{dru}_{\mathrm{nr}}$ ($/kg/day/keV_{nr}$) with (bottom) and without (top) multiple-hit cut

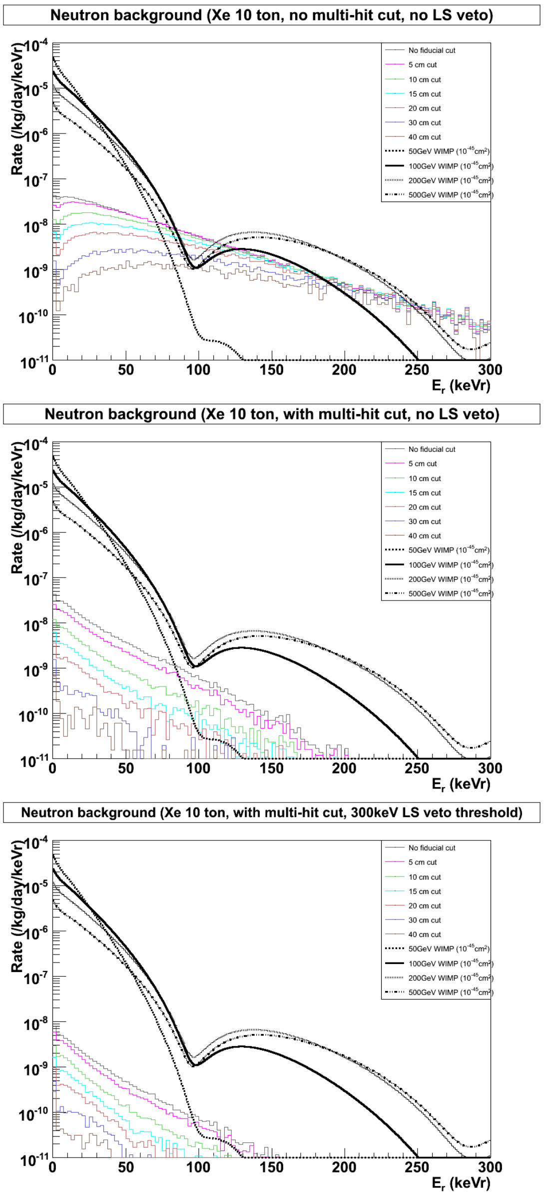

Figure 4.13: Energy spectrum of NR backgrounds for Xenon10T between with (middle) and without (top) multiple-hit cut. Bottom plot shows the spectrum with both the multiple-hit cut and the active LS veto. Background rates are plotted for different fiducial cuts: 0 cm (black), 5 cm (pink), 10 cm (green), 15 cm (light blue), 20 cm (brown), and 30 cm (purple). Also shown are the WIMP spectrum at $\sigma = 10^{-45}$ cm^2 for various WIMP masses: 50 GeV (dashed), 100 GeV (solid), 200 GeV (dotted), 500 GeV (dash-dotted).

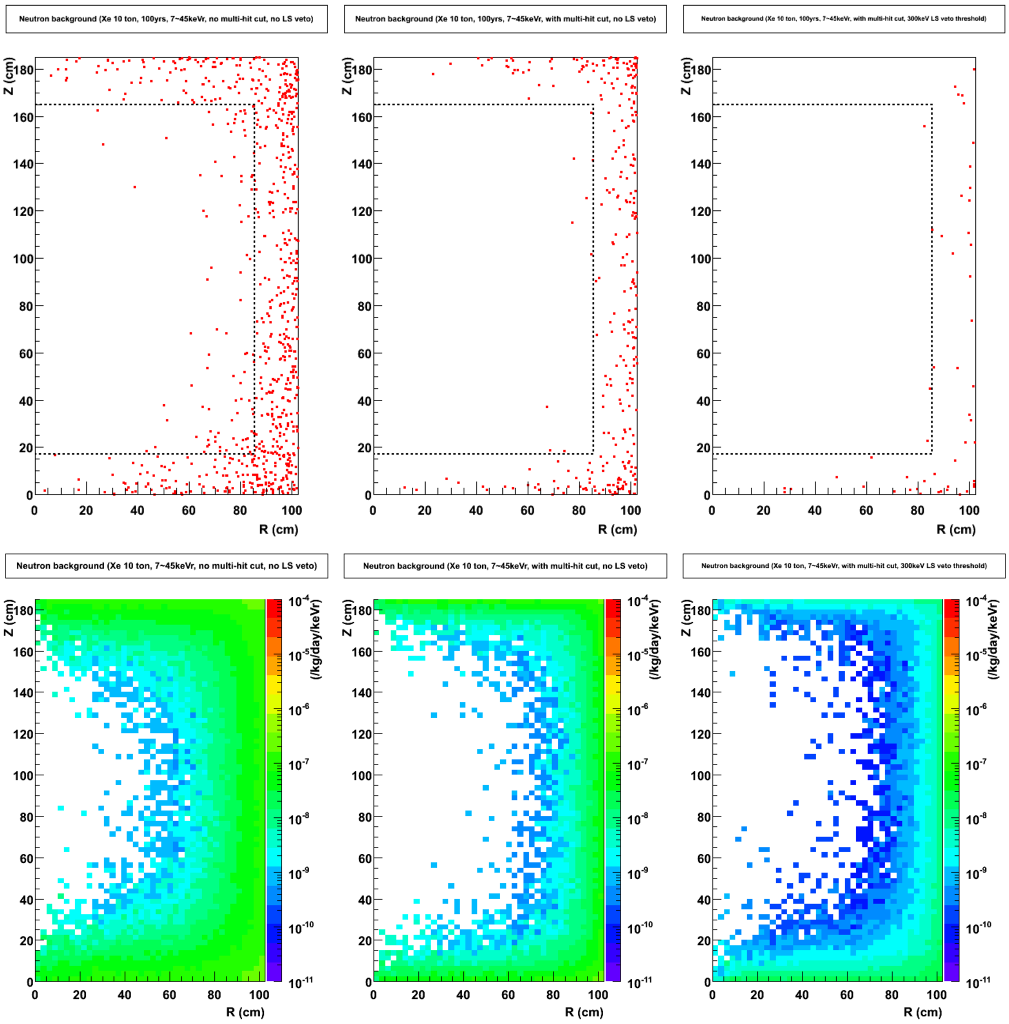

Figure 4.14: Top: r vs z distribution of Xenon10T NR background events in a 100-year exposure with (middle) and without (left) multiple-hit cut. Right plot shows the events with both the multiple-hit cut and the active LS veto. Bottom: r vs z distribution of NR background rate in units of $\mathrm{dru}_{\mathrm{nr}}$ $(/kg/day/keV_{nr})$

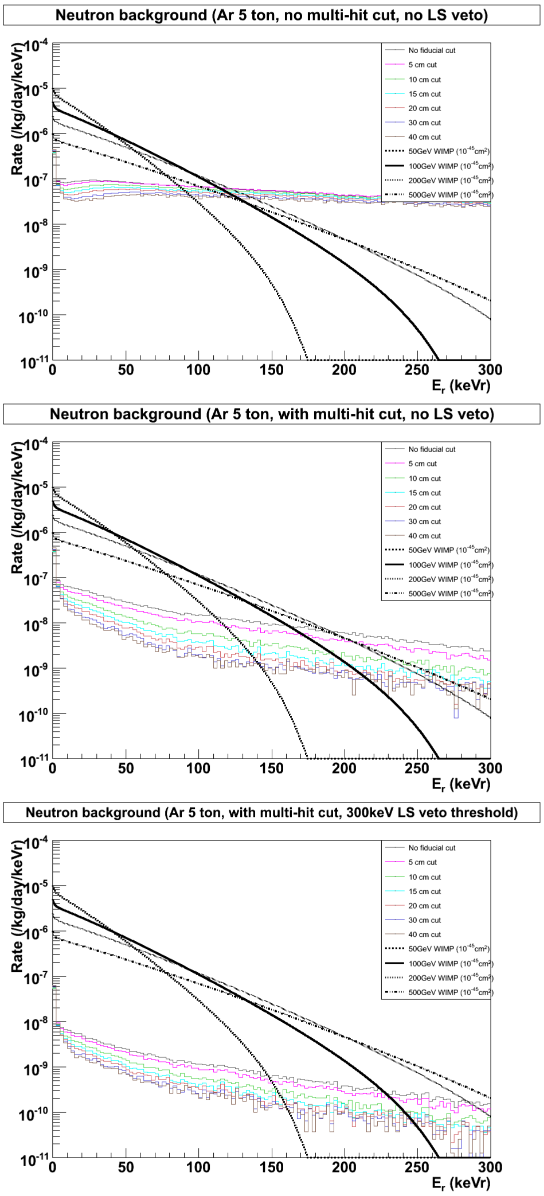

Figure 4.15: Energy spectrum of NR backgrounds for Argon5T between with (middle) and without (top) multiple-hit cut. Bottom plot shows the spectrum with both the multiple-hit cut and the active LS veto. Background rates are plotted for different fiducial cuts: 0 cm (black), 5 cm (pink), 10 cm (green), 15 cm (light blue), 20 cm (brown), and 30 cm (purple). Also shown are the WIMP spectrum at $\sigma = 10^{-45}$ cm^2 for various WIMP masses: 50 GeV (dashed), 100 GeV (solid), 200 GeV (dotted), 500 GeV (dash-dotted).

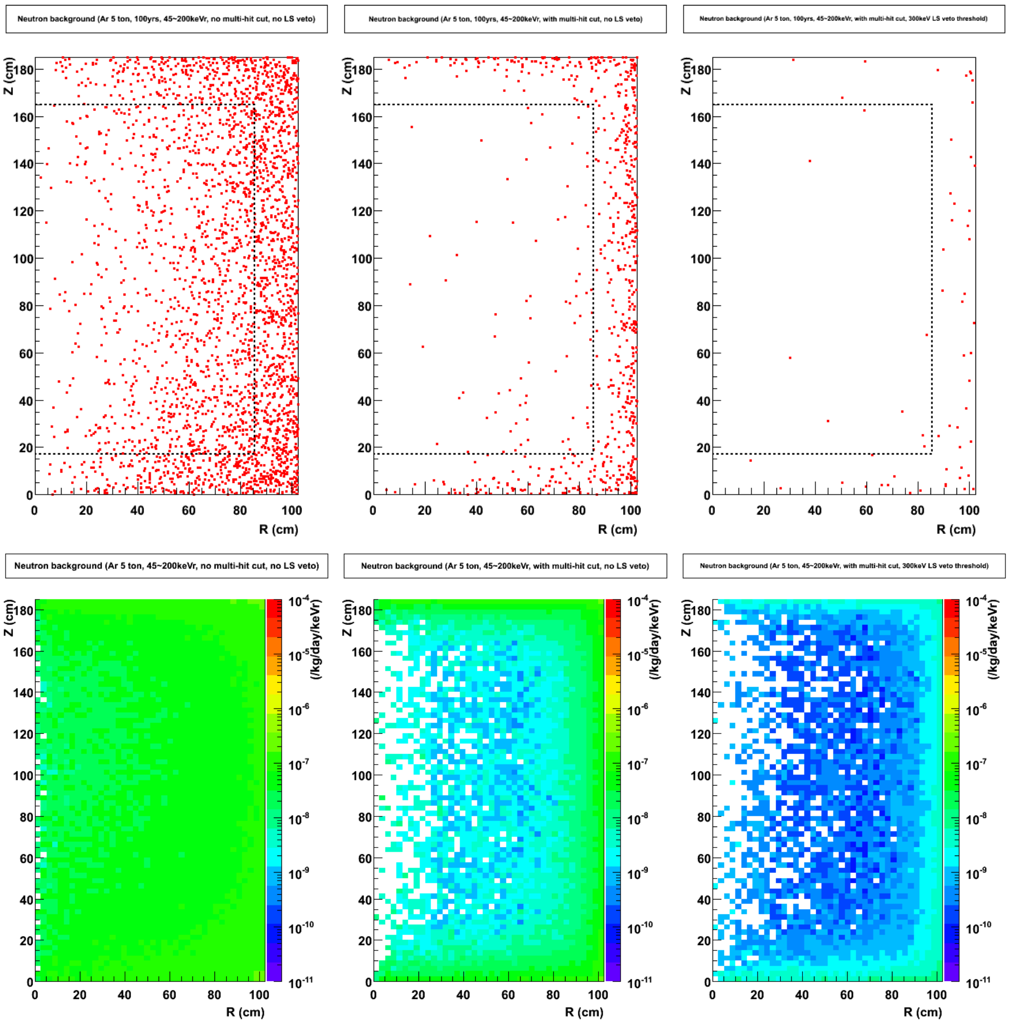

Figure 4.16: Top: r vs z distribution of Argon5T NR background events in a 100-year exposure with (middle) and without (left) multiple-hit cut. Right plot shows the events with both the multiple-hit cut and the active LS veto. Bottom: r vs z distribution of NR background rate in units of $\mathrm{dru_{nr}}$ $(/kg/day/keV_{nr})$

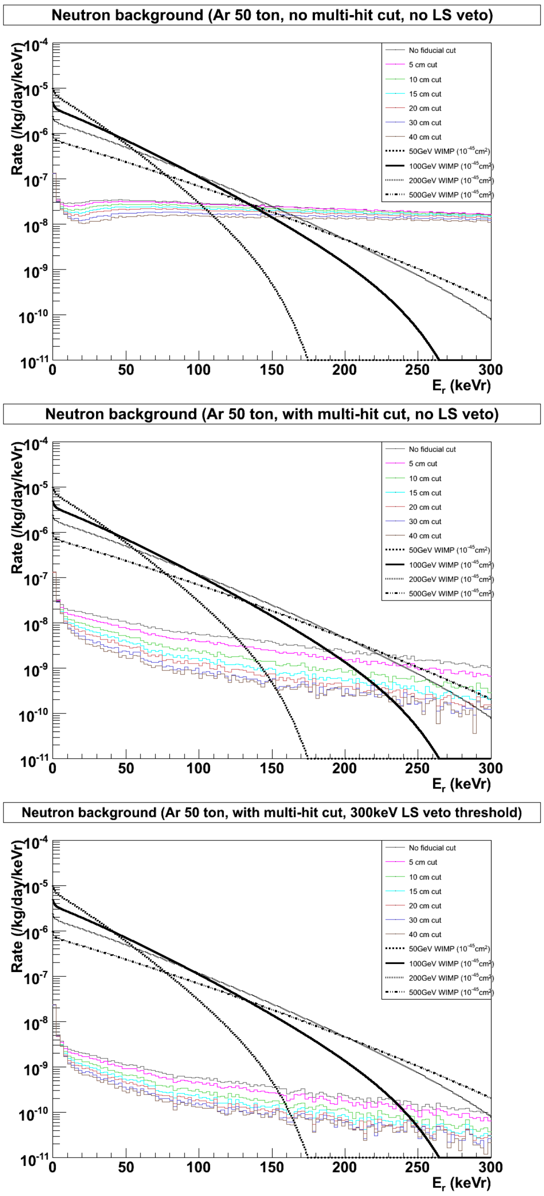

Figure 4.17: Energy spectrum of NR backgrounds for Argon5T between with (middle) and without (top) multiple-hit cut. Bottom plot shows the spectrum with both the multiple-hit cut and the active LS veto. Background rates are plotted for different fiducial cuts: 0 cm (black), 5 cm (pink), 10 cm (green), 15 cm (light blue), 20 cm (brown), and 30 cm (purple). Also shown are the WIMP spectrum at $\sigma = 10^{-45}$ cm^2 for various WIMP masses: 50 GeV (dashed), 100 GeV (solid), 200 GeV (dotted), 500 GeV (dash-dotted).

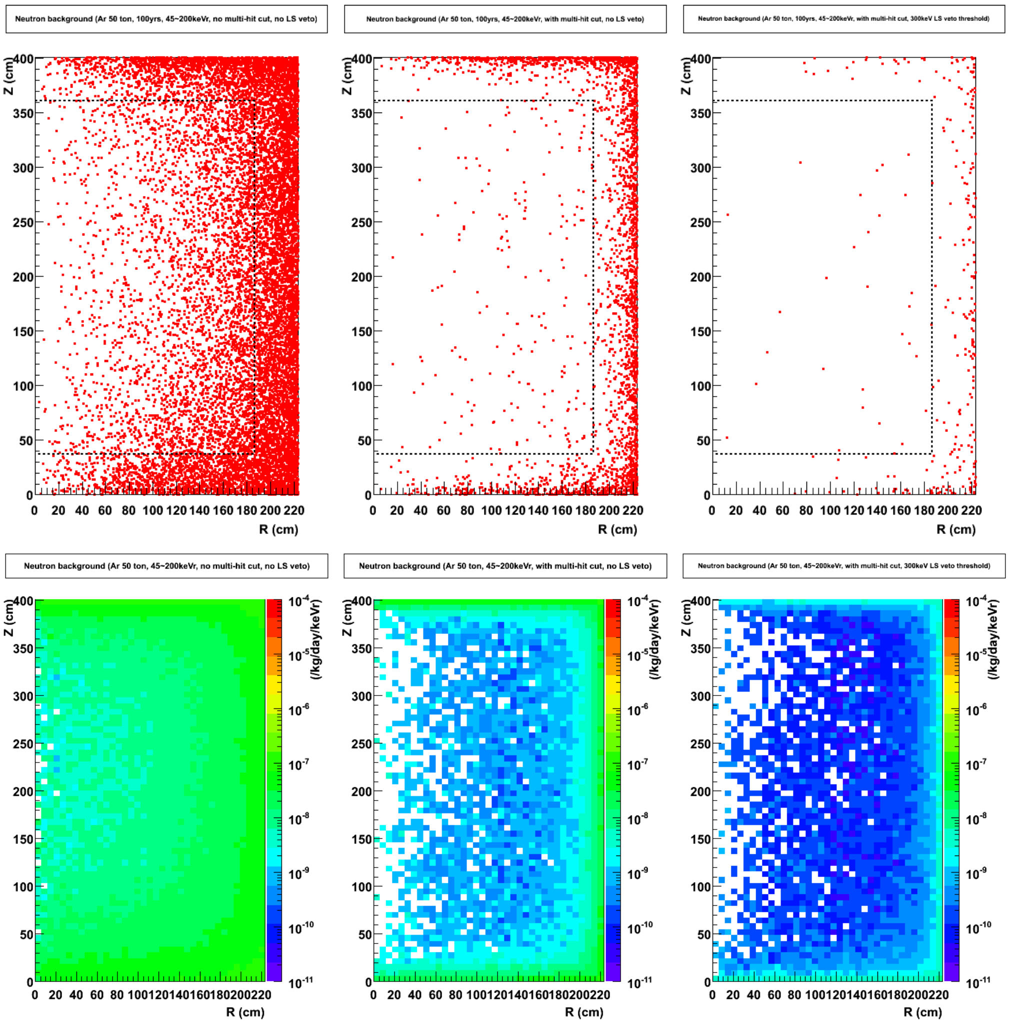

Figure 4.18: Top: r vs z distribution of Argon50T NR background events in a 100-year exposure with (middle) and without (left) multiple-hit cut. Right plot shows the events with both the multiple-hit cut and the active LS veto. Bottom: r vs z distribution of NR background rate in units of $\mathrm{dru_{nr}}$ $(/kg/day/keV_{nr})$

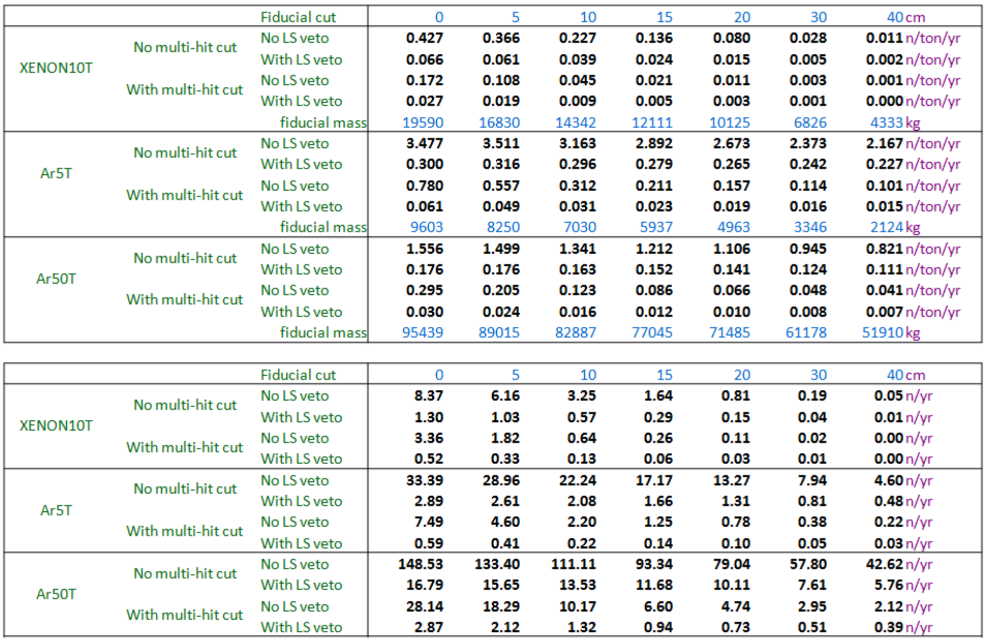

		Fiducial cut	0	5	10	15	20	30	40 cm
XENON10T	No multi-hit cut	No LS veto	0.427	0.366	0.227	0.136	0.080	0.028	0.011 n/ton/yr
		With LS veto	0.066	0.061	0.039	0.024	0.015	0.005	0.002 n/ton/yr
	With multi-hit cut	No LS veto	0.172	0.108	0.045	0.021	0.011	0.003	0.001 n/ton/yr
		With LS veto	0.027	0.019	0.009	0.005	0.003	0.001	0.000 n/ton/yr
		fiducial mass	19590	16830	14342	12111	10125	6826	4333 kg
Ar5T	No multi-hit cut	No LS veto	3.477	3.511	3.163	2.892	2.673	2.373	2.167 n/ton/yr
		With LS veto	0.300	0.316	0.296	0.279	0.265	0.242	0.227 n/ton/yr
	With multi-hit cut	No LS veto	0.780	0.557	0.312	0.211	0.157	0.114	0.101 n/ton/yr
		With LS veto	0.061	0.049	0.031	0.023	0.019	0.016	0.015 n/ton/yr
		fiducial mass	9603	8250	7030	5937	4963	3346	2124 kg
Ar50T	No multi-hit cut	No LS veto	1.556	1.499	1.341	1.212	1.106	0.945	0.821 n/ton/yr
		With LS veto	0.176	0.176	0.163	0.152	0.141	0.124	0.111 n/ton/yr
	With multi-hit cut	No LS veto	0.295	0.205	0.123	0.086	0.066	0.048	0.041 n/ton/yr
		With LS veto	0.030	0.024	0.016	0.012	0.010	0.008	0.007 n/ton/yr
		fiducial mass	95439	89015	82887	77045	71485	61178	51910 kg

		Fiducial cut	0	5	10	15	20	30	40 cm
XENON10T	No multi-hit cut	No LS veto	8.37	6.16	3.25	1.64	0.81	0.19	0.05 n/yr
		With LS veto	1.30	1.03	0.57	0.29	0.15	0.04	0.01 n/yr
	With multi-hit cut	No LS veto	3.36	1.82	0.64	0.26	0.11	0.02	0.00 n/yr
		With LS veto	0.52	0.33	0.13	0.06	0.03	0.01	0.00 n/yr
Ar5T	No multi-hit cut	No LS veto	33.39	28.96	22.24	17.17	13.27	7.94	4.60 n/yr
		With LS veto	2.89	2.61	2.08	1.66	1.31	0.81	0.48 n/yr
	With multi-hit cut	No LS veto	7.49	4.60	2.20	1.25	0.78	0.38	0.22 n/yr
		With LS veto	0.59	0.41	0.22	0.14	0.10	0.05	0.03 n/yr
Ar50T	No multi-hit cut	No LS veto	148.53	133.40	111.11	93.34	79.04	57.80	42.62 n/yr
		With LS veto	16.79	15.65	13.53	11.68	10.11	7.61	5.76 n/yr
	With multi-hit cut	No LS veto	28.14	18.29	10.17	6.60	4.74	2.95	2.12 n/yr
		With LS veto	2.87	2.12	1.32	0.94	0.73	0.51	0.39 n/yr

Table 4.4: Expected number of neutron background events per ton-year (top) and per year (bottom) of exposure, with and without multiple-hit cut, with and without liquid scintillator veto, for different fiducial volume cuts (0, 5, 10, 15, 20, and 30 cm). Also listed are the fiducial mass for different fiducial volume cuts.

4.6.3 Summary

Table. 4.5 summarizes the number of background events for both gamma rays and neutrons in the case of the Xenon1T detector. Their energy spectra are plotted together for the 1.1 ton fiducial volume in Fig. 4.19. It has been shown that, by effectively reducing the background with self-shielding and multiple-hit cut, the Xenon1T can achieve a background level that is well below 1 event per year, while being able to reach a sensitivity down to 10^{-46} cm^2.

Background Unit	ER $[10^{-7}$ dru$_{ee}]$	NR $[10^{-9}$ dru$_{nr}]$
QUPID	<8.50	<2.18
PTFE	<0.84	<4.84
Titanium	<2.13	<0.34
Acrylic	<0.02	<0.01
Total BG	<11.5	<7.4
# of BG events	<0.07	<0.10
# of WIMP events ($M_\chi = 100$ GeV/c^2, $\sigma_{\chi-p} = 10^{-46}$ cm^2)	5.6	

Table 4.5: Predicted background rate and the number of events in a 1-ton-year exposure in the WIMP search region ($7 - 45$keVr). 99% S2/S1 ER rejection efficiency, 50% NR acceptance, and 80% software acceptance has been assumed.

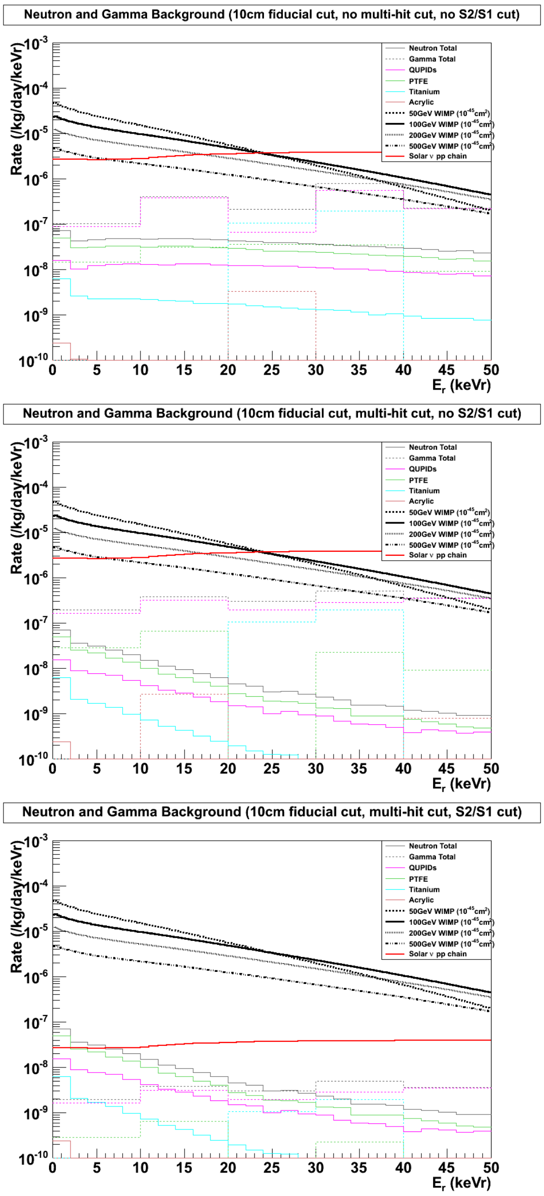

Figure 4.19: Energy spectrum of both the ER (dashed) and NR (solid) backgrounds for Xenon1T for 10 cm fiducial cut with (middle) and without (top) multiple-hit cut. Bottom plot shows the spectrum with both the multiple-hit cut and the S2/S1 cut. Background rates are plotted for different detector materials: QUPID (pink), PTFE (green), titanium (light blue), acrylic (brown), and total (black). Also shown are the WIMP spectrum at $\sigma = 10^{-45}$ cm^2 for various WIMP masses: 50 GeV (dashed), 100 GeV (solid), 200 GeV (dotted), 500 GeV (dash-dotted).

4.7 Sensitivities

4.7.1 Upper Limits of Spin-independent Cross Sections

Using the recoil energy spectrum given in Sec. 2.3.1, the upper limits can be calculated in a similar way as the XENON100 detector in Sec. 3.3.5. Fig. 4.20 shows the spin-independent cross section upper limits for Xenon1T, Argon5T, Xenon10T, and Argon50T. With increased fiducial mass and data-taking time, they are able to achieve improvements of more than 3 orders of magnitude over the current XENON100 results and start to probe further into the parameter space predicted by supersymmetry. Shown in fig. 4.20 as an example is the region (grey area) favored by the constrained minimal supersymmetric standard model (CMSSM), as determined by a Markov Chain Monte Carlo scanning technique with 95% CL in the case of $\mu > 0$ [56]. If no events are observed in the Xenon10T and the Argon50T detector, it will be possible to almost fully exclude the above parameter space.

4.7.2 Measurements of WIMP Mass and WIMP-Nucleon Cross Section

If dark matter events are seen in the future detectors, the WIMP mass and WIMP-nucleon cross section can be found with precision depending on the number of events observed. While the recoil energy spectrum changes proportionally with the WIMP-nucleon cross section, the slope of the energy spectrum varies with the WIMP mass (with lower WIMP masses having steeper slopes). Therefore knowing the observed spectrum will allow us to measure both the cross section and the WIMP mass. Fig. 4.21 and 4.22 shows the $1-$ and $2-\sigma$ error of WIMP mass and WIMP-nucleon cross section by a goodness-of-fit test of the

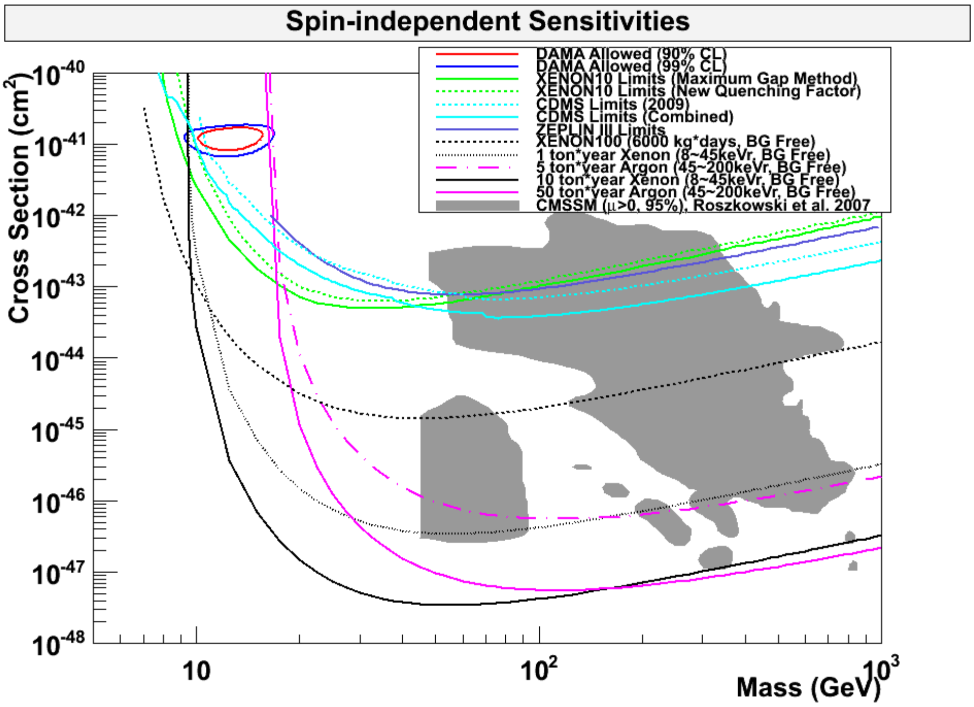

Figure 4.20: Upper limits of spin-independent WIMP-nucleon cross section for WIMP masses between 5 and 1000 GeV. Limits and sensitivities are shown for different experiments: 10 ton Xenon (solid black), 50 ton Argon (solid pink), 1 ton Xenon (dotted black), 5 ton Argon (long dashed pink), XENON10 (green) [12], CDMS (light blue) [3], ZEPLIN III (purple) [55]. Also shown are the DAMA-allowed region at 90% and 99% CL (red and blue) and the parameter space favored by CMSSM (grey) [56].

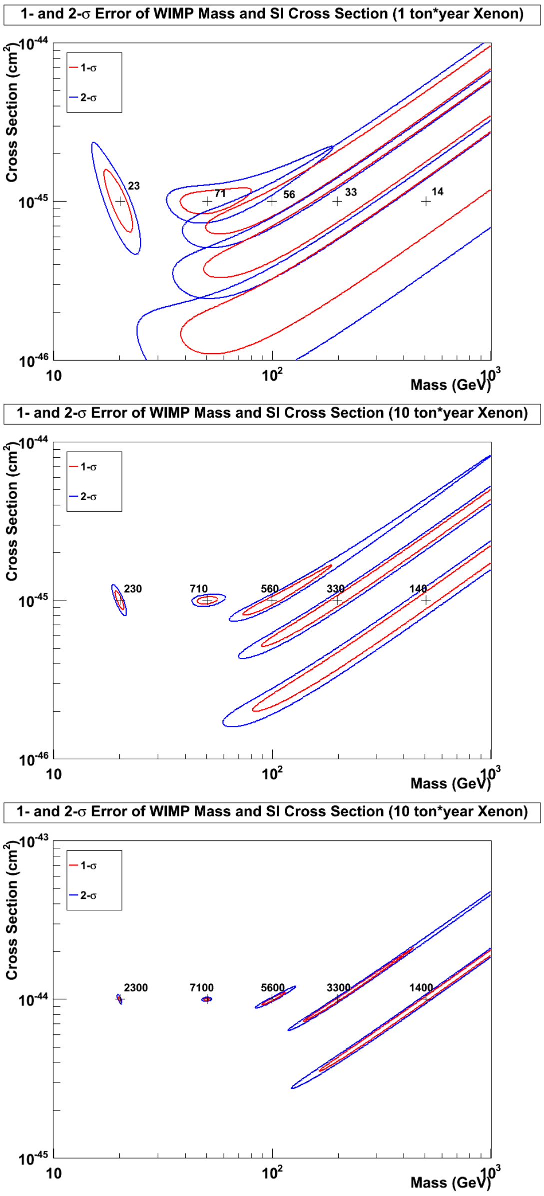

Figure 4.21: $1-$ and $2-\sigma$ error (red and blue) of WIMP mass and WIMP-nucleon cross section by a goodness-of-fit test of the energy spectrum from a LXe detector. Results are shown for WIMP masses of 20, 50, 100, 200, and 500 GeV, labeled with the expected number of events. Top: 1 ton-year exposure with a cross section of 10^{-45} cm^2. Middle: 10 ton-year exposure with a cross section of 10^{-45} cm^2. Bottom: 10 ton-year exposure with a cross section of 10^{-44} cm^2.

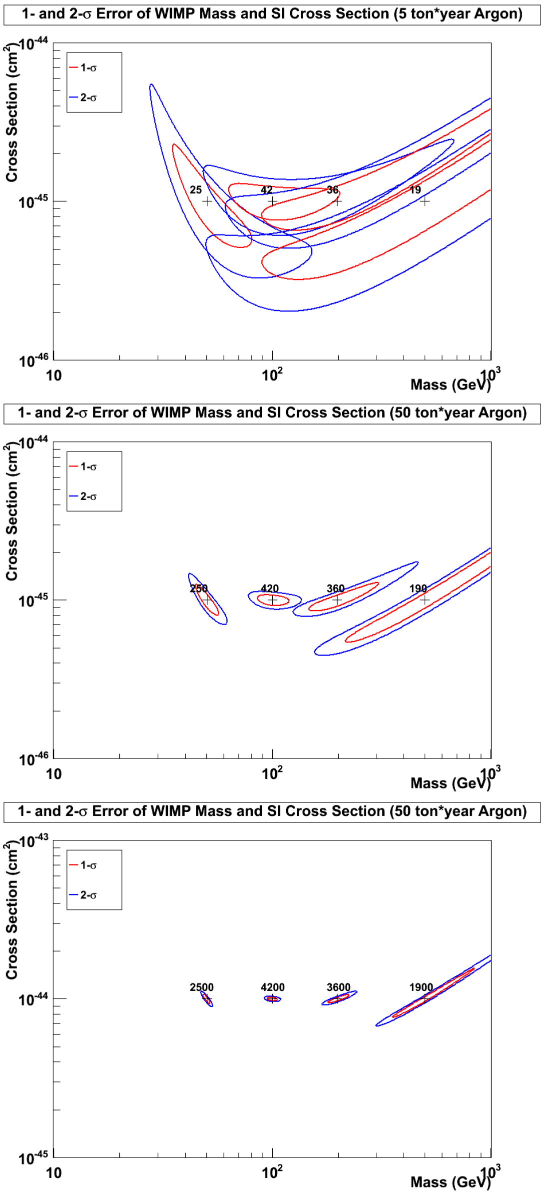

Figure 4.22: 1− and 2−σ error (red and blue) of WIMP mass and WIMP-nucleon cross section by a goodness-of-fit test of the energy spectrum from a LAr detector. Results are shown for WIMP masses of 50, 100, 200, and 500 GeV, labeled with the expected number of events. Top: 5 ton-year exposure with a cross section of 10^{-45} cm^2. Middle: 50 ton-year exposure with a cross section of 10^{-45} cm^2. Bottom: 50 ton-year exposure with a cross section of 10^{-44} cm^2.

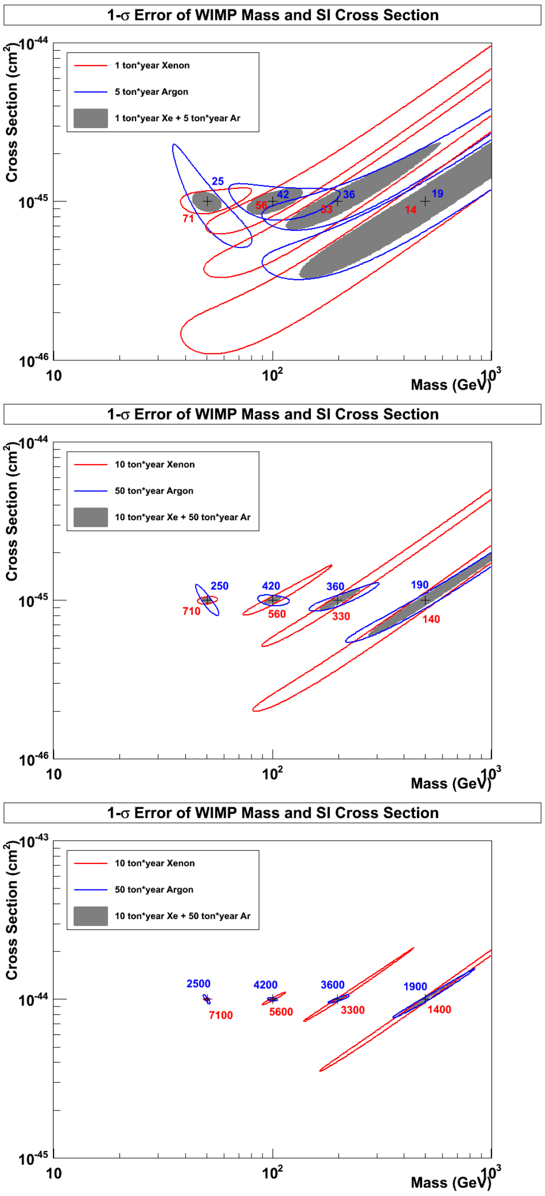

Figure 4.23: $1-\sigma$ error of WIMP mass and WIMP-nucleon cross section by a goodness-of-fit test of the energy spectrum from a LXe (red), a LAr (blue) detector, and with both combined (grey). Results are shown for WIMP masses of 20, 50, 100, 200, and 500 GeV, labeled with the expected number of events. Top: 1 ton-year LXe and 5 ton-year LAr exposure with a cross section of 10^{-45} cm^2. Middle: 10 ton-year LXe and 50 ton-year LAr exposure with a cross section of 10^{-45} cm^2. Bottom: 10 ton-year LXe and 50 ton-year LAr exposure with a cross section of 10^{-44} cm^2.

energy spectrum for xenon and argon detectors separately, with different assumed values of the actual cross section. Furthermore, by combing both the results from a xenon and a argon detector, a better constraint on the parameter values can be obtained, as shown in Fig. 4.23.

4.7.3 Measurements of WIMP Mass and WIMP Characteristic Velocity Using Annual Modulation

In addition to the WIMP mass and the WIMP-nucleon cross section, the WIMP velocity in the dark matter halo can also be measured. The modulation amplitude varies with the WIMP mass (Fig. 4.24 and 4.25) and the WIMP velocity (Fig. 4.25) for both the xenon and argon detectors. If considerable number of events are seen in a one-year exposure, it will be possible to estimate the WIMP velocity based on the observed modulation amplitude.

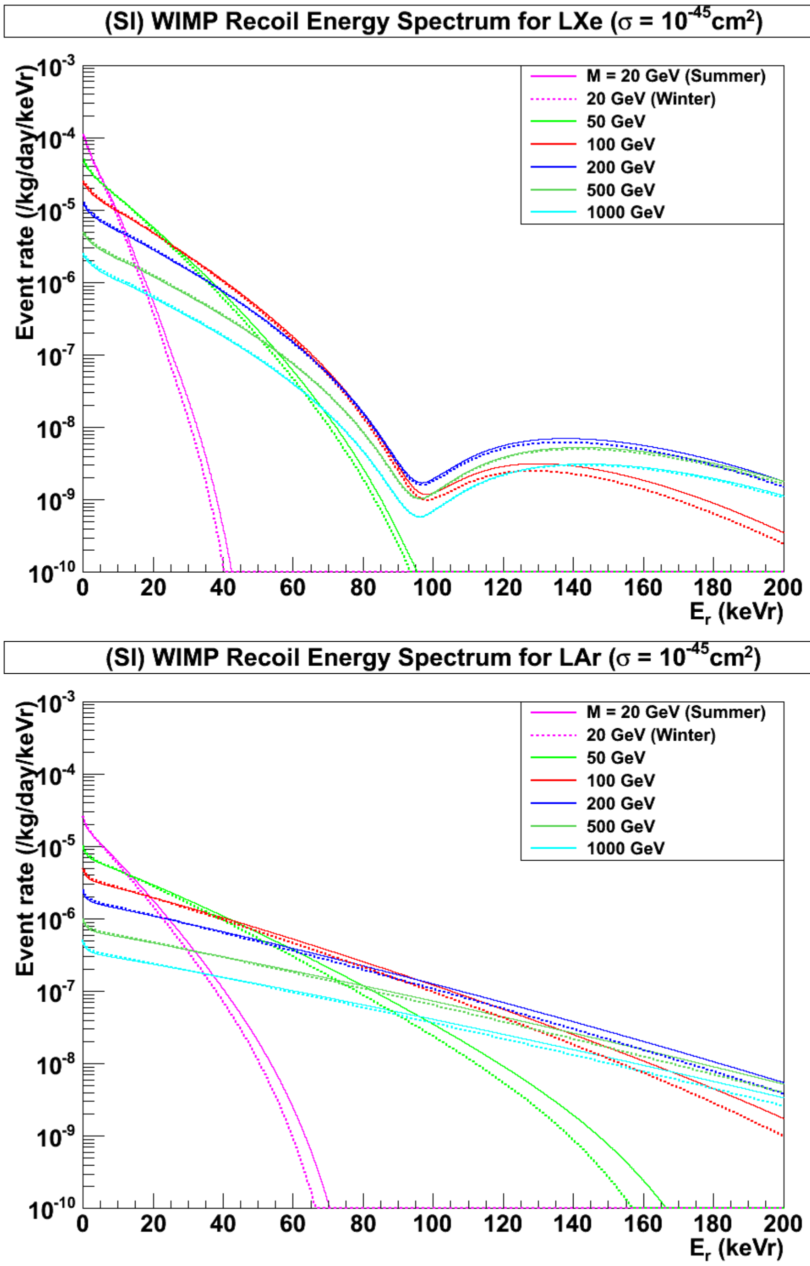

Figure 4.24: Recoil energy spectrum for Xe (top) and Ar (bottom) in summer (solid) and winter (dashed) for WIMP masses of 20, 50, 100, 200, 500, and 1000 GeV.

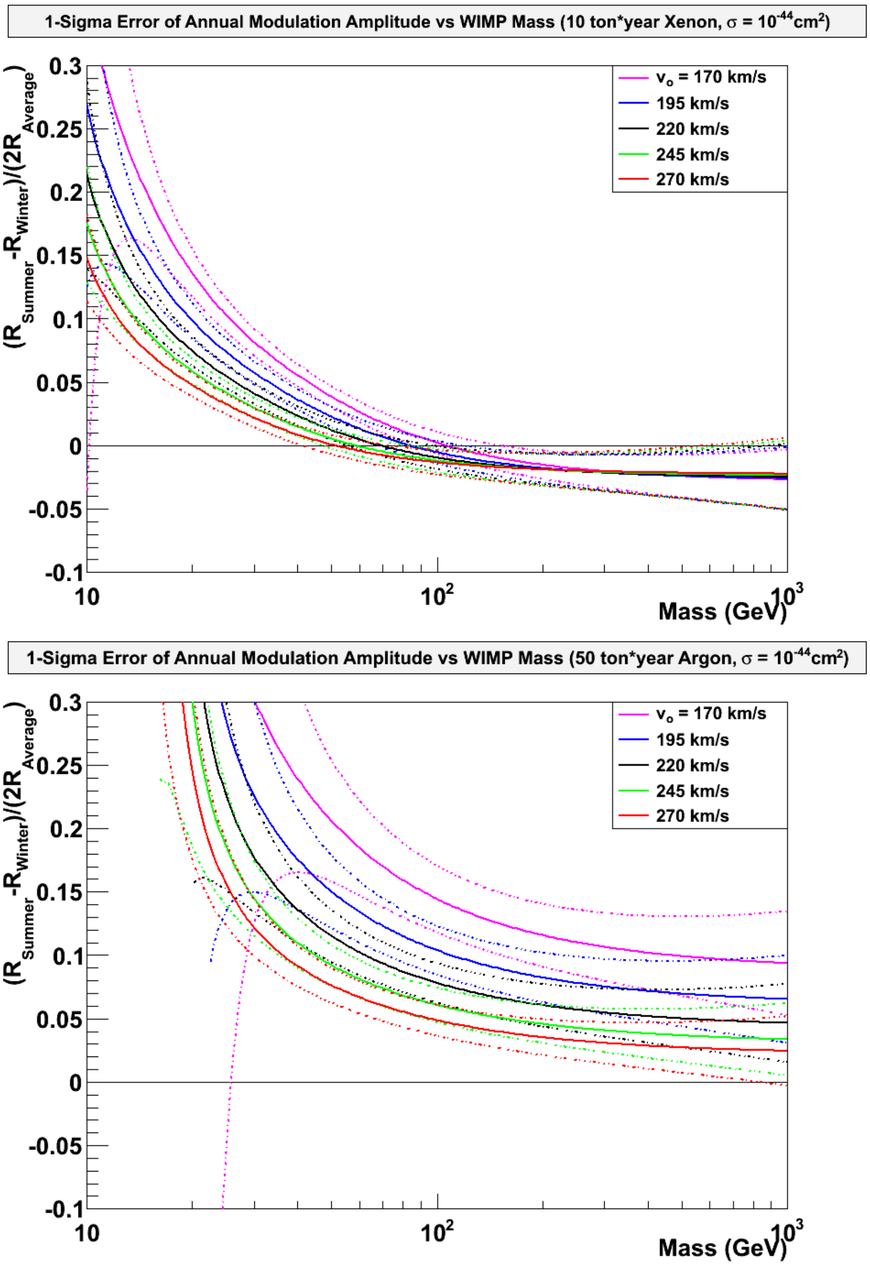

Figure 4.25: Modulation amplitude with $1-\sigma$ error for 10 ton-year LXe (top) and 50 ton-year LAr (bottom) with a cross section of 10^{-45} cm^2. Results are shown for different WIMP characteristic velocities: 170, 195, 220, 245, and 270 km/s.

CHAPTER 5

Conclusion

The 40 kg × 11.17 days results presented here have demonstrated the capability of XENON100 as an ultra-low background detector. With only 11.17 days of exposure, it has achieved competitive limits in both the elastic and the inelastic dark matter explanations. With ongoing data-taking this year and increased exposure, it will be able to either challenge or reinforce the results of other experiments in a serious way. In particular, it will shed light on the current situation of the low mass WIMP and inelastic dark matter, and make stronger statements on these two scenarios.

For the future detectors, the ability to limit the background to less than 1 event is important in obtaining the best sensitivity. With Monte Carlo simulations, it has been shown to be possible to reduce the gamma and neutron background respectively by adopting ultra-low radioactive QUPIDs and background rejection techniques. On the other hand, in the case that WIMPs with parameters predicted by supersymmetry do exist, one will be able to learn a lot from the prominent signals of these detectors.

For my dissertation work, I was involved in the analysis of the Spin-independent cross section limit for the 11.17 days results, and I calculated the inelastic dark matter limit. I performed the studies on future detectors, including internal gamma and neutron background simulations for Xenon1T, Xenon10T, Argon5T, and Argon50T, as well as the prediction of their sensitivities. I also participated in shifts for the XENON100 detector at LNGS, particularly the Kr distillation run in summer 2009.

REFERENCES

[1] *http://map.gsfc.nasa.gov/.*

[2] E. Aprile *et al.* (XENON) (2010), arXiv:1001.2834.

[3] Z. Ahmed *et al.* (CDMS) (2009), arXiv:0912.3592v1.

[4] R. Bernabei et. al., Nucl. Instrum. Meth. **A592**, 297-315 (2008).

[5] C. E. Aalseth *et al.* (CoGeNT) (2010), arXiv:1002.4703.

[6] G. Angloher *et al.*, Astropart. Phys. **31**, 270-276 (2009).

[7] W. de Boer *et al.*, Astron. Astrophys. **444**, 51 (2005).

[8] M. Ackermann *et al.* (Fermi-LAT), JCAP **05**, 025 (2010).

[9] M. Casolino *et al.*, (PAMELA) (2009), arXiv:0904.4692v1.

[10] V. A. Acciari *et al.* (VERITAS), Astrophys. J. **720**, 1174-1180 (2010).

[11] Z. Thomas, D. Tucker-Smith, and N. Weiner, Phys. Rev. **D77**, 115015 (2008).

[12] J. Angle *et al.* (XENON), Phys. Rev. Lett. **100**, 021303 (2008).

[13] CDMS Collaboration, Phys. Rev. **D66**, 122003 (2002).

[14] Oleg Kamaev (CDMS) (2009), arXiv:0910.3005.

[15] R. Bernabei *et al.*, Eur. Phys. J. **C56**, 333-355 (2008).

[16] C. Savage, G. B. Gelmini, P. Gondolo, and K. Freese, JCAP **04**, 010 (2009).

[17] J. D. Lewin and P. F. Smith, Astropart. Phys. **6**, 87 (1996).

[18] *http://environmentalchemistry.com/.*

[19] J. Engel, Phys. Lett. **B264**, 114 (1991).

[20] M. T. Ressell and D. J. Dean, Phys. Rev. **C56**, 535 (1997).

[21] E. Aprile and T. Doke, Rev. Modern Phys. **82**, 2010.

[22] N. Smith *et al.*, PPARC astroparticle physics project, galactic dark matter search volume A (2004).

[23] E. Aprile *et al.* (XENON100) (2010), arXiv:1005.0380 (Accepted by Phys. Rev. Lett.).

[24] XENON100 Collaboration, private communication.

[25] E. Aprile *et al.*, Phys. Rev. Lett. **97**, 081302 (2006).

[26] J. Lindhard *et al.*, Mat. Fys. Medd. Dan. Vid. Selsk. **33** (1963).

[27] F. Arneodo *et al.*, Nucl. Instrum. Meth. **A449**, 147 (2000).

[28] R. Bernabei *et al.*, EPJdirect C **11**, 1 (2001).

[29] D. Akimov *et al.*, Phys. Lett. **B524**, 245 (2002).

[30] E. Aprile *et al.*, Phys. Rev. **D72**, 072006 (2005).

[31] V. Chepel *et al.*, Astropart. Phys. **26**, 58-63 (2006).

[32] E. Aprile *et al.*, Phys. Rev. **C79**, 045807 (2009).

[33] A. Manzur *et al.*, Phys. Rev. **C81**, 025808 (2010).

[34] R. Trotta *et al.*, J. High Energy Phys. **12**, 024 (2008).

[35] D. Smith and N. Weiner, Phys. Rev. **D64**, 043502 (2001).

[36] N. Arkani-Hamed, D. P. Finkbeiner, T. R. Slatyer, N. Weiner, Phys. Rev. **D79**, 015014 (2009) .

[37] O. Adriani *et al.*, Nature **458**, 607-609 (2009).

[38] J. Chang *et al.* (ATIC) (2005), prepared for 29th International Cosmic Ray Conferences (ICRC 2005).

[39] S. Chang, G. D. Kribs, D. Tucker-Smith, and N. Weiner, Phys. Rev. **D79**, 043513 (2009).

[40] W. Dehnen and J. Binney, Mon. Not. Roy. Astron. Soc. **298**, 387 (1998).

[41] K. Schmidt-Hoberg and M. W. Winkler, JCAP **09**, 010 (2009).

[42] R. Bernabei *et al.*, Eur. Phys. J. **C53**, 205 (2008).

[43] N. Bozorgnia, G. B. Gelmini, and P. Gondolo (2010), arXiv:1006.3110v1.

[44] M. C. Smith *et al.*, Mon. Not. Roy. Astron. Soc. **379**, 755-772 (2007).

[45] F. Donato, N. Fornengo, and S. Scopel, Astropart. Phys. **9**, 247-260 (1998).

[46] J. Angle *et al.* (XENON), Phys. Rev. **D80**, 115005 (2009).

[47] K. Arisaka *et al.*, Astropart. Phys. **31**, 63 (2009).

[48] UCLA dark matter group, private communication.

[49] G. Alimonti *et al.* (Borexino) (2008), arXiv:0806.2400v1.

[50] S. Agostinelli *et al.*, Nucl. Instrum. Meth. **A506**, 250 (2003).

[51] *http://geant4.cern.ch/.*

[52] *http://root.cern.ch/.*

[53] C. Bungau *et al.*, Astropart. Phys. **23**, 97-115 (2005).

[54] P. Benetti *et al.*, Astropart. Phys. **28**, 495-507 (2008).

[55] V. N. Lebedenko *et al.*, Phys. Rev. **D80**, 052010 (2009).

[56] L. Roszkowski *et al.*, JHEP **0707**, 075 (2007).